1-1-2017

Unraveling Recrystallization Mechanisms Governing Texture Development from Rare Earth Element Additions to Magnesium

Aidin Imandoust

Follow this and additional works at: https://scholarsjunction.msstate.edu/td

Unraveling recrystallization mechanisms governing texture development from rare earth

element additions to magnesium

By

Aidin Imandoust

A Dissertation
Submitted to the Faculty of
Mississippi State University
in Partial Fulfillment of the Requirements
for the Degree of Doctor of Philosophy
in Mechanical Engineering
in the Department of Mechanical Engineering

Mississippi State, Mississippi

August 2017

Unraveling recrystallization mechanisms governing texture development from rare earth

element additions to magnesium

By

Aidin Imandoust

Approved:

_____
Haitham El Kadiri
(Major Professor)

_____
Nima Shamsaei
(Committee Member)

_____
Lei Chen
(Committee Member)

_____
Andrew L. Oppedal
(Committee Member)

_____
Wilburn Whittington
(Committee Member)

_____
Yucheng Liu
(Graduate Coordinator)

_____
Jason M. Keith
Dean
Bagley College of Engineering

Name: Aidin Imandoust

Date of Degree: August 11, 2017

Institution: Mississippi State University

Major Field: Mechanical Engineering

Major Professor: Dr. Haitham El Kadiri

Title of Study: Unraveling recrystallization mechanisms governing texture development
from rare earth element additions to magnesium

Pages in Study: 176

Candidate for Degree of Doctor of Philosophy

The origin of texture components associated with rare-earth (RE) element additions in wrought magnesium (Mg) alloys is a long-standing problem in magnesium technology. The objective of this research is to identify the mechanisms accountable for rare-earth texture during dynamic recrystallization (DRX). Towards this end, we designed binary Mg-Cerium and Mg-Gadolinium alloys along with complex alloy compositions containing zinc, yttrium and Mischmetal. Binary alloys along with pure Mg were designed to individually investigate their effects on texture evolutions, while complex compositions are designed to develop randomized texture, and be used in automotive and aerospace applications. We selected indirect extrusion to thermo-mechanically process our materials. Different extrusion ratios and speeds were designed to produce partially and fully recrystallized microstructures, allowing us to analyze DRX from its early stages to completion. X-ray diffraction, electron backscattered diffraction (EBSD) and transmission electron microscopy (TEM) were used to conduct microstructure and texture analyses.

Our analyses revealed that rare-earth elements in zinc-containing magnesium alloys promote discontinuous dynamic recrystallization at the grain boundaries. During nucleation, the effect of rare earth elements on orientation selection was explained by the concomitant actions of multiple Taylor axes in the same grain. Isotropic grain growth was observed due to rare earth elements segregating to grain boundaries, which lead to texture randomization.

The nucleation in binary Mg-RE alloys took place by continuous formation of necklace structures. Stochastic relaxation of basal and non-basal dislocations into low-angle grain boundaries produced chains of embryos with nearly random orientations. Schmid factor analysis showed a lower net activation of dislocations in RE textured grains compared to ones on the other side of the stereographic triangle. Lower dislocation densities within RE grains favored their growth by setting the boundary migration direction toward grains with higher dislocation density, thereby decreasing the system energy.

We investigated the influence of RE elements on extension twinning induced hardening. RE addition enhanced tensile twinning induced hardening significantly. EBSD analysis illustrated that tensile twins cross low angle grain boundaries in Mg-RE alloys, which produced large twins and facilitated transmutation of basal to prismatic dislocations. Higher activity of pyramidal II dislocations in Mg-RE alloys resulted in higher twinning induced hardening.

DEDICATION

This work is dedicated to my loving mother, Fattaneh Malekzadeh, and my father's gentle soul, Mahmood Imandoust, who have always loved their little son unconditionally and whose critical support and care taught me how to be a better and successful person.

ACKNOWLEDGEMENTS

TABLE OF CONTENTS

LIST OF TABLES

LIST OF FIGURES

CHAPTER I

INTRODUCTION

1.1   Introduction

Over the past decades, magnesium (Mg) and its alloys has garnered attention due to their high specific strength [1, 2]. However, poor room temperature formability of Mg has been the paramount setback, in terms of cost-effectiveness, for the development of its industrial applications [3]. Furthermore, Mg alloys develop sharp texture during deformation, which exacerbates the plastic flow anisotropy and yield asymmetry of Mg products [4]. For instance, rolled Mg sheets develop basal texture (i.e. $[0001]||ND$), and extruded Mg alloys has strong rod texture (i.e. $\langle 10\bar{1}0\rangle||ED$) [5]. Hence, texture development in Mg alloys is one of the key components for development of Mg products.

The perspective of the contemporary research is to design and develop new Mg alloys with improved ductility and randomized texture [6]. The most successful approach towards this end has been the addition of rare earth (RE) elements to magnesium [7, 8]. Rare earth addition not only ameliorates room temperature ductility of magnesium alloys, but also modifies their recrystallization texture [9]. Ductility improvement in Mg-RE alloys is attributed to the higher activity of non-basal dislocations (e.g. $\langle c + a\rangle$ dislocations) [10]. As a matter of fact, RE additions reduce the gap between the critical resolved shear stress (CRSS) values of basal and non-basal slip modes, which homogenizes their relative activity[1]. It has been reported that RE elements reduce the

stacking fault on basal and/or non-basal planes, which reduces the CRSS value for activation of $\langle c + a \rangle$ dislocations [11].

Texture modification is the other key factor in alloying Mg with RE elements. While traditional Mg alloys have the tendency to sharpen their texture upon dynamic and static recrystallization [12], RE containing Mg alloys develop random/modified recrystallization texture [13]. However, the mechanism through which the texture randomization takes place has been a long standing problem in materials science research. After deciphering this texture weakening effect in a RE containing Mg alloy, dubbed WE54, Ball and Prangnell attributed the texture weakening effect to particle-stimulated nucleation (PSN) during dynamic recrystallization (DRX) [14]. Nevertheless, Al-Samman *et al.* showed that PSN was associated with non-RE particles [13]. Additionally, Robson *et al.* demonstrated that grain boundary nucleated grains have growth preference over PSN grains [15]. Hence, one can rule out the necessity of PSN as an essential mechanism for texture weakening. Stanford and Barnett [8] reported the formation of grains with "RE texture" within shear bands in extruded binary Mg-RE alloys. They held the shear banding phenomenon accountable for texture modifications. On the other hand, solid solution Mg-RE alloys with no shear banding events exhibited similar effects [16]. Hadorn *et al.* observed the transition from the domination of basal dislocations to prevalence of prismatic dislocations, which was theorized to alter recrystallization characteristics [17]. Stanford hypothesized this phenomenon to be tied with the interaction between solute and Mg atoms [9]. Segregation of RE elements to grain boundaries is another key influence that should be taken into account in order to thoroughly address the RE effects [17]. In case of ternary or complex Mg-RE alloys, co-

2

segregation of zinc (Zn) and RE elements was shown to remarkably influence the growth preference of DRX nuclei [18, 19].

Although numerous researchers have addressed different aspects of "RE texture" phenomenon, the existing literature lacks a complete consensus on the details of dynamic and static recrystallization, and their correlation with texture evolution in Mg-RE alloys. To this end, we designed complex Mg-RE alloys to investigate the minute detail of recrystallization and texture evolution in real world alloys. Moreover, we designed binary Mg-RE alloys to address their individual effects of RE elements. We selected indirect extrusion as our processing method, by altering the parameters of which recrystallization kinetics were controlled. Using electron back scattered electron diffraction (EBSD) and transmission electron microscopy (TEM) techniques, we tracked the microstructural and textural evolutions from the beginning to completion. In this study, we unraveled the contribution of active recrystallization mechanisms, namely continuous dynamic recrystallization (CDRX) and discontinuous dynamic recrystallization (DDRX). Furthermore, we analyzed the textural transitions and proposed a mechanism for development of RE texture from $\langle 10\bar{1}0 \rangle$ fiber texture of parent grains in binary and complex alloys. The origin of growth preference for "RE texture" in terms of grain boundary and process geometry effects was also addressed during dynamic and static recrystallization.

1.2 References

[1] S.R. Agnew, Ö. Duygulu, Plastic anisotropy and the role of non-basal slip in magnesium alloy AZ31B, Int. J. Plast. 21 (2005) 1161-1193.

[2] S.R. Agnew, J.A. Horton, T.M. Lillo, D.W. Brown, Enhanced ductility in strongly textured magnesium produced by equal channel angular processing, Scripta Mater. 50 (2004) 377-381.

[3] B. Mordike, T. Ebert, Magnesium: properties—applications—potential, Mater. Sci. Eng. A 302 (2001) 37-45.

[4] T. Al-Samman, X. Li, Sheet texture modification in magnesium-based alloys by selective rare earth alloying, Mater. Sci. Eng. A 528 (2011) 3809-3822.

[5] S.R. Agnew, P. Mehrotra, T.M. Lillo, G.M. Stoica, P.K. Liaw, Crystallographic texture evolution of three wrought magnesium alloys during equal channel angular extrusion, Mater. Sci. Eng. A 408 (2005) 72-78.

[6] C. Zhao, R. Song, L. Zhang, F. Yang, T. Kang, Effect of annealing temperature on the microstructure and tensile properties of Fe–10Mn–10Al–0.7 C low-density steel, Mater. Des. 91 (2016) 348-360.

[7] N. Stanford, D. Atwell, A. Beer, C. Davies, M.R. Barnett, Effect of microalloying with rare-earth elements on the texture of extruded magnesium-based alloys, Scripta Mater. 59 (2008) 772-775.

[8] N. Stanford, M.R. Barnett, The origin of "rare earth" texture development in extruded Mg-based alloys and its effect on tensile ductility, Mater. Sci. Eng. A 496 (2008) 399-408.

[9] N. Stanford, Micro-alloying Mg with Y, Ce, Gd and La for texture modification—A comparative study, Mater. Sci. Eng. A 527 (2010) 2669-2677.

[10] S. Sandlöbes, M. Friák, J. Neugebauer, D. Raabe, Basal and non-basal dislocation slip in Mg–Y, Mater. Sci. Eng. A 576 (2013) 61-68.

[11] S. Sandlöbes, S. Zaefferer, I. Schestakow, S. Yi, R. Gonzalez-Martinez, On the role of non-basal deformation mechanisms for the ductility of Mg and Mg–Y alloys, Acta Mater. 59 (2011) 429-439.

[12] S. Agnew, M. Yoo, C. Tome, Application of texture simulation to understanding mechanical behavior of Mg and solid solution alloys containing Li or Y, Acta Mater. 49 (2001) 4277-4289.

[13] T. Al-Samman, X. Li, Sheet texture modification in magnesium-based alloys by selective rare earth alloying, Mater. Sci. Eng. A 528 (2011) 3809-3822.

[14] E. Ball, P. Prangnell, Tensile-compressive yield asymmetries in high strength wrought magnesium alloys, Scripta Metallurgica et Materialia 31 (1994) 111-116.

[15] J.D. Robson, D.T. Henry, B. Davis, Particle effects on recrystallization in magnesium–manganese alloys: Particle-stimulated nucleation, Acta Mater. 57 (2009) 2739-2747.

[16] J.P. Hadorn, R.P. Mulay, K. Hantzsche, S. Yi, J. Bohlen, D. Letzig, S.R. Agnew, Texture Weakening Effects in Ce-Containing Mg Alloys, Metall. Mater. Trans. A 44 (2012) 1566-1576.

[17] J.P. Hadorn, K. Hantzsche, S. Yi, J. Bohlen, D. Letzig, J.A. Wollmershauser, S.R. Agnew, Role of Solute in the Texture Modification During Hot Deformation of Mg-Rare Earth Alloys, Metall. Mater. Trans. A 43 (2011) 1347-1362.

[18] Z.R. Zeng, M.Z. Bian, S.W. Xu, C.H.J. Davies, N. Birbilis, J.F. Nie, Texture evolution during cold rolling of dilute Mg alloys, Scripta Mater. 108 (2015) 6-10.

[19] Z.R. Zeng, Y.M. Zhu, S.W. Xu, M.Z. Bian, C.H.J. Davies, N. Birbilis, J.F. Nie, Texture evolution during static recrystallization of cold-rolled magnesium alloys, Acta Mater. 105 (2016) 479-494.

CHAPTER II

A REVIEW ON THE EFFECT OF RARE EARTH ELEMENTS ON TEXTURE

EVOLUTION DURING PROCESSING OF MAGNESIUM ALLOYS;

JOURNAL OF MATERIALS SCIENCE (2017) 52:1–29.

2.1   Introduction

The ever-increasing demand for magnesium (Mg) and its alloys due to their low

density and good castability has produced an active research field aiming to develop cast

and wrought Mg alloys with superior performance and processability [1-6]. For the last

two decades, enormous efforts have been dedicated to improving mechanical properties

such as creep resistance, ductility and specific strength by employing intelligent thermo-

mechanical processing and alloying strategies [7]. Poor ductility of traditional wrought

Mg alloys at room temperatures has restricted their application because of cost-

prohibitive processing requiring forming operations at high temperatures (573-

723 K(300-450 ºC)), as well as an inability for hallow structure to absorb energy under

crash scenarios [8-10]. Designing new Mg alloys with improved properties would greatly

extend the potential usage of Mg alloys, resulting in a considerable weight reduction and

consequently lower carbon footprint for entire industries [11-19].

The unfavorable mechanical response depicted by most conventional wrought Mg

alloys has been attributed to their tendency to develop very sharp textures, which respond

to mechanical load, just like single crystals, with excessive strain-path anisotropy and

asymmetry [20-23]. In fact, the low symmetry associated with their hexagonal close-packed structure (HCP) does not allow easy slip to occur along the geometrically versatile pyramidal directions. Instead, easy slip occurs along directions contained within the basal plane which are unable to provide deformation along the $\langle c \rangle$-axis. Activation of pyramidal slip is actually so hard that mechanical twining takes place much easier on pyramidal planes and directions at medium temperatures and low strain rates. Twinning has been understood as the prime mechanism responsible for the observed anisotropic behavior [24-30].

Although the significant differences in the critical resolved shear stresses (CRSS) for basal, prismatic and pyramidal slip systems are reduced as the temperature increases, rolled products and extruded billets still endure the development of a very sharp basal texture [31,24]. Moreover, during post annealing treatments, these strong deformation textures persist and if anything, intensify in the presence of grain growth [32-34]. In this respect, a great deal of research has been performed based on the hypothesis that altering the predominant deformation and dynamic recrystallization (DRX) mechanisms would produce Mg products with weaker textures, and hence, with less anisotropy and asymmetry. Small additions of rare-earth (RE) elements have been proved in fact beneficial in supporting this hypothesis, as weaker intensities developed and correlated with a mitigation in the anisotropic behavior and gain of ductility [35-39]. A particular feature associated with texture weakening was some special texture components, dubbed "RE-textures", which proved in general to facilitate deformation by basal slip in bending conditions, and thus contributed to the enhancement of ambient temperature formability and the reduction of mechanical anisotropy. Common examples of RE-textures are the

7

$\langle 11\overline{2}1\rangle||ED$ formed during extrusion [40], and the atypical TD spread texture developed during rolling [41-43].

Although room temperature (RT) ductility and tensile strength of Mg alloys have been significantly improved by RE additions (Yttrium included), there is still much room to reduce the yield anisotropy when forming Mg products at RT is considered [20,44]. Moreover, the mechanisms through which the RE texture component develops during thermo-mechanical processing have been a rather challenging puzzle. Among the potential mechanisms proposed in the literature, one can find particle stimulated nucleation (PSN), enhancement of shear banding, increased $\langle c + a \rangle$ slip activity, oriented growth of recrystallized grain nuclei, and recently, grain boundary (GB) energy and mobility, [45-48,35,49-53]. However, it seems that each time a hypothesis for the underlying mechanism is suggested, it is followed by some works which show formation of the same RE texture in conditions where the hypothesized mechanism is not operational.

For instance, despite the predictions from Ball and Prangnell [54], the PSN mechanism cannot be considered as a major contributor to RE texture formation due to its nature of generating random rather than unique types of orientations, and the negligible volume fraction of these orientations (~1% - 5% of the overall texture), unless their growth is favored in some cases [45]. Likewise, although no doubt could be cast on the ability of RE textures to nucleate and thrive in shear [51], many RE texture cases were reported in the literature which do not involve any shear band formation [35,55,56].

With several plausible theories in the literature on the origin of RE-texture, there is however an apparent consensus that RE elements retard dynamic recovery

8

mechanisms by obstructing dislocation motion and hampering cross slip through a reduction of the stacking fault energy. An action on GB energy has been also reported in recent endeavors [35{Robson, 2011 #39]}. These changes would give the chance for a broader orientation spectrum to nucleate and survive than the one comprising a limited set of misorientations and other special boundaries [57,58].

While RE textures can form in dilute Mg-RE solid solutions which entail a limited degree of precipitation, solute drag was suggested to retard recrystallization kinetics as an alternative mechanism to the Zener pinning. Solute drag operates as RE atoms segregate to GBs, which was observed to tally concentrations almost 20 times higher than those measured in the bulk [59]. This high level of segregation is believed to cause a difference in the boundary mobility of basal and non-basal DRX nuclei, in a fashion which leads to preferential growth of RE orientations, and as such their predominance in the final texture [51].

In line with these endeavors, the present work attempts to provide a comprehensive standpoint on the reported recrystallization mechanisms for both traditional and RE element-containing Mg alloys. The goal is to identify gaps forestalling a formal understanding of the RE effect. Filling these gaps could help the scientific community in their bid to design novel Mg alloys and expand their applications to all critical safety components in automotive.

2.1.1   Deformation and texture evolution in Mg alloys

Deformation slip in Mg, which has a c/a ratio of 1.624, (near the ideal c/a ratio of 1.633), takes place very easily on basal planes and $\langle 11\bar{2}0 \rangle$ ($\langle a \rangle$) directions (i.e. close packed direction and plane). Basal $\langle a \rangle$ slip is being understood as responsible for the

9

systemic basal texture development during rolling [60]. However, this type of texture has rarely been observed and the basal poles in rolled Mg sheets are tilted by ±10-20º about the transverse direction toward the rolling direction. This is because of activities related to other deformation modes [60]. Actually, the basal slip mode provides only two independent slip systems, which fail to satisfy the Taylor criterion requiring five independent slip systems for homogeneous plastic deformation [61]. In this context, prismatic slip along the $\langle 11\bar{2}0 \rangle$ ($\langle a \rangle$) direction on the $\{10\bar{1}0\}$ planes would offer two more independent slip systems, but still comes short of the Taylor criterion requirement. Although the activation of pyramidal $\langle a \rangle$ slip would alone provide four more slip systems, [32], it cannot accommodate $\langle c \rangle$-axis deformation. At elevated temperatures ($>$ 573 K (300℃)) slip on the $\{11\bar{2}2\}$ second order pyramidal planes reportedly takes place, especially under $\langle c \rangle$-compression or inside $\{10\bar{1}2\}$ extension twins growing under a compressive macroscopic loading [32,53,62-65]. This slip, whose activation is highly dependent on temperature level, completes the requirements satisfying the Taylor criterion. 2nd order pyramidal slip also exhibits a great level of hardening, and hence, further restricts its occurrence at high temperatures [66]. Deformation along the c-axis can also be accommodated by tension/extension ($\{01\bar{1}2\}\langle 0\bar{1}11 \rangle$) and compression/contraction ($\{01\bar{1}1\}\langle 0\bar{1}12 \rangle$ or $\{01\bar{1}3\}\langle 0\bar{3}32 \rangle$) twins [8,9,67]. Mechanical twinning can normally be considered as an athermal deformation mechanism in hexagonal close packed (HCP) materials, and due to its polar nature, a twin mode can only be triggered either under tension or compression [68].

The activity of the aforementioned deformation mechanisms is governed by their CRSS values, which are generally accepted to scale as CRSS basal <CRSS extension-twinning

<CRSS $_{prismatic}$ <CRSS $_{pyramidal <c+a>}$ [24]. The approximate CRSS ratios with respect to

that of basal slip are approximately 1:38:50:100 in traditional Mg alloys, and the

temperature at which they become active follows the same order [69]. It should be noted

that the alloying elements can introduce solid solution softening or hardening effects for

both slip and twinning deformation modes, thereby changing their relative CRSS ratios

[70,68,71].

In most cases of plastic deformation of magnesium, the imposed strain is

primarily accommodated by basal slip and tensile twinning at low temperatures, while

increasing the deformation temperature favors both pyramidal and prismatic slip modes

[69]. Enhanced activity of prismatic slip beyond 498 K (225 ºC) can significantly

improve ductility. Furthermore, first and second order pyramidal slip become dominant

over {$10\bar{1}2$} twinning above 623 K (350 ºC) and 673 K (400 ºC), respectively [69].

Using polycrystal plasticity modeling, Agnew *et al*. [60] showed that higher activity of

⟨$c + a$⟩ dislocations would form "split-basal poles" tilted toward the rolling direction in

the course of plane strain compression. In hot rolled Mg sheets, this split is often

associated with the rolling direction (RD)-split in basal textures, which develops mainly

because of profuse activity of basal slip compared to other slip modes even at high

temperatures (> 673 K (400 ºC)) [72-74]. Similarly, it has been suggested that the

⟨$10\bar{1}0$⟩ fiber texture that develops during extrusion is another way that basal and

prismatic slip manifests themselves under this type of loading. Basal slip tends to rotate

the basal planes around the ⟨$10\bar{1}0$⟩ Taylor axis to the point they are parallel to the

extrusion direction with a broad orientation fiber to assume the entire ⟨$10\bar{1}0$⟩ − ⟨$11\bar{2}0$⟩

arc. In addition, the activity of prismatic slip may rotate the crystals toward $\langle 10\bar{1}0 \rangle$ [71,75-80].

2.1.2 Dynamic recrystallization of Mg alloys

Depending on temperature, strain rate, and applied strain, four different mechanisms of DRX were observed to operate in Mg [81,82]. These types include continuous DRX (CDRX), discontinuous DRX (DDRX), twin DRX (TDRX) and low temperature DRX (LTDRX) [83]. DDRX corresponds basically to localized rearrangement of dislocations at GB regions, and typically occurs via the bulging mechanism. On the other hand, CDRX could be considered as an extended recovery phenomenon, as rotation and migration of low angle GBs (leading to high angle GBs) take place homogeneously throughout the microstructure. Repetitive cycling of either CDRX or DDRX can potentially develop necklace type structure [84]. Nomenclature of TDRX and LTDRX is based upon their nucleation mechanism and temperature, respectively. These mechanisms were mapped by Sitdikov *et al*. [83] in a temperature vs. true strain diagram depicted in Figure 2.1.

At low temperatures (< 523 K (250 ºC)) and Zener-Holloman parameters above $\sim 7 \times 10^{12} s^{-1}$ [85], extensive deformation twinning on multiple planes causes extensive dislocation pile-ups, which increases the dislocation density in initial grains [82,83].

Deformation twins propagate under further strain, and basal/prismatic slip assisted twin fragmentation takes place [86]. It has been reported that recrystallization inside compression twins is continuous in nature and followed by extensive recovery, and recrystallized grains inherit the orientation of their twin host [87].

12
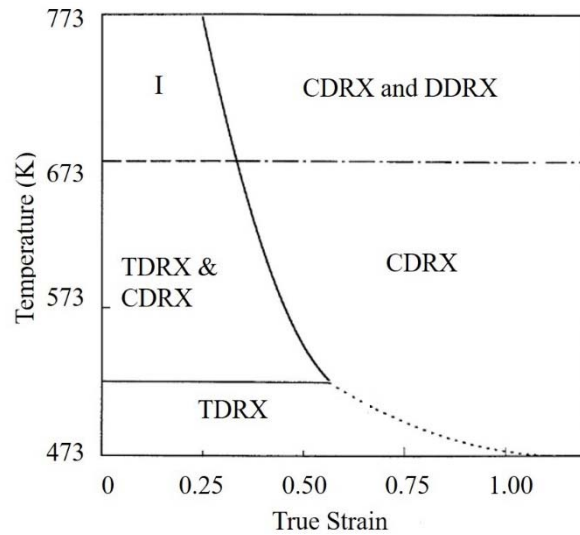
Figure 2.1   Active DRX mechanisms in Mg as a function of temperature ranging from 473 to 773 K (200-500 ºC) and strain.

Twin transformation into recrystallized grains takes place at region I. Reproduced from [83] with permission from the Japan Institute of Metals and Materials.

There has also been observations which proposed that extensive recovery within twins occurs dynamically alongside prismatic slip, which rotates the CDRX grains inside the twin about their $\langle c \rangle$-axis, resulting in subsequent texture randomization [88]. Basically, TDRX is associated with localized slip inside soft twin orientations, which promote fragmentation and localized dynamic recovery, thereby giving rise to strain-free grains. Furthermore, twin DRX mechanisms can vary in dynamic and static recrystallization conditions due to a higher activity of slip dislocations over the course of deformation. Depending on the chemistry of the Mg alloys, TDRX may take place through different mechanisms where CDRX or DDRX commence within twins [86]. TDRX can also take place in regions subjected to intersections of deformation twins at elevated temperatures. The optical micrograph of Figure 2.2 shows the formation of

quadrilateral grains as a result of twinning intersection in AZ81 Mg alloy deformed at

523 K (250 ºC) up to a true strain of 0.45 [89].
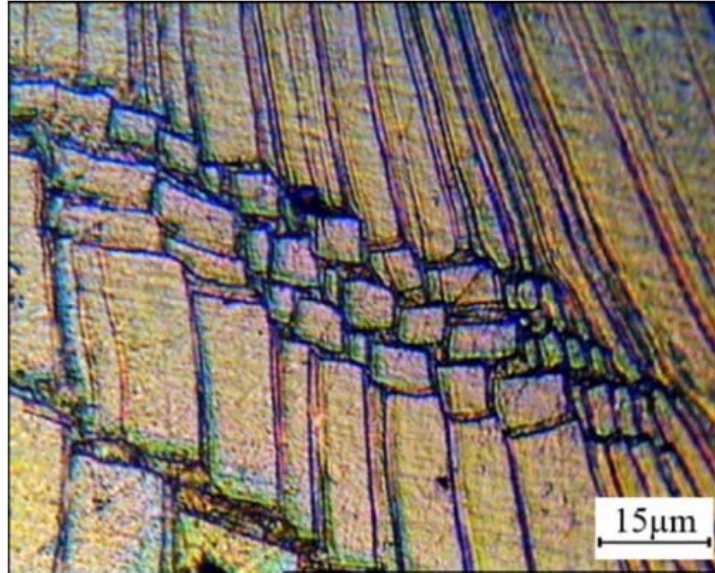
Figure 2.2   Twinning intersection in AZ81 Mg alloy after uniaxial compression.

Testing was performed at 523 K (250 ºC) to the true strain of 0.45 at the initial strain rate
of 0.3 s^{-1}. Reproduced from [89] with permission from Elsevier.

The growth of intersected twin lamellas may be accommodated either by

increasing strain levels when temperature is very low (i.e. $\varepsilon = 1$) or by heat at elevated

temperatures [89,83]. In other words, high density of lattice dislocations and internal

elastic strain at low temperatures (i.e. ambient temperature) ensure the growth of DRX

nuclei. The small size of TDRX grains reduces the propensity for twinning at large

strains [83]. As a result, high density of GB dislocations and stored strain energy lead to

LTDRX.

On the other hand, "twin and sub-grain mechanism of DRX" refers to the

concurrent activation of TDRX and CDRX mechanisms. At temperatures above 523 K

(250 ºC), twin nucleation and twin-twin intersection occur before the steady state of strain could be reached (ε_{ss}) [83]. Increasing strain leads to the formation of chains of recrystallized grains running across twin lamellas. A slight grain growth was also detected at these levels, and was ascribed to the larger nucleus size generated through the CDRX mechanism [83].

At higher temperatures, typically greater than 350°C, deformation twinning is practically eliminated by the drastic increase in the activity of dislocations with Burgers vectors out of the basal plane. Any pre-existing twin may be able to grow through migration of incoherent segments of twin boundaries. However, it would rapidly collapse in favor to low-angle GBs running across the twin. The subdivision process leads to rectangular grains extending over spaces created across the twin thickness (Region I in Figure 2.1) [83]. Depending on temperature, this recrystallization process may saturate at strains no less than 0.7 [83]. In the high temperature regime, the inherent higher strains cause repetitive formation and development of sub-grains at parent GBs [90,84,83]. Furthermore, when the activation energy for steady-state creep is almost equal to that required for self-diffusion (135 kJ mol^{-1} [91]), deformation becomes controlled by climb of basal dislocations [91]. In this regime DDRX was observed to take place at GBs and boundaries of coarse twin grains through a bulging mechanism [91,83], which could also cause sub-grain formation within slip bands [91,84].

From the above, it can thus be generally assumed that the active DRX mechanism during processing of a material is governed by the Zener-Holloman value ($Z = \dot{\varepsilon}\exp(Q/RT)$ [92]), where $\dot{\varepsilon}$ is strain rate, Q is the activation energy for deformation, T is the absolute temperature and R is the universal gas constant. Controlling the Z value over

15

the course of deformation may yield the desired grain size and structure. However, regardless of the predominant DRX mechanism, the sharp texture induced by the deformation process persists through the recrystallization process [93-96]. Static and dynamic recrystallization have been proven to be ineffective tools in terms of texture modification in traditional Mg alloys, which stands as the most significant hurdle in Mg processing [32,35,97]. However, manipulating the nature of recrystallization remains an efficient technique to replace the sharp deformation texture with a randomly oriented microstructure. In this respect, recent trends of alloy design have opted the strategy to restrict normal recrystallization mechanisms that produce basal textures, hence allowing alternative mechanisms to produce more desired random textures.

2.1.3   Effect of rare earth elements on Mg workability

The concept of alloy design to improve metal formability is a very old practice in physical metallurgy [98], and Mg made no exception to this. Although numerous compositions have been investigated, there was a consensus that texture weakening is necessary for any alloy design strategy that aims at improving ductility of Mg alloys [15,41,99]. Combinations of RE elements and non-RE elements (e.g. Zn and Ca) has been by far the most widely used alloying strategy for Mg as it proved most efficient in reducing texture intensities and ameliorating ductility [40,100,35,101-104]. The idea is simple, one must decrease twin volume fraction by avoiding the single crystal-like behavior inherent of sharp textures. A decrease in twin volume fraction leads to a decrease in anisotropy and asymmetry. The enhancement in RT ductility of Mg-RE alloys has also been attributed to an enhanced activity of non-basal slip mechanisms, particularly prismatic $\langle a \rangle$ and pyramidal $\langle c + a \rangle$, thereby mitigating the propensity for

16

deformation twinning [60,105,96]. On the other hand, the RE texture modification effect is mainly associated with changes in the recrystallization phenomenon.

Recent investigations pointed out the critical role of recrystallization in RE texture formation [35,103,55]. As mentioned above, this effect was first explained based on the effect of RE elements on promoting particle stimulated nucleation [54]. On the other hand, other authors reported that RE element additions retard DRX during thermomechanical processing and instigates a greater number of shear bands comprising large orientation spreads. This aspect is considered crucial for triggering the RE effect because it determines the amount of deformation stored energy in the deformed microstructure. Shear band nucleation (SBN) of RE textures can be thus attributed to (a) a CDRX mechanism leading to sub-grain formation of basal and off-basal orientations and (b) subsequent preferential growth of the latter. This is explained by the fact that the mobility of low angle boundaries between basal recrystallizing nuclei and their basal parents is relatively much lower than the mobility of non-basal boundaries between off-basal RE nuclei and the basal-oriented matrix. This difference in boundary mobility is further exacerbated by GB pinning due to solute drag [51,55,40].

Interestingly, there are also cases, in which weak or random textures were reported in Mg-RE alloys that had a negligible amount of precipitates no shear bands to trigger PSN and SBN mechanisms. [105]. This prompted some authors to suggest a possible effect of solute clusters near GBs which may be able to trigger off other recrystallization mechanisms [106]. In lights of all these contentions, several parametric and mechanistic studies, including type and concentration of RE elements, were

17

conducted in hope of unraveling the key elements producing the RE effect seen on recrystallization of Mg-RE alloys [102,42,107,108].

In this paper, we review the burgeoning research on the effect of RE elements on both recrystallization and deformation in Mg alloys, and discuss key mechanisms reported in the literature in order to construct a hypothesis that can untangle this highly controversial topic. We pay special attention to the four most widely studied RE element additions – yttrium, cerium, gadolinium, and neodymium and try to identify common grounds in their assorted actions. Throughout the manuscript, we try to distinguish between the action of rare earth on deformation texture and that on recrystallization, and we analyze literature to determine which one is more predominant in each case of the various reported compositions. We have elected to keep the plan of this manuscript as simple as possible, by devising only four sections dedicated separately to the four aforementioned RE elements, and a section for ternary and complex alloys. We conclude by suggesting new research venues that have potential to reap the most significant impact of rare-earth additions to Mg alloys.

2.2   Mg-Y alloys

Yttrium, with a high solubility limit of 12.4 wt. % in Mg [109], is known to reduce the sharpness of the deformation texture of Mg and its alloys by altering the relative activity of deformation mechanisms (slip and twinning) and the interplay between recrystallization mechanisms (i.e. CDRX and DDRX) [60,58,102]. Compared to other RE elements, Y has probably the smallest influence on texture. In fact, after rolling and annealing, basal poles tilted toward RD, which is a typical feature of traditional Mg alloy sheets, are still salient in the obtained (0002) pole figure (Figure 2.3) [101].

Yttrium, however, seems to induce a noticeable change in the relative activity of slip systems.
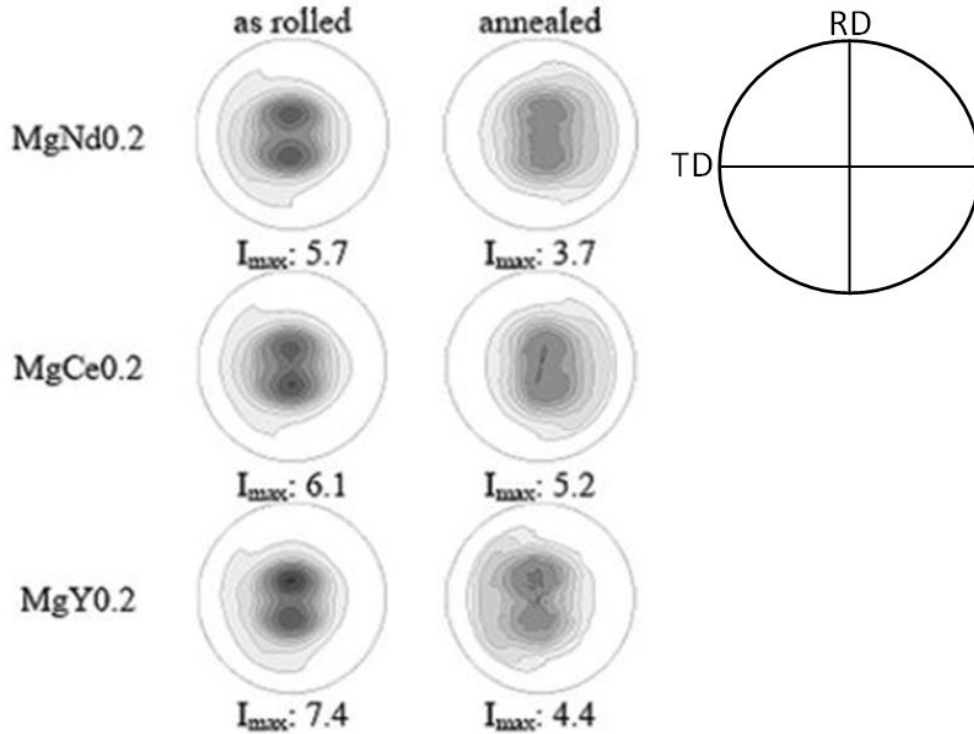
Figure 2.3   Recalculated (0002) pole figures for rolled binary Mg-RE alloys.

Rolling was conducted at 673 K (400 ºC) with 16 m/min rolling speed, and annealed at 673 K (400 ºC) for 20 minutes. Reproduced from [101] with permission from Elsevier

Agnew *et al*. [60] showed that alloying with Y increases the tendency of RD split basal textures during rolling due to the increased activity of non-basal $\langle c + a \rangle$ slip. Sandlöbes *et al.* [50] reported that proper additions of Y to pure Mg enhance the activity of compression and double twinning in addition to $\langle c + a \rangle$ slip. This increase in the diversification of deformation modes causes a more homogeneous strain distribution, and hence, generates a softer texture after recrystallization. These authors suggested that Y in substitutional solid solution reduces the I_1 stacking fault energy (SFE) on basal and

19

probably pyramidal planes, making $\langle c + a \rangle$ slip easier to activate [50,110]. The I_1 stacking fault (stacking sequence …ABABCBCB…) is bound by partial dislocations with lines lying in the basal plane, but Burgers vectors aligned with the pyramidal planes. Theoretically, it is able to act as a heterogeneous nucleation source for $\langle c + a \rangle$ dislocations [111]. This explanation falls in agreement with the results from density functional theory calculations by Muzyk *et al*. [112], which indicate that Y has a strong effect on the basal SFE.

However, Cottam *et al*. [58] suggested that the enhancement of $\langle c + a \rangle$ slip per say is not enough to cause any observed amount of texture weakening, which is more likely to arise from a change in the recrystallization mechanism. Hadorn et al. [55] reported in fact that for hot rolled sheets when Y concentration was between 0.03 at. % and 0.75 at. %, a transition occurs from a deformation regime dominated by basal dislocations to a regime dominated by prismatic dislocations. They concluded that the ease of prismatic slip could not be taken as responsible for the observed texture weakening as the deformation texture remains largely unchanged. The action of Y must have then taken place during dynamic recrystallization [55]. Bohlen *et al*. [35] have showed that recrystallized grains in a hot extruded bar containing Y have generally quite different orientations than the deformed grains typical of $\langle 10\bar{1}0 \rangle$ fiber texture. In these Y-containing alloys (MW11 grade – Mg-0.96 Mn-1.14 Y wt. %), large recrystallized grains (i.e. >5 μm) fall within the ED$\|$ $\langle 11\bar{2}1 \rangle$ texture component, dubbed RE-texture, while most small recrystallized grains either populate the $\langle 10\bar{1}0 \rangle$ fiber or are at best slightly tilted towards the $[20\bar{2}1]$ pole (Figure 2.4) [35]. They attributed the origin of the "RE texture" to the effect of RE elements on the nucleation and growth processes of grains.

20

Nucleation of the corresponding unique orientations was associated with the presence of shear bands. This hypothesis was later substantiated by Stanford and Barnett [40]. However, the aspect of GB pinning by Y solute atoms and its role in enhancing the growth advantage of RE-oriented nuclei was not greatly discussed.
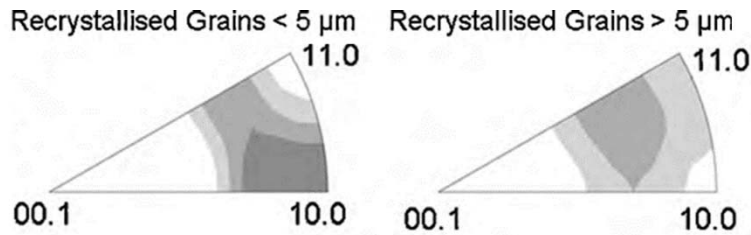
Figure 2.4   The Inverse pole figures (for small and large recrystallized grains) of the MW11 (Mg-0.96 Mn-1.14 Y (wt. %)) alloy.

Extruded at 573 K (300 ºC) with 30:1 extrusion ratio. Reproduced from [35] with permission from Elsevier.

Hantzsche *et al.* [101] showed that annealing after rolling would further decrease the intensity of texture. This texture evolution process was attributed to the nucleation of new orientations on twins inside deformation bands followed by their preferred grain growth, which ultimately leads to the RE-texture alongside off-basal dominant components. They reported that restricted grain growth and texture weakening could simultaneously be the result of pinning effects from solute segregation or particles. Further, they demonstrated that the RE-texture develops only after a critical concentration threshold is reached for all the investigated elements. The maximum texture intensity vs. the RE elements content is plotted in Figure 2.5. The critical concentration for noticeable drop of texture intensity, about a half of order of magnitude, can be clearly seen in all RE

elements [101]. Additionally, Jung *et al.* [113] plotted the critical amount of RE elements

needed for texture randomization based on several works in literature.
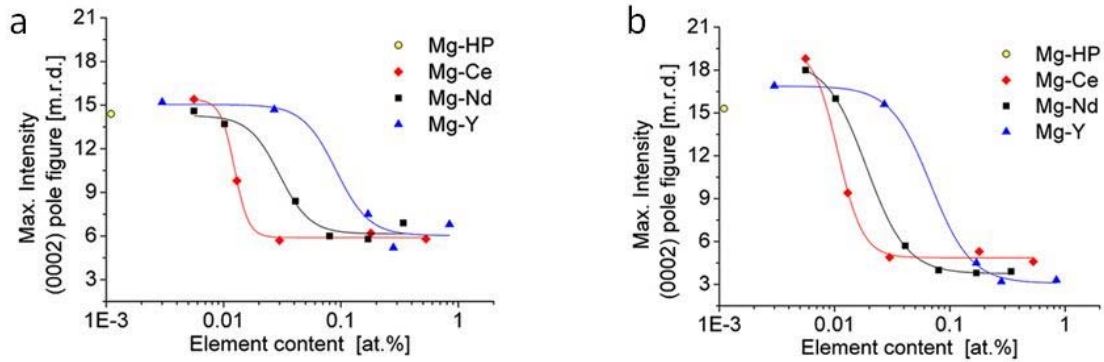
Figure 2.5   Maximum (0 0 0 2)-pole figure intensity for binary Mg-RE alloys.

a) In as-rolled condition b) After annealing (accuracy of the texture measurements is
±0.2). Reproduced from [101] with permission from Elsevier.

The texture intensity drop takes place at concentrations well below the solubility

limit of each RE element, which may rule out the effect of precipitates and related PSN

mechanism. Stanford [102] reported similar tendencies for extruded binary Mg-Y alloys.

The inverse pole figures used are reproduced in Figure 2.6 and show that texture

randomization takes place after adding 0.04 at. % Y and becomes highly effective at 0.17

at. % Y.

Considering the high solubility of Y in Mg and the absence of noticeable

precipitation in the corresponding microstructures, texture weakening that Y produces

could be attributed to the strong interaction of Y solute atoms with dislocations and GBs

[102]. However, as aforementioned, Y may be expected to be a less effective texture

modifier compared to other RE elements (i.e. Lanthanum) due to its smaller atomic

radius (closer to that of Mg), and hence, weaker atomic interactions with Mg atoms

22

[114]. As such, effect of RE elements cannot be totally attributed to their large atomic size difference with Mg, as the unique electron orbitals of the lanthanides play a role in reducing GB and SF energies that is not yet entirely clear. Moreover, other atoms with similar radial disparities, such as Pb were not reported to have as much effect on Mg properties as Y.

Pure Magnesium		Yttrium series	
max = 3.3 Grain size = 69 μm	0001 — $\overline{1}2\overline{1}0$ 01$\overline{1}$0	0.02 at% Y max = 3.2 Grain size = 72 μm	
		0.04 at% Y max = 4.1 Grain size = 45 μm	
		0.07 at% Y max = 3.8 Grain size = 18 μm	
		0.17 at% Y max = 4.4 Grain size = 16 μm	
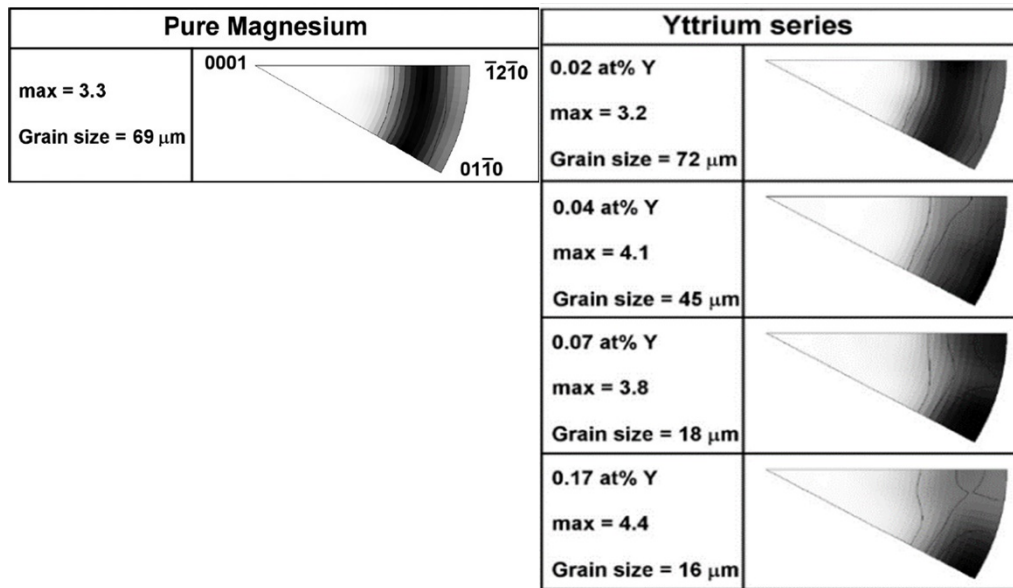
Figure 2.6   Texture data for binary Mg-Y alloys.

Invers pole figure refers to extrusion direction. Reproduced from [102] with permission from Elsevier.

With respect to the important effect of solute segregation to GBs on retarding the GB mobility, Hadorn et al. reported a substantial reduction of grain growth for alloys with medium concentration of Y (i.e. 0.23 at. %) [55]. Cottam et al. [58] suggested that the segregation of Y atoms to GBs renders the bulging mechanism to form DRX nuclei difficult. Hence, conventional DRX by strain induced boundary migration would be restricted compared to other mechanisms that do not rely on high angle boundary

23

migration, such as CDRX. However, the process of sub-grain rotation into recrystallized grains with high angle boundaries (CDRX) does not seem a viable means for forming random textures during the course of annealing. In fact, the intragranular misorientation axis (IGMA) analysis performed in processed Mg-Y alloys indicated increasing IGMA shifts from $\langle uvt0 \rangle$ within the basal plane to [0001] as a function of rising Y concentration from 0.03 to 0.75 at. % [55]. For intermediate concentrations, the IGMA axis would be a direction between $\langle uvt0 \rangle$ and [0001] (i.e. $\langle uvtw \rangle$) [55]. At higher Y concentrations when the IGMA (or Taylor) axis was close to the [0001] axis, texture randomization, particularly upon annealing, was evident. The prevalence of the [0001] Taylor axis is typically indicative of high prismatic slip activity, which has been suggested to promote CDRX, and thereby induce a texture modification. However, if we consider the formation of an extrusion RE-texture that engages a texture transition from $\langle 10\bar{1}0 \rangle$ to $\langle 11\bar{2}1 \rangle \parallel$ ED, it becomes clear that such a rotation cannot take place around the [0001] Taylor axis, and hence, cannot be ascribed to the enhanced role of prismatic slip, and the promotion of non-basal slip in general. Instead, it can be attributed to preferred growth characteristics of DRX nuclei with the ED $\parallel \langle 11\bar{2}1 \rangle$ orientation over other orientations close to that of the deformed matrix.

It is worth mentioning that favorable off-basal orientations of DRX nuclei could potentially form in traditional Mg alloy sheets or extrusions as well, provided the onset of DRX can be delayed to higher strains. However during recrystallization growth, basal oriented grains (basal plane parallel to RD or ED) seem to eclipse any off-basal oriented nuclei giving rise to the common basal or $\langle 10\bar{1}0 \rangle$ fiber texture. In this regard, Agnew *et al.* [32] showed that rolled AZ31B sheets can develop an RD-split basal texture after

rolling, which seems to disappear after further annealing treatments in favor of a very sharp, single-peak basal texture. Moreover, Hantzsche et al. [101] showed that dilute Mg-Y alloys tend to sharpen their deformation texture, whereas annealing of these alloys was found to weaken the texture, particularly for higher Y concentrations. Hence, it could be hypothesized that Y addition not only affects active deformation mechanisms and provides unique nucleation sites for RE-textured nuclei, but also alters the growth preference through changing the characteristics of GB mobility in the course of recrystallization.

2.3   Mg-Ce alloys

Having the lowest solubility limit in Mg (0.1 at. % or 0.5 wt. %) among all other explored RE elements, Ce is one of the strongest potential texture modifiers known for wrought Mg alloys [102,15]. As can be clearly observed in Figure 2.5, Ce weakens deformation and annealing textures at concentrations as small as 0.01 at. %, but this effect quickly levels above 0.03 at. % Ce content. Ce-containing Mg alloys develop a relatively softer texture away from the basal texture over a wide range of bulk compositions. Off-basal textures would develop upon annealing regardless of the processing temperature (423-673 K (150-400 ºC)) [43]. Hadorn *et al.* [56] suggested that the superior efficacy of Ce has to do with its low solubility limit compared to other RE elements (i.e. the critical concentration required to trigger the RE-effect scales with the solubility in Mg) [115,116]. To compare the effects of Ce and Y on texture, Hadorn *et al.* [56] hypothesized that the pinning effect of small particles (i.e. smaller than the threshold limit for PSN) would retard normal DRX by strain-induced boundary migration and thus promote the activity of CDRX and/or shear band DRX mechanism. Hence, for Ce, the

texture weakening effect took place at lower concentrations than for Y (i.e. less solute was needed owing to the pinning effect of fine Mg-Ce particles). The authors also suggested that the critical alloy composition to induce texture modification depends on the solubility of each RE element in Mg, rising with increasing solubility. In another study, Al-Samman *et al*. [41] demonstrated that the occurrence of PSN in Mg alloys with a combination of RE and non-RE elements is actually associated with non-RE element containing particles (i.e. Zr containing particles for Mg-Zn-Zr-RE alloys). RE element-containing particles, when they exist, may not have a major contribution to PSN due to their very fine dispersion in the matrix, which could obstruct dislocation motion and GB mobility in the course of deformation and DRX.

Despite the reported significant contribution of Zener pinning to texture weakening, most currently studied Mg alloys containing Ce still opt for very low alloying content (e.g. 0.2 wt.% of Ce) to achieve the texture weakening effect, which seems to saturate at concentrations much below the solubility limit of Ce. This indicates that PSN is not always a viable mechanism for controlling the RE effect [117,97]. At elevated annealing temperatures, texture weakening becomes subject to the interplay between GB pinning and particle coarsening. For a rolled Mg-1wt.% Ce alloy, Basu *et al*. [118] reported that $Mg_{12}Ce$ second-phase particles form "stringers" during large strain rolling (80% total reduction in one pass), which impede the oriented growth phenomena of RE nuclei despite the presence of massive shear bands in the deformation microstructure. The process eventuates in sharper basal textures during subsequent annealing treatments. In general, Ce addition is reported to have a minor effect on annealing grain size [119].

At higher concentrations, precipitates adopt a string-like morphology (Figure 2.7) which significantly reduces availability of sites where more grain orientations could nucleate.
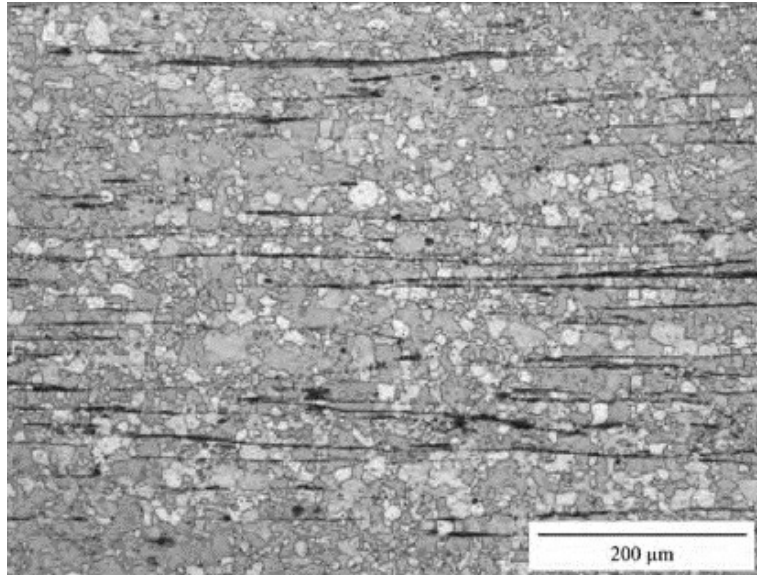
Figure 2.7   The microstructure of a Mg- 0.95 Mn- 0.86 Ce (wt. %).

Extruded at 573 K (300 ºC) with extrusion ratio of 30:1. Reproduced from [35] with permission from Elsevier.

For this range of concentrations (i.e. 0.49 at. %), TEM investigations revealed an increased presence of non-basal $\langle a \rangle$ dislocations and dislocations with $\langle c \rangle$ component alongside $\langle c + a \rangle$ dislocations. These dislocations produce a high strain gradient from mantle to core regions, thereby altering the dynamic recrystallization mechanism [56]. Chino *et al.* [97] documented that addition of Ce does not produce much change in the c/a ratio of the Mg alloy, rather it changes the SFE values to favor more active non-basal dislocations. Actually, the boost in the activity of $\langle c + a \rangle$ and non-basal $\langle a \rangle$ type dislocations seems to be a common feature for most Mg alloys with sufficient content of RE elements.

Notably, Stanford *et al*. [102] proved that grains tend to rotate from the $\langle 10\bar{1}0 \rangle$ pole toward the $\langle \bar{1}2\bar{1}1 \rangle$ pole as an effect of Ce on recrystallization process (Figure 2.8). The angle between these poles is approximately ~34.2º, and seems consistent with the rotation angles (40º-50º) reported by Mishra *et al*. [120] of the basal poles toward the extrusion direction for the same type of alloys (Figure 2.9). Accordingly, the final texture exhibits approximately 56% of grains, which have a macroscopic Schmid factor of about 0.4 for basal slip when loaded accordingly, i.e. along the extrusion direction. The rest of grains show orientations typical of the CDRX mechanism in traditional Mg alloy, which would corroborate the anisotropic behavior. Such high basal activity would improve ductility, but not to the point observed for this texture as dislocations with non-basal Burgers vectors must have drastically contributed to the overall deformation process [120]. These correlations between grain size and grain orientation suggests a particular effect on the mechanical properties, but in a way that is yet to be identified.

Preferred growth of grains with RE-texture orientations has also been observed for Mg-Ce alloys [35] (Figure 2.10), and it is rather common for most of Mg-RE alloys. However, the average grain size for Mg-Ce alloy extruded at 673 K (400 ºC) with extrusion ratio of 25:1 was found to be approximately 36 μm, which is well above the grain diameter for grains with RE-texture, usually 5 μm to 10 μm.

Mishra et al. [120] measured the stress-strain curve under tension along the extrusion direction for Mg-0.2 wt. % Ce alloy and a pure Mg polycrystal (Figure 2.11). The alloy clearly displayed a higher uniform elongation but lower yield stress compared to extruded pure Mg.
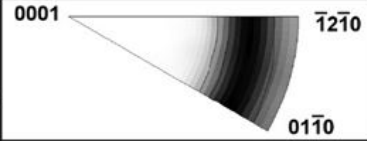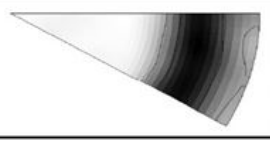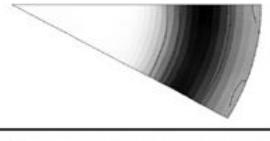
Pure Magnesium		Cerium series	
max = 3.3 Grain size = 69 μm	0001 ─── 1̄21̄0 011̄0	0.009 at % Ce max = 3.1 Grain size = 56 μm	
		0.016 at % Ce max = 3.4 Grain size = 58 μm	
		0.04 at % Ce max = 2.5 Grain size = 14 μm	
		0.06 at % Ce max = 2.4 Grain size = 11 μm	
		0.08 at % Ce max = 2.3 Grain size = 8 μm	

Figure 2.8   Texture data for binary Mg-Ce alloys.

Where the invers pole figures refer to extrusion direction. Reproduced from [102] with permission from Elsevier.
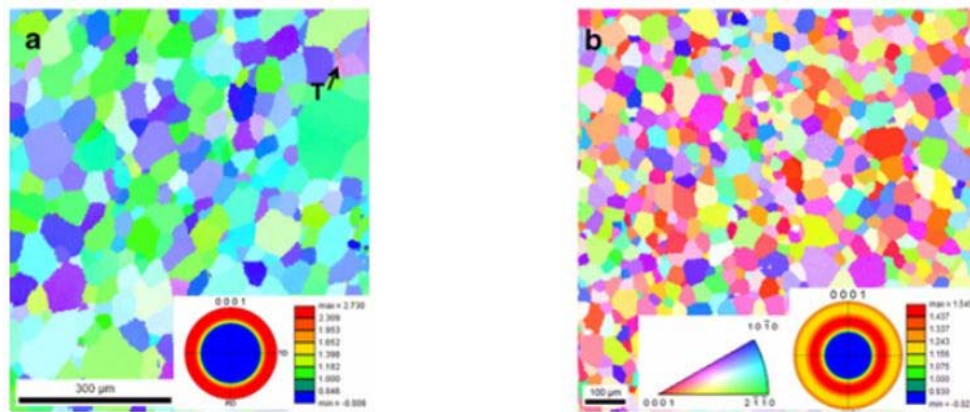
Figure 2.9   EBSD data and axial texture plots for extruded a) Mg and b) Mg- 0.2 wt. % Ce alloy.

At 673 K (400 ºC) and extrusion ratio of 25:1 with maximum intensity of ~2.7 and ~1.5, respectively. Reproduced from [120] with permission from Elsevier.
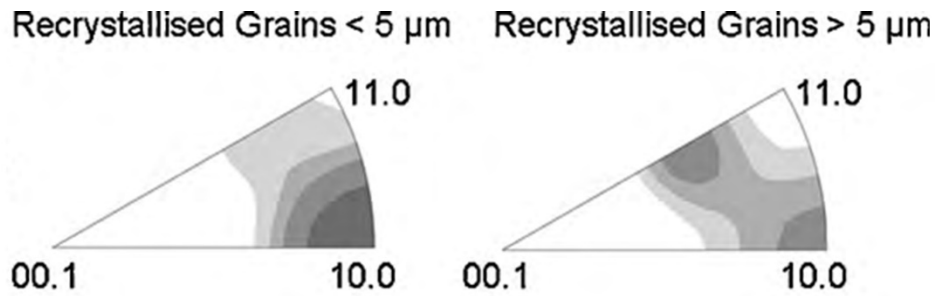
Figure 2.10   The Inverse pole figures (for small and large recrystallized grains) of the
ME11 (Mg-0.95 Mn-0.86 Ce (wt. %)) alloy.

Extruded at 573 K (300 ºC) with 30:1 extrusion ratio. Reproduced from [35] with permission from Elsevier

The lower tensile yield stress can be ascribed to the favorable orientation of grains to deform by basal slip for the Ce-containing alloy, while the yield in the pure Mg is controlled by several deformation mechanisms requiring higher CRSS values than basal slip (e.g. prismatic slip and contraction twinning). However, the same amount of contraction twinning was observed in the microstructure of both materials for strains above 20%. Thus, the essential difference in the behavior was due to the higher slip activity in the Mg-Ce alloy which led to an intra-granular average misorientation of about 7º compared to 3º for pure Mg [120]. Higher dislocation activities in the Mg-Ce alloy was probably assisted by a drop in the CRSS values for non-basal slip which would also promote less stress concentrations and thus less strain localization events [121,120]. Chino et al. [117] have reported that higher activity of non-basal dislocation improves compressive elongation of Mg at room temperature. However, the higher flow stress and lower formability of Mg-Ce alloys compared to pure Mg at elevated temperatures (i.e. > 573 K (300 ºC)) was attributed to a substantial retardation of DRX compounded to a Ce-induced lower diffusion effects [117].
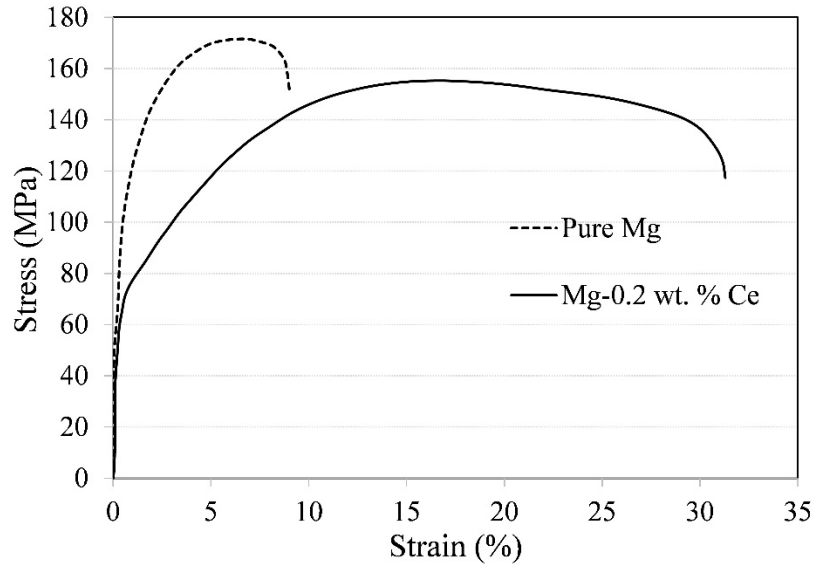
Figure 2.11   Stress-strain curves in tension for a pure Mg polycrystal and a Mg-0.2 wt. % Ce alloy.

Tensile testing was conducted at room temperature with an average strain rate of $0.66 \times 10^{-3} \ s^{-1}$. Materials were extruded at 673 K (400 °C) with an extrusion ratio of 25:1. Reproduced from [120] with permission from Elsevier.

DRX retardation in Mg-Ce alloys is accompanied by extensive double twinning inside shear bands, which cause the basal planes to align themselves with the shear bands, causing much of the observed texture softening, absent in pure Mg [121,97].

Compared to other Mg-RE alloys, Ce-containing Mg alloys exhibit lower formability irrespective of the direction of applied load. The lower elongation to fracture has been attributed to brittle Ce-containing second phase precipitates [41,35] that thus act in opposition to Ce's supreme capability to advantageously modify the recrystallization texture. Both effects are correlated to Ce's low solubility in Mg, which is thus demonstrated to simultaneously have both favorable and detrimental effects on Mg formability.

31

Overall, Ce and Y seem to have similar tendencies in affecting recrystallization texture and enhancing $\langle c + a \rangle$ slip. Ce, however, seems to modify the texture more significantly and without much segregation into the GBs [117]. In a Mg-1.3 wt. % Ce alloy, Ce was observed to preferentially segregate onto certain atomic planes causing relatively large distortions [122]. However, the subsequent effects on texture evolution is still largely unknown. Despite the similarities in the type of texture induced by Y and RE elements, their corresponding effects on the dislocation and GB characteristics appear to be very much in variance.

2.4   Mg-Gd alloys

Having a relatively high solubility in Mg, Gadolinium (Gd) is known to be an efficient but yet a cost-prohibitive grain refiner, solid solution strengthener, and texture modifier for Mg [123-128]. As illustrated in Figure 2.12, Gd improves the mechanical strength at room temperature, only to cause a substantial loss in ductility [129-131]. Gd presence also tends to increase the extrusion force and decrease the final average grain size by as much as 75% [102]. However, addition of Y to the Mg-Gd system results in an improved ductility [129], and it is not quite clear yet how Y atom compensate for the deleterious effect of Gd. Al-Samman *et al.* [41] reported that thanks to a more even polar distribution of basal poles along different sheet directions, Gd-containing Mg-Zn-Zr systems express the highest strain hardening rate and the highest planar isotropy among all the RE element-containing alloys. Actually, superior ductility for Mg-Gd-Zn alloys was reported by Wu *et al.* [128], and the reasons why Gd effects are quite different in the ternary or complex alloying systems are yet to be investigated.

32
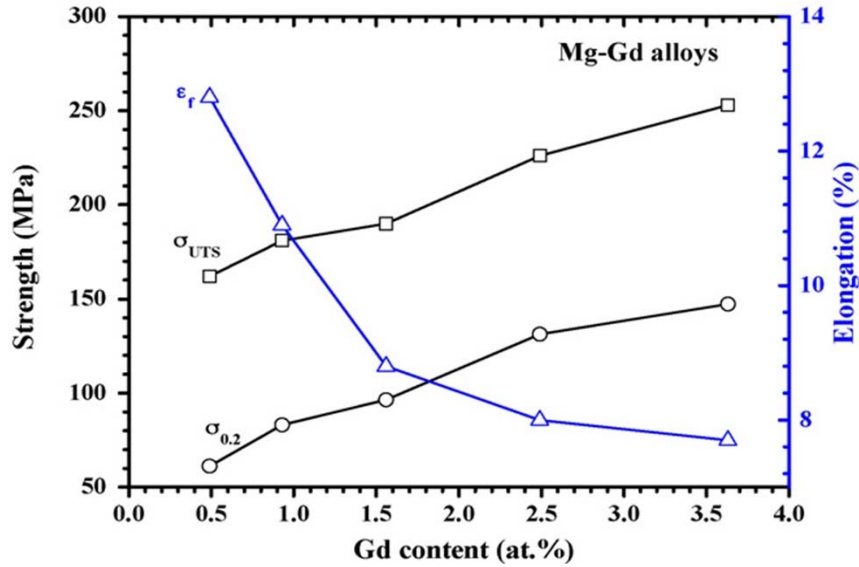
Figure 2.12   Tensile characteristics of the Mg–Gd alloys against the concentration of Gd.

$\sigma_{0.2}$ is the 0.2% proof strength; σ_{UTS} is the ultimate tensile stress; and e_f is the elongation-to-failure. Reproduced from [129] with permission from Elsevier.

Depending on recrystallization temperature, Gd is widely known to handily temper texture at concentrations as small as 600 ppm (Figure 2.13) [41,107,40,113]. Gd is practically soluble at 473 K (200 ºC) even at 4 wt. % concentrations, which totally rules out any potential PSN effects [114]. Accordingly, Gd must act from its solid solution state, either on GBs during the recrystallization phase or on the process of deformation preceding nucleation and growth [102].

Mg-Gd binary alloys develop an RE-texture that resembles the Mg-Ce series, but with the addition of a small (2%) texture component oriented within 5º of $\langle 10\bar{1}0 \rangle \| ED$, which typically survived from the deformation process (Figure 2.14) [102]. Texture is generally pretty random, but the famed RE-texture can be easily discerned from the

33

overall background, and it seems that the corresponding grains tend to tilt away from

$\langle\bar{1}2\bar{1}0\rangle$ toward [0001] pole as Gd content increases [102].
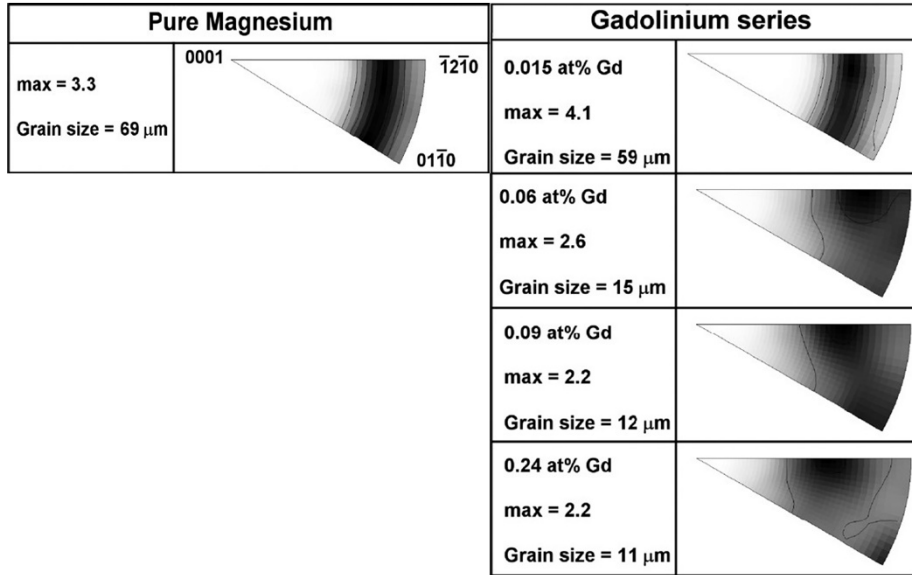
Figure 2.13   Texture data for binary Mg-Gd alloys.

Invers pole figures refer to extrusion direction. Reproduced from [102] with permission from Elsevier.

When concentrations of Gd exceed 4 wt. %, split basal poles tend to merge together in the [0001] pole figure, while the RE-texture disappears from the inverse pole figure (Figure 2.15) [107].

This change may be explained by the considerable segregation of Gd in GBs, which could trigger intergranular precipitation, and as such, eliminate either the beneficial effect of Gd solutes or the preferred growth of grains with random orientations [107]. Al-Samman *et al.* [41] have shown that the addition of 0.73 wt. % of Gd to a ternary Mg-Zn-Zr system would not split the basal poles during a warm rolling at 673 K (400 ºC), but only tilts them uniformly toward the TD direction by ~42º.
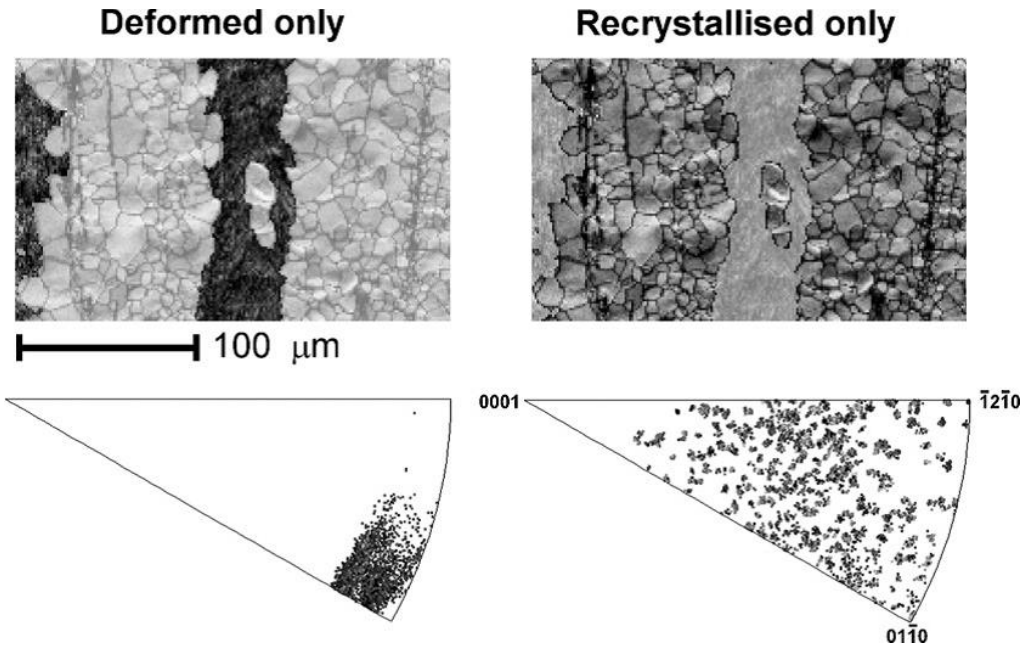
Figure 2.14   EBSD analysis of a 0.24 at. % Gd alloy extruded at 415 ºC with an area
reduction ratio of 30 for deformed and recrystallized grains.

Extrusion direction vertical on orientation maps; inverse pole figures refer to the
extrusion direction. Reproduced from [102] with permission from Elsevier
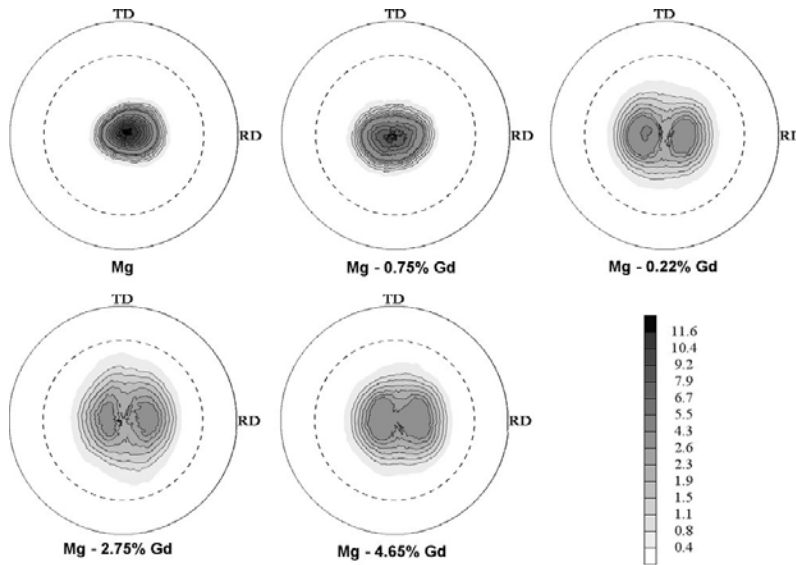
Figure 2.15   Pole figures for Mg-Gd binary alloys obtained using X-ray diffraction.

Specimens were subject to two hot rolling passes with a 50% area reduction and were
annealed to produce fully recrystallized microstructures with the grain size of 10 μm.
Reproduced from [107] with permission from Elsevier.

Moreover, it further weakens texture during a one hour post annealing at 673 K (400 ºC) (Figure 2.16), which was accompanied by considerable grain growth in the microstructure. The more random orientations of DRX grains in these alloys was attributed to the nucleation stage, but no formal explanation proved decisive yet on the matter [102]. Other researchers explained that formation of off-basal nuclei on shear bands and their preferred growth due to inherent deformation heterogeneities within shear bands drive this texture weakening process [118]. Considering the loss of texture randomization capability of Gd together with its grain refining properties [132], one may reasonably assert Gd acts through a change it produces on the character of GBs.
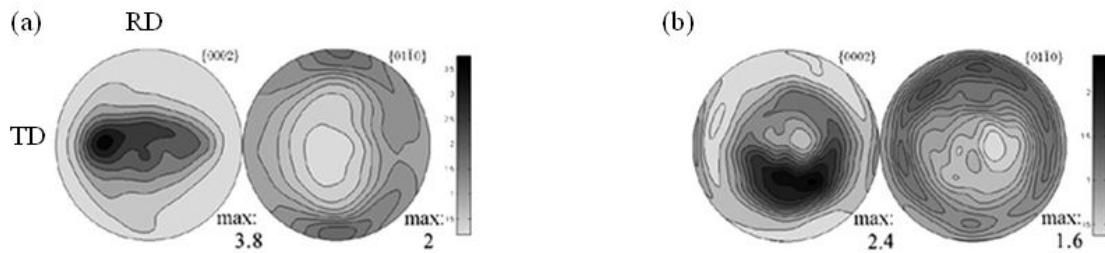
Figure 2.16   Pole figures for a Mg-Zn-Zr alloy containing 0.73 wt. % Gd.

a) Rolling at 673 K (400 ºC) with a 75% reduction in thickness and, b) Annealing for 1 hour at 673 K (400 ºC). Reproduced from [41] with permission from Elsevier

According to Al-Samman *et al.* [41], the atomic weight of Gd should not be overlooked either, it has all the potential to alter the grain growth preference in terms of their intra-granular orientation. The abundance of high angle GBs with misorientation angles in the range of 70º to 75º at the $\langle 11\bar{2}0 \rangle$-$\langle 10\bar{1}0 \rangle$ fiber (Figure 2.17a) is not a common stand in a typical IPF of wrought Mg alloys, so they may be well correlated with

36

special reorientations that are particularly favored in Gd-containing alloys [41]. The coexistence of recrystallization GBs ($30^{\circ}\langle 0001 \rangle$) and extension twin boundaries ($86^{\circ}\langle 11\bar{2}0 \rangle$) within a $\langle 11\bar{2}0 \rangle$-$\langle 10\bar{1}0 \rangle$ fiber (Fig. 18) testify to the parallel activity of special Gd-driven recrystallization mechanisms alongside deformation and DRX mechanisms that are active in traditional Mg alloys.

Yamasaki *et al.* [126] have observed the segregation of Zn and Gd atoms into stacking faults at medium temperatures (673 K (400 ºC)). The formation of 14H long period stacking ordered structure (LPSO) with a $Mg_{97}Zn_1Gd_2$ (at. %) stoichiometry was also noticeable at high temperatures (>723 K (450 ºC)). Effect of these precipitates are properly addressed in section 6. Moreover, Nie *et al.* [132] reported that Gd and Zn potentially segregate and form a dimer in the core of basal dislocations, which become rather sluggish. They hypothesized that formation of Shockley partial dislocations ($b = 1/3\langle 10\bar{1}0 \rangle$) leads to an MgGdZn-type phase, named the $\acute{\gamma}$ phase, having a disordered hexagonal structure (Figure 2.17b). These authors also demonstrated the periodic segregation of Gd and Zn atoms into ($10\bar{1}2$) twin boundaries [133], which could potentially influence the dislocation activity, the nucleation process of DRX grains, as well as the grain growth preference. All aforementioned processes would be more or less influential where the reorientation of an undeveloped grain would settle, opening the opportunity for new texture components to emerge. All reported textures suggest that both CDRX and DDRX mechanisms are active in the course of dynamic recrystallization, with an interplay sensitive to the amount of Gd present in solid solution.
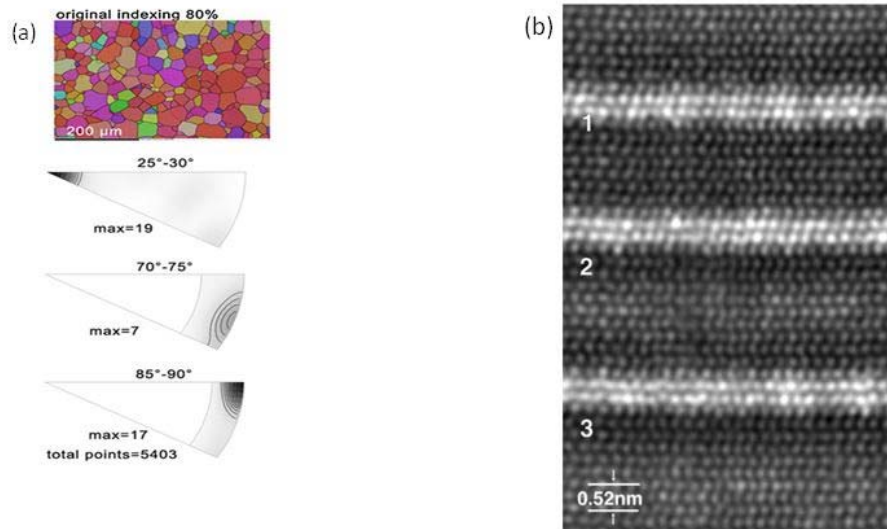
Figure 2.17   EBSD and TEM micrographs for MG-Gd alloys.

a) IPF for the recrystallized microstructure of a Gd-containing alloy and the corresponding axis/angle misorientation distribution for select angle pairs with high misorientation densities. b) Fourier filtered HAADF-STEM image of three precipitates $\acute{\gamma}$ from $\langle 11\bar{2}0 \rangle$ formed in Mg–1Gd–0.4Zn–0.2Zr (at. %) aged at 523 K (250 ºC) for 2 h. Reproduced from [41] and [132], respectively with permissions from Elsevier.

Another important effect reported for Gd relates to the widespread formation of shear bands that have been long seen to promote DRX, owing to the high strain gradients they comprise. Stanford and Barnett [40] reported that addition of 1.55 wt. % of Gd is enough to start seeing shear bands with two different orientations with respect to the extrusion direction (Figure 2.18). Using full pole figures of the partially recrystallized microstructures, they demonstrated that basal poles of recrystallized grains are approximately perpendicular to the shear bands on which they nucleate and grow [40], which explains the observed texture component on the corresponding IPFs. In more explicit terms, shear bands that are nearly parallel to extrusion direction produce $\langle 1\bar{2}10 \rangle$ fibers, while those inclined at ~25º produce RE-texture around the $\langle 1\bar{2}11 \rangle$ pole.
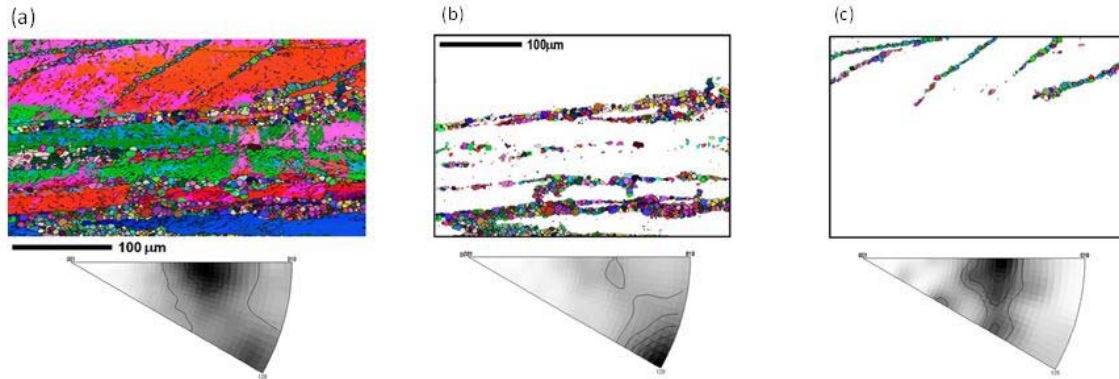
Figure 2.18   EBSD maps of the extruded Mg-1.55 wt. % Gd alloy.

Extruded at 688 K (415 ºC) with extrusion ratio of 30:1 with their corresponding IPFs referring to extrusion direction; a) full map, b) shear bands aligned with extrusion direction, c) shear bands inclined at ~25º to extrusion direction. Reproduced from [40] with permission from Elsevier.

According to these authors, since the angle between $\langle 1\bar{2}10 \rangle$ and $\langle 1\bar{2}11 \rangle$ in pure Mg with c/a ratio of 1.624 is ~28º, one can confidently hypothesize that the origin of this type of texture (RE-texture) is the orientation of shear bands with respect to extrusion direction. However, RE-texture has been observed in quite a few thermo-mechanically processed Mg-RE alloys without shear bands and with exactly that specific orientation, indicating the activity and/or dominance of other mechanisms discussed above [101,102,107,108].

2.5   Mg-Nd alloys

Nd is known to have a very low solubility limit in Mg, which depends on the purity of the raw element [114], (~0.1 at. %), and was found to noticeably weaken the texture starting from concentrations as small as 0.04 at. % [105,134-137]. Although the texture randomization occurs below the solubility limit, the systematic formation of a metastable phase Mg3Nd mask any potential effect of solutes [138,103]. Hadorn et al.

[103] showed that this metastable phase forms during hot rolling, whilst post annealing only contributes to coarsening them. They also reported that Zener drag is active in alloys with softer texture, which exhibits a relatively higher concentration of Nd (i.e. 0.095 at. %). However, no distinct correlation between the actions of Zener drag and texture weakening was observed. Still, the formation of RE-texture in other Mg-RE alloys having no precipitates in the microstructure, such as Mg-Y alloys, suggest considering the common ground for RE elements, e.g., their possible effects on dislocation dynamics and GB characteristics.

Segregation of Nd to GBs, whether in form of solutes or precipitates, upsets their mobility and interfacial energy. Hirsch et al. [2] reported the formation of some precipitates at the GBs of a Nd-containing alloy in a homogenized condition (Figure 2.19), but couldn't clearly determine the effect they produce on nucleation and growth of new orientations. In a Mg-1Mn-1Nd wt. % (MN11) extruded at 548 K (275 ºC), Hidalgo-Manrique et al. [105] demonstrated the formation of Mg3Nd (coherent DO19 phase β'' or semi-coherent hexagonal phase β') with a significant effect on the texture randomization. β'' and β' phases form along prismatic planes and increase the CRSS of basal slip, and hence, allow a more substantial activity of other pyramidal systems such as extension twinning [105].

The other phenomenon sustaining the occurrence of twinning is the transition from the dominance of $\langle a \rangle$ basal dislocations to that of $\langle a \rangle$ prismatic dislocations similar to other RE element-containing alloys [103]. Presence of numerous basal and prismatic dislocations in Mg-Nd alloys is conceivable, and would generate much deformation inhomogeneity (i.e. deformation stored energy gradient in the material) and able to

sustain the formation of deformation twins, namely compression and double twins
(Figure 2.20) [101].
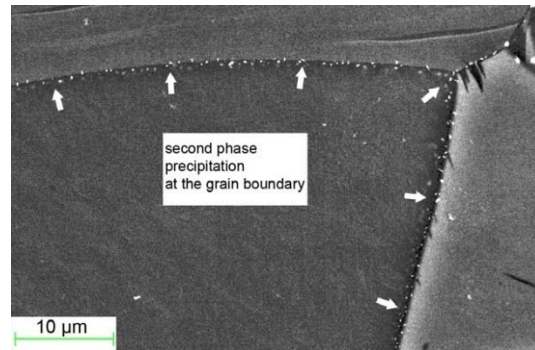
Figure 2.19   SEM micrograph of the Mg-0.6Nd-0.6Zn-0.3Zr (wt. %) alloy.

Picture was taken after homogenization treatment at 673 K (400 ºC) for 12 hours
followed by water quenching. Reproduced from [2] with permission from Elsevier.
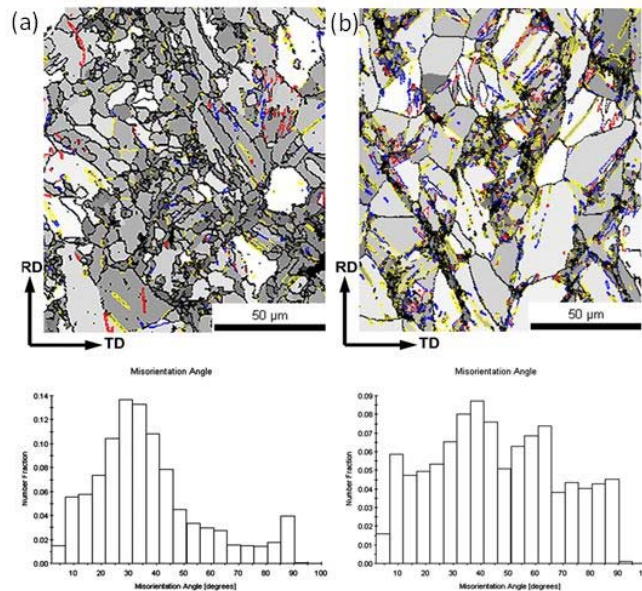
Figure 2.20   EBSD orientation maps along with the misorientation angle distribution in
as rolled (673 K (400 ºC)) condition for: a) Mg-0.01Nd, and b) Mg-0.04Nd
(at. %) alloys.

Mechanical twins are depicted by colored lines; red: tensile twins; blue: compression
twins; yellow: double twins. Reproduced from [101] with permission from Elsevier

Formation of different types of twins along with potential symmetric tilt boundaries with [0001] and $\langle uvt0 \rangle$ tilt axes makes the misorientation distribution more even throughout the grain misorientation range [101,139,140]. Therefore, the probability for nucleation of DRX grains is enhanced, as the orientation relationship between the nuclei and the parent phase might be dictated by the GB structure in question. Notably, twins were formed preferentially inside shear bands which have a "direct correspondence" to the newly formed grains [101]. In this case, shear bands with a high amount of stored strain energy are preferred sites for DRX nucleation. However, the mechanisms through which DRX grains with RE-texture orientations nucleate in these shear band are still elusive.

Furthermore, formation of twins could develop new texture components by rotating the lattice around their corresponding Taylor axis [55]. The existence of the $[0001]||ED$ component in IPFs for extruded Nd-containing alloys has been reported by Hidalgo-Manrique et al. [105]. They seem to argue on the basis of nucleation as the rate limiting step, that the basal component in the texture of extruded MN11 alloy appears when the $[11\bar{2}0]||ED$ texture vanishes (Figure 2.21), [105]. On the other hand, such a texture component can also emerge after hot compression along ED, and can be attributed to the lattice rotation that $\{10\bar{1}2\}$ twins would typically produce [9].

Figure 2.22 demonstrates that a basal texture in MN11 can be classically generated by activity of deformation twins [141-143]. Hence, one may assume that grains with a basal texture component are generated due to extension twinning in the $[11\bar{2}0]$ grains, which could be followed by an overwhelming TDRX leaving no trace of prior twinning in the microstructure.
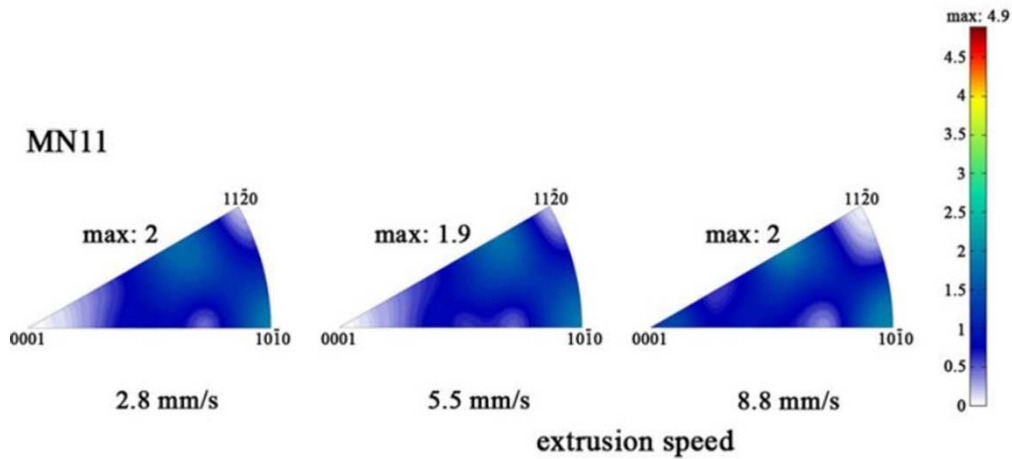
Figure 2.21   IPFs for the MN11 alloy in extrusion direction.

Extrusion was conducted at 548 K (275 ºC) with extrusion ratio of 30:1. Reproduced from [105] with permission from Springer.

Moreover, the orientations within $[11\bar{2}1] - [10\bar{1}1]$ arc seem to preserve their orientation during compressive deformation along the extrusion direction, which could signal the predominance of prismatic slip having the [0001] Taylor axis. In other words, rotation around [0001] axis would move the poles along the $[11\bar{2}1] - [10\bar{1}1]$ arc and, as such, would result in the formation of the same texture patterns observed in the corresponding IPF, alongside low energy [0001] tilt boundaries in Nd containing alloys, leading to higher intensities around $[11\bar{2}1]$ and $[10\bar{1}1]$ poles. However, as aforementioned, the formation of such orientations could be the consequence of a broader range of DRX grains nucleating, with prismatic slip only rotating them along the $[11\bar{2}1] - [10\bar{1}1]$ arc.

After nucleation on the mentioned sites, growth advantage of DRX grains may play a remarkable role in further texture evolution. Figure 2.23a presents IPFs for small

43

(<5 μm) and large recrystallized grains (>5 μm) of an Mg-0.95Mn-0.94Nd wt. % alloy

extruded at 573 K (300 ºC) with a 30:1 extrusion ratio [35].
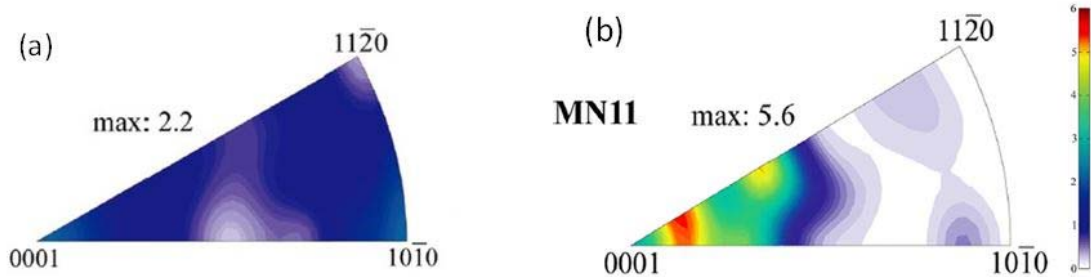
Figure 2.22   IPFs for a Mg–1.0Mn–1.0 wt. % Nd (MN11) alloy.

a) Extruded at 623 K (350 ºC) with the extrusion ratio of 30:1, and, b) Compressed along extrusion direction at an initial strain rate of 10^{-3} S^{-1}. Reproduced from [141] with permission from Elsevier.

Small grains strikingly follow a $\langle 10\bar{1}0 \rangle - \langle 11\bar{2}0 \rangle$ fiber tilted about 14° to 16º

toward ED, which is the typical texture of high purity Mg [102]. On the other hand,

larger grains are sharply concentrated around the $\langle 11\bar{2}1 \rangle$ pole. Since there is not a high

density of grains oriented around $[10\bar{1}0]$ pole, Nd seems to be a more effective producer

of RE-texture than its Ce and Y counterparts (Figure 2.4 and Figure 2.11). There was no

difference observed, as expected, between the deformation textures of Nd-containing

alloys and other RE element-containing alloys (Figure 2.23b). It should also be noted that

the activity of different slip/twinning systems is also affected by dynamic strain aging in

Nd-containing alloys, which could play a non-negligible role, though minor, in the

texture evolution [143,144].
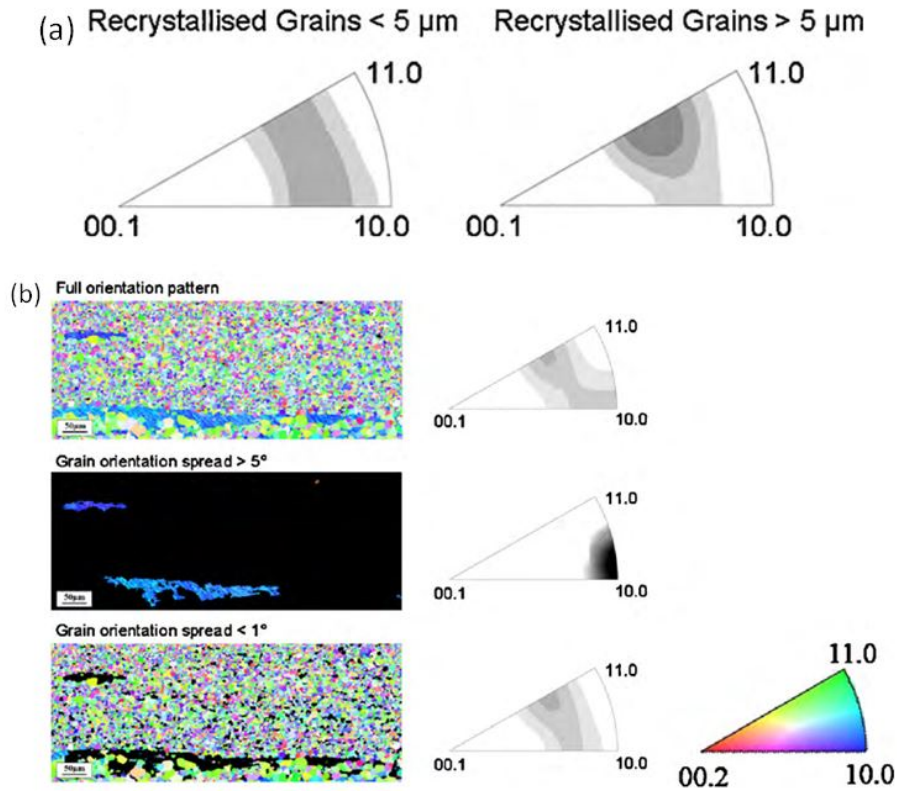
Figure 2.23   EBSD data for a Mg-0.95Mn-0.94Nd (wt. %).

Extruded at 573 K (300 ºC) with 30:1 extrusion ratio.a) IPF for small and large recrystallized grains, b) orientation map and inverse pole figure for deformed and recrystallized grains. Reproduced from [35] with permission from Elsevier.

2.6   Ternary and complex Mg-RE alloys

The reviewed RE elements have also been exploited in ternary and complex alloying systems in order to develop alloys with superior mechanical properties accompanied by texture weakening effects [145-155]. A high total concentration of RE elements was used in numerous chemical composition designs, which renders them cost-prohibitive for mass production purposes [149,156]. However, the scientific value of these studies must be taken into account so as to illuminate the ambiguities in this matter.

Hence, interaction of RE elements with one another and also with non-RE elements shall be investigated.

Addition of non-RE elements such as Zn and Zr alters the effectiveness of RE element addition in terms of their texture effects. In essence, formation of any type of precipitate or intermetallic in the Mg-matrix tends to decrease the RE element concentration in the matrix, thereby changing the threshold limits for the abovementioned RE elements. However, for RE element addition in the presence of Zn, it was observed that off-basal texture development in Mg matrix takes place close to the concentrations for that of binary alloys [157,14,158]. As a matter of fact, ternary systems of Mg-Zn-RE seem to have the propensity to form long-period stacking ordered (LPSO) phase [159-162]. Formation of this type of ordered phase in RE alloys would improve the mechanical properties, while its subsequent effects on texture evolutions depends on their size and shape. Jono *et al.* [80] reported that LPSO particles larger than 1 μm would enhance DRX through PSN mechanism, which may cause texture weakening. It was also reported that higher volume fraction of such particles may further weaken the fiber texture [163]. On the other hand, plate-like particles along with solute-segregated stacking faults sustain basal slip by suppressing slip modes with $\langle c \rangle$ component, and hence corroborate formation of sharp fiber texture in extruded alloys. Moreover, Garces *et al.* [164] reported that bimodal grain structure caused by LPSO phase elongated in the extrusion direction may enhance mechanical twinning in coarse grains. This may play a significant role in the texture evolutions during static recrystallization. On the other hand, formation of large LPSO particles (~20 μm) with high volume fraction (i.e. greater than 0.5) could potentially inhibit twin activation [165].

In addition to ternary alloys, numerous works have been performed on complex alloying systems, through which new facts about nucleation and growth of randomly oriented grains were obtained. Li [37] observed the nucleation of grains with random orientation inside deformation bands (DB) under uniaxial compression in a complex Mg-RE alloy (Mg−9Gd−4Y−0.6Zr wt. %). It was reported that DBs were initiated from the existing GBs and oriented growth of DRX grains inside DBs created the off-basal texture components. Additionally, it was observed that dynamic precipitation (i.e. strain induced precipitation) takes place during compressive deformation within DBs and retards DRX, which in turn suppresses texture weakening effects at higher Z values. Robson *et al.* [36] reported that extrusion of Mg-RE alloys (Mg-6Y-7Gd-0.5 Zr wt. %) below the solvus temperature of β precipitates, similar to the case of alloys with LPSO phase, yields a bimodal microstructure where the finer grains form within the bands of β precipitates. However, regardless of the extrusion condition, the final texture of the extrudates was weak, and only a slight difference in the developed texture components was captured. They attributed the appearance of new components such as $[0001]||ED$ to their growth preference, and the observed yield symmetry was believed to be tied with altered CRSS values driven by RE element addition in addition to texture randomization. In addition, the β ($Mg_5(Gd, Y)$) phase may potentially form on sub-boundaries, which, in turn, would suppress the CDRX mechanism (rotation of low angle GBs to high angle ones) [166]. This perhaps affects texture evolution during DRX.

In the case of compositions with alloying contents above their solubility limit, post treatments must be conducted in a way that randomizes texture without inducing

precipitates that are detrimental for total elongation. Liu *et al.* [156] reported that $\langle 10\bar{1}0 \rangle || ED$ fiber texture generated by extrusion almost disappeared after T4 and T6 heat treatments in a ternary Mg alloy (Mg-10Gd-3Y wt. %). T6 treatment improved mechanical properties while T4 deteriorated mechanical properties due to excessive grain growth. It was also reported that aging treatment improved tensile strength in the cost of formability lost [146]. Hence, an optimized sequence of treatments should be conducted on these alloys.

Addition of optimized amount of grain refiners and solid solution strengtheners such as Zr and Zn is beneficial when it comes to desired mechanical properties [147]. Sanjari *et al.*[167] reported that increasing Ce/Zn ratio in ternary Mg-Zn-Ce alloys at relatively higher concentrations of Ce (i.e. 1 wt. %) through changing Zn content results in higher GB mobility and larger grain size after thermo-mechanical processing. Generally speaking, the total concentration of added elements and their mutual ratio affects DRX kinetics since the diffusion coefficient of the alloying elements are mostly greater than the self-diffusion coefficient of Mg [168,169]. This implies that there is a balance compromising between texture modifications and mechanical properties. Intuitively, grain growth is essential for texture evolutions while it may turn out to be detrimental for creep properties.

2.7   Summary and Conclusions

It is quite remarkable that despite the numerous studies conducted to understand the effect of rare earth elements on dynamic recrystallization and the mechanisms by which they modify texture, concrete conclusions remain quite elusive. There is, however, a consensus on the effect of RE elements in promoting $\langle c + a \rangle$ and prismatic slip, which

is attributed to a decrease in the stacking fault energy on non-basal planes, and a mitigation of dislocation motion and ability to cross slip as solutes diffuse in dislocation cores. At the macroscopic level, most wrought Mg alloys with proper additions of RE elements exhibit improved ductility, reduced anisotropy, and thereby enhanced formability. These improvements in mechanical properties are generally attributed to texture weakening and the decreased CRSS gap between active slip modes. Enhancement of non-basal slip, however, causes little changes in the deformation texture, which remains dominated by the traditional "basal texture", manifesting itself as a $\langle 10\bar{1}0 \rangle || ED$ fiber after extrusion and a $[0001] || ND$ texture after rolling. This phenomenon rules out activation of new non-basal slip modes having a different Taylor axis than those known for classically operating modes. Understandably, RE elements could only affect the relative activity of traditional slip systems.

However, during dynamic recrystallization, RE elements result in a drastic attenuation in texture strength, as new orientations surface with an abundance unseen in traditional Mg alloys. The consensus of the available literature suggests that the genesis of these orientations is associated with a change in the dominant recrystallization mechanism. Figure 2.24 depicts a schematic representation of the influence of RE alloying strategies on recrystallization behavior from different aspects. The minute details of these multiple effects on texture evolution are briefly summarized in what follows. Under extrusion conditions, all RE elements produce a significant $\langle 11\bar{2}1 \rangle || ED$ component, known as the RE component. The origin of this texture is still a wide open question, as it is not yet clear whether the orientation selection process operates during nucleation or grain growth.

49
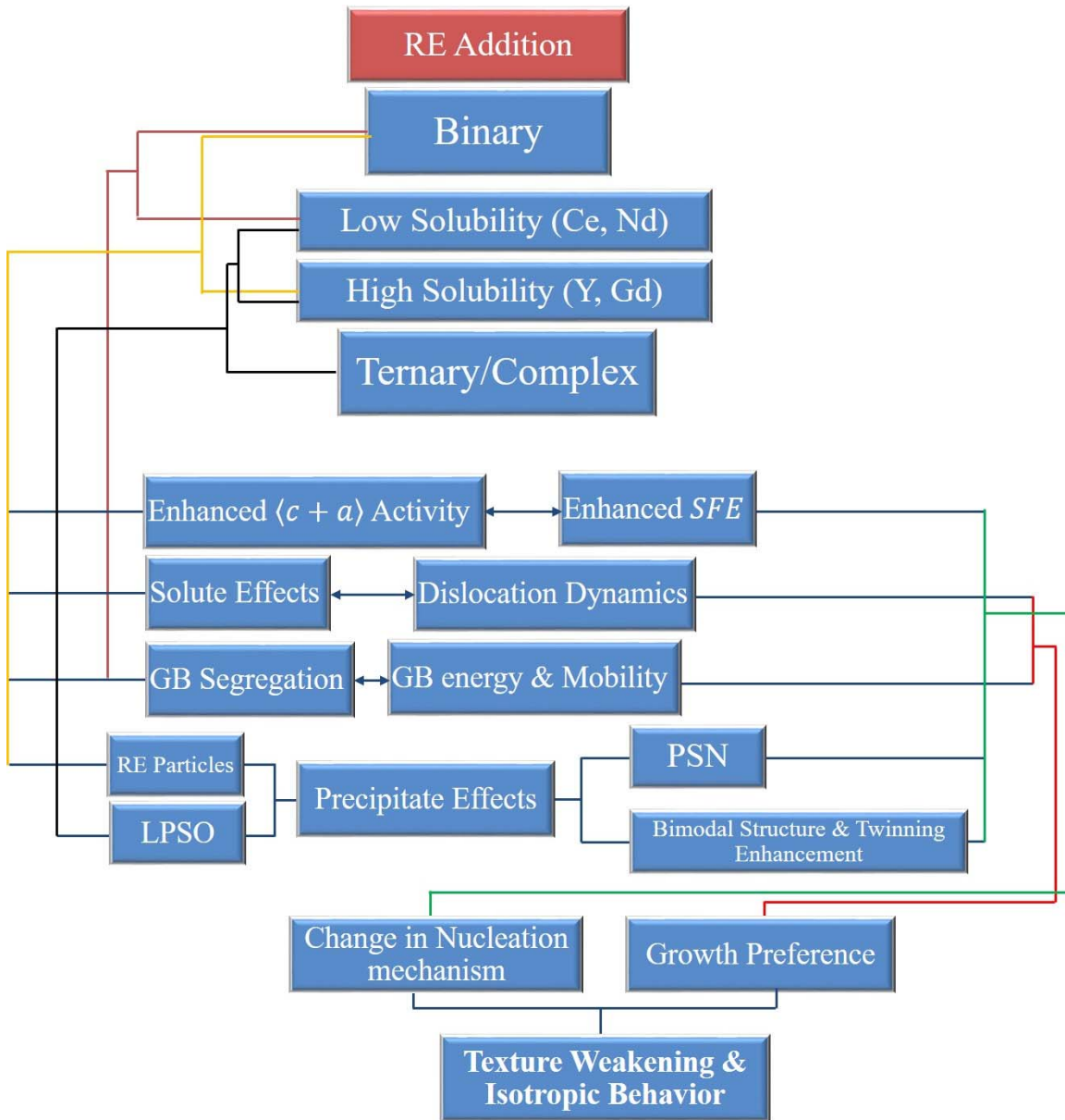
Figure 2.24 A schematic chart illustrating mechanisms believed to be responsible for the effect of rare-earth elements on texture weakening in Mg alloys.

We consider it unlikely for both recrystallization stages to single out this orientation, or any other specific orientation, since these stages have quite different driving forces. However, it is logical to assume that the grains associated with this

50

orientation originate at the $\langle 10\bar{1}0 \rangle || ED$ parent component following a discontinuous nucleation process at the available interfaces. Several endeavors indicate that the most important action of RE elements takes place at the boundaries where they have been observed to segregate. This effect permeates both high and low angle grain boundaries critically including prominent twin boundaries. As in conventional Mg alloys, the energy and mobility of the grain boundaries likely dictate the dominant misorientation relationships, and as such, the orientations of the new grains. Most recently, Zeng *et al.*[170,171] pointed out that dynamic recrystallization (DRX) grains with random orientation nucleated in the early stages of DRX tend to grow in ternary Mg-Zn-Ca alloy while they disappeared in binary Mg-Zn and Mg-Ca alloys. This phenomenon was attributed to the co-segregation of Zn and Ca atoms that inhibited growth of grains with basal texture. In other terms, low energy and low mobility of grains boundaries as a result of the co-segregation provides the chance for grains with random orientation to grow. A similar co-segregation behavior was observed for Mg-Zn-Gd alloys, which was discussed in section 4 [133]. Formation of these special boundaries may be also affected by the type of the substructure that develops during recovery. RE elements may in fact alter the limiting step of dislocation reactions during deformation, (cross-slip, jogs, super-jogs, dipoles, pinched off loops) allowing for all types of active dislocation to exist in the subgrain boundaries. This would set the stage for combined rotations around $\langle 10\bar{1}0 \rangle || ED$ and $\langle 11\bar{2}0 \rangle || ED$ to take place, giving rise to the observed RE texture fibers, i.e. $\langle 11\bar{2}1 \rangle || ED$. This effect warrants further endeavors to shed the light on the connection between the concentration and type of the RE element, and the grain boundary atomic structure, which can potentially govern the growth preference. It should be also noted that

segregation behavior of the alloying elements might vary with the type of grain boundary and the added element, giving rise to the promotion of certain orientations. This hypothesis is in good agreement with the intensities several types of RE elements were observed to spawn for the same RE texture component. All these concepts are still mostly unexplored themes of research, and warrant substantial future endeavors to reveal them.

Much work is still needed to further our understanding of all these effects in traditional Mg alloys as well as in RE element-containing Mg alloys. We stress the following fundamental gaps which should come under the magnifying glass of future endeavors:

1.   The question of how the nature of recrystallization changes in Mg-RE alloys is still pending. Further investigations are required to decipher the effect of RE element additions on the interplay of CDRX and DDRX, and the subsequent effects that result in formation of $\langle 11\bar{2}1 \rangle || ED$ RE-texture component.

2.   Here, the role of grain boundary energy and mobility in orientation selection is revealed as a sound hypothesis for the effect of RE element additions on recrystallization texture under extrusion. This possible effect it is still largely unexplored and warrants investigations of grain boundary character at the atomic scale.

3.   It must be recognized that RE elements interact differently depending on the composition and also the presence of other alloying constituents (e.g. non-RE elements or other RE elements), which makes it difficult to formulate generalizations without considering the above effects. Furthermore, interaction of RE elements with the Mg matrix changes from solute to precipitate type, with an intermediate dual nature (both as solute and second phase), and the nature of their impact might change drastically between the two. Addressing these issues would be eye-opening and could cast light on the critical topics in this field.

4. The role of twinning in damage of traditional Mg alloys is still uncharted and warrants serious endeavors to clear up the way for understanding the effects of RE elements, and probably other elements, on the enhancement of ductility. It is insufficient to just correlate ductility and anisotropy for understanding the effect of RE element additions on mitigating damage in traditional Mg alloys. More depth must be gained in both fronts for the exact interactions that lead to premature cracking. For instance, under tension normal to the $\langle c \rangle$-axis, tension twinning is prohibited, while strikingly, contraction twinning is almost absent for compression along the $\langle c \rangle$-axis. However, under both loading orientations an all-but brittle fracture is recorded. Therefore, twinning might not be the sole deformation mechanism responsible for fracture. A better hypothesis should take into consideration the extent of interactions between several distinct deformation modes. Do RE elements tend to mitigate these interactions by texture weakening or an action on deformation modes or even both?

2.8   References:

[1] B. Mordike, T. Ebert, Magnesium: properties—applications—potential, Mater. Sci. Eng. A 302 (2001) 37-45.

[2] J. Hirsch, T. Al-Samman, Superior light metals by texture engineering: Optimized aluminum and magnesium alloys for automotive applications, Acta Mater. 61 (2013) 818-843.

[3] C. Dharmendra, K.P. Rao, Y.V.R.K. Prasad, N. Hort, K.U. Kainer, Hot workability analysis with processing map and texture characteristics of as-cast TX32 magnesium alloy, J. Mater. Sci. 48 (2013) 5236-5246.

[4] L. Guo, F. Fujita, Effect of equivalent strain and redundant shear strain on microstructure and texture evolution during hot rolling in Mg–3Al–1Zn alloys, J. Mater. Sci. 47 (2012) 6213-6219.

[5] X. Huang, K. Suzuki, Y. Chino, M. Mabuchi, Influence of rolling temperature on static recrystallization behavior of AZ31 magnesium alloy, J. Mater. Sci. 47 (2012) 4561-4567.

[6] Y. Huang, R.B. Figueiredo, T. Baudin, A.-L. Helbert, F. Brisset, T.G. Langdon, Effect of temperature on the processing of a magnesium alloy by high-pressure torsion, J. Mater. Sci. 47 (2012) 7796-7806.

[7] K. Kubota, M. Mabuchi, K. Higashi, Review processing and mechanical properties of fine-grained magnesium alloys, J. Mater. Sci. 34 (1999) 2255-2262.

[8] M.R. Barnett, Twinning and the ductility of magnesium alloys, Mater. Sci. Eng. A 464 (2007) 8-16.

[9] M.R. Barnett, Twinning and the ductility of magnesium alloys, Mater. Sci. Eng. A 464 (2007) 1-7.

[10] J. Koike, T. Kobayashi, T. Mukai, H. Watanabe, M. Suzuki, K. Maruyama, K. Higashi, The activity of non-basal slip systems and dynamic recovery at room temperature in fine-grained AZ31B magnesium alloys, Acta Mater. 51 (2003) 2055-2065.

[11] E. Aghion, B. Bronfin, D. Eliezer, The role of the magnesium industry in protecting the environment, J. Mater. Process. Technol. 117 (2001) 381-385.

[12] M.K. Kulekci, Magnesium and its alloys applications in automotive industry, Int. J. Adv. Manuf. Technol. 39 (2007) 851-865.

[13] A. Yamashita, Z. Horita, T.G. Langdon, Improving the mechanical properties of magnesium and a magnesium alloy through severe plastic deformation, Mater. Sci. Eng. A 300 (2001) 142-147.

[14] H. Yan, R. Chen, N. Zheng, J. Luo, S. Kamado, E. Han, Effects of trace Gd concentration on texture and mechanical properties of hot-rolled Mg–2Zn–xGd sheets, J. Magnesium Alloys 1 (2013) 23-30.

[15] S. Yi, J. Bohlen, F. Heinemann, D. Letzig, Mechanical anisotropy and deep drawing behaviour of AZ31 and ZE10 magnesium alloy sheets, Acta Mater. 58 (2010) 592-605.

[16] Q. Huo, X. Yang, J. Ma, H. Sun, J. Wang, L. Zhang, Texture weakening of AZ31 magnesium alloy sheet obtained by a combination of bidirectional cyclic bending at low temperature and static recrystallization, J. Mater. Sci. 48 (2012) 913-919.

[17] M. Janeček, S. Yi, R. Král, J. Vrátná, K.U. Kainer, Texture and microstructure evolution in ultrafine-grained AZ31 processed by EX-ECAP, J. Mater. Sci. 45 (2010) 4665-4671.

[18] A.S.H. Kabir, M. Sanjari, J. Su, I.-H. Jung, S. Yue, Effect of annealing on microstructure and texture evolution of uniaxial hot compressed Mg–Al–Sn alloys, J. Mater. Sci. 51 (2015) 1600-1609.

[19] F. Kang, Z. Li, J.T. Wang, P. Cheng, H.Y. Wu, The activation of $\langle c + a \rangle$ non-basal slip in Magnesium alloys, J. Mater. Sci. 47 (2012) 7854-7859.

[20] M.-G. Lee, R. Wagoner, J. Lee, K. Chung, H. Kim, Constitutive modeling for anisotropic/asymmetric hardening behavior of magnesium alloy sheets, Int. J. Plast. 24 (2008) 545-582.

[21] H. Wang, B. Raeisinia, P. Wu, S. Agnew, C. Tomé, Evaluation of self-consistent polycrystal plasticity models for magnesium alloy AZ31B sheet, Int. J. Solids Struct. 47 (2010) 2905-2917.

[22] P. Pérez, G. Garcés, P. Adeva, Influence of texture on the mechanical properties of commercially pure magnesium prepared by powder metallurgy, J. Mater. Sci. 42 (2007) 3969-3976.

[23] S.-Q. Zhu, H.-G. Yan, W.-J. Xia, J.-Z. Liu, J.-F. Jiang, Influence of different deformation processing on the AZ31 magnesium alloy sheets, J. Mater. Sci. 44 (2009) 3800-3806.

[24] I. Ulacia, N.V. Dudamell, F. Gálvez, S. Yi, M.T. Pérez-Prado, I. Hurtado, Mechanical behavior and microstructural evolution of a Mg AZ31 sheet at dynamic strain rates, Acta Mater. 58 (2010) 2988-2998.

[25] X. Li, P. Yang, L.N. Wang, L. Meng, F. Cui, Orientational analysis of static recrystallization at compression twins in a magnesium alloy AZ31, Mater. Sci. Eng. A 517 (2009) 160-169.

[26] A. Jäger, P. Lukáč, V. Gärtnerová, J. Haloda, M. Dopita, Influence of annealing on the microstructure of commercial Mg alloy AZ31 after mechanical forming, Mater. Sci. Eng. A 432 (2006) 20-25.

[27] H. Li, E. Hsu, J. Szpunar, H. Utsunomiya, T. Sakai, Deformation mechanism and texture and microstructure evolution during high-speed rolling of AZ31B Mg sheets, J. Mater. Sci. 43 (2008) 7148-7156.

[28] M. Sanjari, A.S.H. Kabir, A. Farzadfar, H. Utsunomiya, R. Petrov, L. Kestens, S. Yue, Promotion of texture weakening in magnesium by alloying and thermomechanical processing. II: rolling speed, J. Mater. Sci. 49 (2013) 1426-1436.

[29] S. Wang, R. Ma, L. Yang, Y. Wang, Y. Wang, Precipitates effect on microstructure of as-deformed and as-annealed AZ41 magnesium alloys by adding Mn and Ca, J. Mater. Sci. 46 (2010) 3060-3065.

[30] B.J. Bonarski, E. Schafler, B. Mingler, W. Skrotzki, B. Mikulowski, M.J. Zehetbauer, Texture evolution of Mg during high-pressure torsion, J. Mater. Sci. 43 (2008) 7513-7518.

[31] H. Lin, J. Huang, T. Langdon, Relationship between texture and low temperature superplasticity in an extruded AZ31 Mg alloy processed by ECAP, Mater. Sci. Eng. A 402 (2005) 250-257.

[32] S.R. Agnew, Ö. Duygulu, Plastic anisotropy and the role of non-basal slip in magnesium alloy AZ31B, Int. J. Plast. 21 (2005) 1161-1193.

[33] M.R. Barnett, Quenched and annealed microstructures of hot worked magnesium AZ31, Mater. Trans. 44 (2003) 571-577.

[34] M. Perez-Prado, O. Ruano, Texture evolution during annealing of magnesium AZ31 alloy, Scripta Mater. 46 (2002) 149-155.

[35] J. Bohlen, S. Yi, D. Letzig, K.U. Kainer, Effect of rare earth elements on the microstructure and texture development in magnesium–manganese alloys during extrusion, Mater. Sci. Eng. A 527 (2010) 7092-7098.

[36] J.D. Robson, A.M. Twier, G.W. Lorimer, P. Rogers, Effect of extrusion conditions on microstructure, texture, and yield asymmetry in Mg–6Y–7Gd–0.5wt%Zr alloy, Mater. Sci. Eng. A 528 (2011) 7247-7256.

[37] L. Li, Deformation band and texture of a cast Mg–RE alloy under uniaxial hot compression, Mater. Sci. Eng. A 528 (2011) 7178-7185.

[38] S.A. Farzadfar, M. Sanjari, I.H. Jung, E. Essadiqi, S. Yue, Role of yttrium in the microstructure and texture evolution of Mg, Mater. Sci. Eng. A 528 (2011) 6742-6753.

[39] M. Yamasaki, K. Hashimoto, K. Hagihara, Y. Kawamura, Effect of multimodal microstructure evolution on mechanical properties of Mg–Zn–Y extruded alloy, Acta Mater. 59 (2011) 3646-3658.

[40] N. Stanford, M.R. Barnett, The origin of "rare earth" texture development in extruded Mg-based alloys and its effect on tensile ductility, Mater. Sci. Eng. A 496 (2008) 399-408.

[41] T. Al-Samman, X. Li, Sheet texture modification in magnesium-based alloys by selective rare earth alloying, Mater. Sci. Eng. A 528 (2011) 3809-3822.

[42] J. Bohlen, M.R. Nürnberg, J.W. Senn, D. Letzig, S.R. Agnew, The texture and anisotropy of magnesium–zinc–rare earth alloy sheets, Acta Mater. 55 (2007) 2101-2112.

[43] L. Mackenzie, M. Pekguleryuz, The recrystallization and texture of magnesium–zinc–cerium alloys, Scripta Mater. 59 (2008) 665-668.

[44] X. Lou, M. Li, R. Boger, S. Agnew, R. Wagoner, Hardening evolution of AZ31B Mg sheet, Int. J. Plast. 23 (2007) 44-86.

[45] T. Al-Samman, Modification of texture and microstructure of magnesium alloy extrusions by particle-stimulated recrystallization, Mater. Sci. Eng. A 560 (2013) 561-566.

[46] X. Li, T. Al-Samman, G. Gottstein, Mechanical properties and anisotropy of ME20 magnesium sheet produced by unidirectional and cross rolling, Mater. Des. 32 (2011) 4385-4393.

[47] X. Li, T. Al-Samman, S. Mu, G. Gottstein, Texture and microstructure development during hot deformation of ME20 magnesium alloy: Experiments and simulations, Mater. Sci. Eng. A 528 (2011) 7915-7925.

[48] X. Li, F. Jiao, T. Al-Samman, S.G. Chowdhury, Influence of second-phase precipitates on the texture evolution of Mg–Al–Zn alloys during hot deformation, Scripta Mater. 66 (2012) 159-162.

[49] H. Yan, S. Xu, R. Chen, S. Kamado, T. Honma, E. Han, Twins, shear bands and recrystallization of a Mg–2.0% Zn–0.8% Gd alloy during rolling, Scripta Mater. 64 (2011) 141-144.

[50] S. Sandlöbes, S. Zaefferer, I. Schestakow, S. Yi, R. Gonzalez-Martinez, On the role of non-basal deformation mechanisms for the ductility of Mg and Mg–Y alloys, Acta Mater. 59 (2011) 429-439.

[51] I. Basu, T. Al-Samman, Triggering rare earth texture modification in magnesium alloys by addition of zinc and zirconium, Acta Mater. 67 (2014) 116-133.

[52] C.D. Barrett, H. El Kadiri, The roles of grain boundary dislocations and disclinations in the nucleation of {10 2} twinning, Acta Mater. 63 (2014) 1-15.

[53] H. El Kadiri, J. Kapil, A. Oppedal, L. Hector, S.R. Agnew, M. Cherkaoui, S. Vogel, The effect of twin–twin interactions on the nucleation and propagation of twinning in magnesium, Acta Mater. 61 (2013) 3549-3563.

[54] E. Ball, P. Prangnell, Tensile-compressive yield asymmetries in high strength wrought magnesium alloys, Scripta Metallurgica et Materialia 31 (1994) 111-116.

[55] J.P. Hadorn, K. Hantzsche, S. Yi, J. Bohlen, D. Letzig, J.A. Wollmershauser, S.R. Agnew, Role of Solute in the Texture Modification During Hot Deformation of Mg-Rare Earth Alloys, Metall. Mater. Trans. A 43 (2011) 1347-1362.

[56] J.P. Hadorn, R.P. Mulay, K. Hantzsche, S. Yi, J. Bohlen, D. Letzig, S.R. Agnew, Texture Weakening Effects in Ce-Containing Mg Alloys, Metall. Mater. Trans. A 44 (2012) 1566-1576.

[57] N. Stanford, The effect of rare earth elements on the behaviour of magnesium-based alloys: Part 2–recrystallisation and texture development, Mater. Sci. Eng. A 565 (2013) 469-475.

[58] R. Cottam, J. Robson, G. Lorimer, B. Davis, Dynamic recrystallization of Mg and Mg–Y alloys: Crystallographic texture development, Mater. Sci. Eng. A 485 (2008) 375-382.

[59] I. Basu, K. Pradeep, C. Mießen, L. Barrales-Mora, T. Al-Samman, The role of atomic scale segregation in designing highly ductile magnesium alloys, Acta Mater. 116 (2016) 77-94.

[60] S. Agnew, M. Yoo, C. Tome, Application of texture simulation to understanding mechanical behavior of Mg and solid solution alloys containing Li or Y, Acta Mater. 49 (2001) 4277-4289.

[61] T. Lin, Physical theory of plasticity, Advances in applied mechanics 11 (1971) 255-311.

[62] H. El Kadiri, A. Oppedal, A crystal plasticity theory for latent hardening by glide twinning through dislocation transmutation and twin accommodation effects, J. Mech. Phys. Solids 58 (2010) 613-624.

[63] Q. Ma, H. El Kadiri, A. Oppedal, J. Baird, M. Horstemeyer, M. Cherkaoui, Twinning and double twinning upon compression of prismatic textures in an AM30 magnesium alloy, Scripta Mater. 64 (2011) 813-816.

[64] Q. Ma, H. El Kadiri, A. Oppedal, J. Baird, B. Li, M. Horstemeyer, S. Vogel, Twinning effects in a rod-textured AM30 Magnesium alloy, Int. J. Plast. 29 (2012) 60-76.

[65] A. Oppedal, H. El Kadiri, C. Tomé, G. Kaschner, S.C. Vogel, J. Baird, M. Horstemeyer, Effect of dislocation transmutation on modeling hardening mechanisms by twinning in magnesium, Int. J. Plast. 30 (2012) 41-61.

[66] Z. Wu, W. Curtin, The origins of high hardening and low ductility in magnesium, Nature 526 (2015) 62-67.

[67] A. Luque, M. Ghazisaeidi, W.A. Curtin, Deformation modes in magnesium (0 0 0 1) and (0111) single crystals: simulations versus experiments, Modell. Simul. Mater. Sci. Eng. 21 (2013) 045010.

[68] A. Jain, S. Agnew, Modeling the temperature dependent effect of twinning on the behavior of magnesium alloy AZ31B sheet, Mater. Sci. Eng. A 462 (2007) 29-36.

[69] Y.V.R.K. Prasad, K.P. Rao, Effect of crystallographic texture on the kinetics of hot deformation of rolled Mg–3Al–1Zn alloy plate, Mater. Sci. Eng. A 432 (2006) 170-177.

[70] A. Chapuis, J.H. Driver, Temperature dependency of slip and twinning in plane strain compressed magnesium single crystals, Acta Mater. 59 (2011) 1986-1994.

[71] S. Kleiner, P. Uggowitzer, Mechanical anisotropy of extruded Mg–6% Al–1% Zn alloy, Mater. Sci. Eng. A 379 (2004) 258-263.

[72] J. Del Valle, M.T. Pérez-Prado, O. Ruano, Texture evolution during large-strain hot rolling of the Mg AZ61 alloy, Mater. Sci. Eng. A 355 (2003) 68-78.

[73] Q. Jin, S.-Y. Shim, S.-G. Lim, Correlation of microstructural evolution and formation of basal texture in a coarse grained Mg–Al alloy during hot rolling, Scripta Mater. 55 (2006) 843-846.

[74] S.-H. Kim, B.-S. You, C.D. Yim, Y.-M. Seo, Texture and microstructure changes in asymmetrically hot rolled AZ31 magnesium alloy sheets, Mater. Lett. 59 (2005) 3876-3880.

[75] M. Mabuchi, Y. Chino, H. Iwasaki, T. Aizawa, K. Higashi, The grain size and texture dependence of tensile properties in extruded Mg-9Al-1Zn, Mater. Trans. 42 (2001) 1182-1188.

[76] Y. Wang, J. Huang, The role of twinning and untwinning in yielding behavior in hot-extruded Mg–Al–Zn alloy, Acta Mater. 55 (2007) 897-905.

[77] D. Xu, L. Liu, Y. Xu, E. Han, Effect of microstructure and texture on the mechanical properties of the as-extruded Mg–Zn–Y–Zr alloys, Mater. Sci. Eng. A 443 (2007) 248-256.

[78] R. Gehrmann, M.M. Frommert, G. Gottstein, Texture effects on plastic deformation of magnesium, Mater. Sci. Eng. A 395 (2005) 338-349.

[79] P. Yang, Y. Yu, L. Chen, W. Mao, Experimental determination and theoretical prediction of twin orientations in magnesium alloy AZ31, Scripta Mater. 50 (2004) 1163-1168.

[80] Y. Jono, M. Yamasaki, Y. Kawamura, Effect of LPSO Phase-Stimulated Texture Evolution on Creep Resistance of Extruded Mg^|^ndash;Zn^|^ndash;Gd Alloys, Mater. Trans. 54 (2013) 703-712.

[81] A. Galiyev, R. Kaibyshev, G. Gottstein, Correlation of plastic deformation and dynamic recrystallization in magnesium alloy ZK60, Acta Mater. 49 (2001) 1199-1207.

[82] S.M. Fatemi-Varzaneh, A. Zarei-Hanzaki, H. Beladi, Dynamic recrystallization in AZ31 magnesium alloy, Mater. Sci. Eng. A 456 (2007) 52-57.

[83] O. Sitdikov, R. Kaibyshev, Dynamic Recrystallization in Pure Magnesium, Mater. Trans. 42 (2001) 1928-1937.

[84] A. Rollett, F. Humphreys, G.S. Rohrer, M. Hatherly. Recrystallization and related annealing phenomena, Elsevier, 2004.

[85] M. Barnett, A Taylor model based description of the proof stress of magnesium AZ31 during hot working, Metall. Mater. Trans. A 34 (2003) 1799-1806.

[86] I. Basu, T. Al-Samman, Twin recrystallization mechanisms in magnesium-rare earth alloys, Acta Mater. 96 (2015) 111-132.

[87] T. Al-Samman, K.D. Molodov, D.A. Molodov, G. Gottstein, S. Suwas, Softening and dynamic recrystallization in magnesium single crystals during c-axis compression, Acta Mater. 60 (2012) 537-545.

[88] K.D. Molodov, T. Al-Samman, D.A. Molodov, G. Gottstein, Mechanisms of exceptional ductility of magnesium single crystal during deformation at room temperature: Multiple twinning and dynamic recrystallization, Acta Mater. 76 (2014) 314-330.

[89] P. Changizian, A. Zarei-Hanzaki, H.R. Abedi, On the recrystallization behavior of homogenized AZ81 magnesium alloy: The effect of mechanical twins and γ precipitates, Mater. Sci. Eng. A 558 (2012) 44-51.

[90] S. Ion, F. Humphreys, S. White, Dynamic recrystallisation and the development of microstructure during the high temperature deformation of magnesium, Acta Metall. 30 (1982) 1909-1919.

[91] É. Martin, J.J. Jonas, Evolution of microstructure and microtexture during the hot deformation of Mg–3% Al, Acta Mater. 58 (2010) 4253-4266.

[92] Z. Sheng, R. Shivpuri, Modeling flow stress of magnesium alloys at elevated temperature, Mater. Sci. Eng. A 419 (2006) 202-208.

[93] J. Del Valle, M.T. Pérez-Prado, O.A. Ruano, Deformation mechanisms responsible for the high ductility in a Mg AZ31 alloy analyzed by electron backscattered diffraction, Metall. Mater. Trans. A 36 (2005) 1427-1438.

[94] J. Del Valle, O.A. Ruano, Influence of texture on dynamic recrystallization and deformation mechanisms in rolled or ECAPed AZ31 magnesium alloy, Mater. Sci. Eng. A 487 (2008) 473-480.

[95] T. Al-Samman, G. Gottstein, Dynamic recrystallization during high temperature deformation of magnesium, Mater. Sci. Eng. A 490 (2008) 411-420.

[96] S.B. Yi, S. Zaefferer, H.G. Brokmeier, Mechanical behaviour and microstructural evolution of magnesium alloy AZ31 in tension at different temperatures, Mater. Sci. Eng. A 424 (2006) 275-281.

[97] Y. Chino, M. Kado, M. Mabuchi, Enhancement of tensile ductility and stretch formability of magnesium by addition of 0.2wt%(0.035at%)Ce, Mater. Sci. Eng. A 494 (2008) 343-349.

[98] M. Barnett, M. Nave, C. Bettles, Deformation microstructures and textures of some cold rolled Mg alloys, Mater. Sci. Eng. A 386 (2004) 205-211.

[99] P. Dobroň, F. Chmelík, S. Yi, K. Parfenenko, D. Letzig, J. Bohlen, Grain size effects on deformation twinning in an extruded magnesium alloy tested in compression, Scripta Mater. 65 (2011) 424-427.

[100] G.G. Yapici, I. Karaman, Common trends in texture evolution of ultra-fine-grained hcp materials during equal channel angular extrusion, Mater. Sci. Eng. A 503 (2009) 78-81.

[101] K. Hantzsche, J. Bohlen, J. Wendt, K.U. Kainer, S.B. Yi, D. Letzig, Effect of rare earth additions on microstructure and texture development of magnesium alloy sheets, Scripta Mater. 63 (2010) 725-730.

[102] N. Stanford, Micro-alloying Mg with Y, Ce, Gd and La for texture modification—A comparative study, Mater. Sci. Eng. A 527 (2010) 2669-2677.

[103] J.P. Hadorn, K. Hantzsche, S. Yi, J. Bohlen, D. Letzig, S.R. Agnew, Effects of Solute and Second-Phase Particles on the Texture of Nd-Containing Mg Alloys, Metall. Mater. Trans. A 43 (2012) 1363-1375.

[104] I. Moreno, T. Nandy, J. Jones, J. Allison, T. Pollock, Microstructural characterization of a die-cast magnesium-rare earth alloy, Scripta Mater. 45 (2001) 1423-1429.

[105] P. Hidalgo-Manrique, S.B. Yi, J. Bohlen, D. Letzig, M.T. Pérez-Prado, Effect of Nd Additions on Extrusion Texture Development and on Slip Activity in a Mg-Mn Alloy, Metall. Mater. Trans. A 44 (2013) 4819-4829.

[106] N. Stanford, G. Sha, J. Xia, S. Ringer, M. Barnett, Solute segregation and texture modification in an extruded magnesium alloy containing gadolinium, Scripta Mater. 65 (2011) 919-921.

[107] N. Stanford, D. Atwell, M.R. Barnett, The effect of Gd on the recrystallisation, texture and deformation behaviour of magnesium-based alloys, Acta Mater. 58 (2010) 6773-6783.

[108] N. Stanford, D. Atwell, A. Beer, C. Davies, M.R. Barnett, Effect of microalloying with rare-earth elements on the texture of extruded magnesium-based alloys, Scripta Mater. 59 (2008) 772-775.

[109] M.M. Avedesian, H. Baker, ASM specialty handbook: magnesium and magnesium alloys, ASM International, Materials Park, OH (1999) 15.

[110] S.R. Agnew, L. Capolungo, C.A. Calhoun, Connections between the basal I1 "growth" fault and ⟨c+a⟩ dislocations, Acta Mater. 82 (2015) 255-265.

[111] S. Sandlöbes, M. Friák, S. Zaefferer, A. Dick, S. Yi, D. Letzig, Z. Pei, L.F. Zhu, J. Neugebauer, D. Raabe, The relation between ductility and stacking fault energies in Mg and Mg–Y alloys, Acta Mater. 60 (2012) 3011-3021.

[112] M. Muzyk, Z. Pakiela, K. Kurzydlowski, Generalized stacking fault energy in magnesium alloys: density functional theory calculations, Scripta Mater. 66 (2012) 219-222.

[113] I.-H. Jung, M. Sanjari, J. Kim, S. Yue, Role of RE in the deformation and recrystallization of Mg alloy and a new alloy design concept for Mg–RE alloys, Scripta Mater. 102 (2015) 1-6.

[114] L.L. Rokhlin. Magnesium alloys containing rare earth metals: structure and properties, Crc Press, 2003.

[115] D.W. Zhou, P. Peng, J.S. Liu, Electronic structure and stability of Mg–Ce intermetallic compounds from first-principles calculations, J. Alloys Compd. 428 (2007) 316-321.

[116] Y.-B. Kang, A.D. Pelton, P. Chartrand, P. Spencer, C.D. Fuerst, Critical Evaluation and Thermodynamic Optimization of the Binary Systems in the Mg-Ce-Mn-Y System, J. Phase Equilib. Diffus. 28 (2007) 342-354.

[117] Y. Chino, M. Kado, M. Mabuchi, Compressive deformation behavior at room temperature – 773K in Mg–0.2mass%(0.035at.%)Ce alloy, Acta Mater. 56 (2008) 387-394.

[118] I. Basu, T. Al-Samman, G. Gottstein, Shear band-related recrystallization and grain growth in two rolled magnesium-rare earth alloys, Mater. Sci. Eng. A 579 (2013) 50-56.

[119] M. Masoumi, M. Hoseini, M. Pekguleryuz, The influence of Ce on the microstructure and rolling texture of Mg–1%Mn alloy, Mater. Sci. Eng. A 528 (2011) 3122-3129.

[120] R.K. Mishra, A.K. Gupta, P.R. Rao, A.K. Sachdev, A.M. Kumar, A.A. Luo, Influence of cerium on the texture and ductility of magnesium extrusions, Scripta Mater. 59 (2008) 562-565.

[121] M.R. Barnett, M.D. Nave, C.J. Bettles, Deformation microstructures and textures of some cold rolled Mg alloys, Mater. Sci. Eng. A 386 (2004) 205-211.

[122] G. Omori, S. Matsuo, H. Asada, Precipitation Process in a Mg–Ce Alloy, T JPN I MET 16 (1975) 247-255.

[123] Q. Peng, X. Hou, L. Wang, Y. Wu, Z. Cao, L. Wang, Microstructure and mechanical properties of high performance Mg–Gd based alloys, Mater. Des. 30 (2009) 292-296.

[124] Q.M. Peng, Y.M. Wu, D.Q. Fang, J. Meng, L.M. Wang, Microstructures and properties of Mg–7Gd alloy containing Y, J. Alloys Compd. 430 (2007) 252-256.

[125] M. Yamasaki, T. Anan, S. Yoshimoto, Y. Kawamura, Mechanical properties of warm-extruded Mg–Zn–Gd alloy with coherent 14H long periodic stacking ordered structure precipitate, Scripta Mater. 53 (2005) 799-803.

[126] M. Yamasaki, M. Sasaki, M. Nishijima, K. Hiraga, Y. Kawamura, Formation of 14H long period stacking ordered structure and profuse stacking faults in Mg–Zn–Gd alloys during isothermal aging at high temperature, Acta Mater. 55 (2007) 6798-6805.

[127] J. Zhang, Z. Leng, S. Liu, J. Li, M. Zhang, R. Wu, Microstructure and mechanical properties of Mg–Gd–Dy–Zn alloy with long period stacking ordered structure or stacking faults, J. Alloys Compd. 509 (2011) 7717-7722.

[128] D. Wu, R.S. Chen, E.H. Han, Excellent room-temperature ductility and formability of rolled Mg–Gd–Zn alloy sheets, J. Alloys Compd. 509 (2011) 2856-2863.

[129] L. Gao, R.S. Chen, E.H. Han, Effects of rare-earth elements Gd and Y on the solid solution strengthening of Mg alloys, J. Alloys Compd. 481 (2009) 379-384.

[130] X. Gao, S.M. He, X.Q. Zeng, L.M. Peng, W.J. Ding, J.F. Nie, Microstructure evolution in a Mg–15Gd–0.5Zr (wt.%) alloy during isothermal aging at 250°C, Mater. Sci. Eng. A 431 (2006) 322-327.

[131] X. Gao, J.F. Nie, Enhanced precipitation-hardening in Mg–Gd alloys containing Ag and Zn, Scripta Mater. 58 (2008) 619-622.

[132] J.F. Nie, K. Oh-ishi, X. Gao, K. Hono, Solute segregation and precipitation in a creep-resistant Mg–Gd–Zn alloy, Acta Mater. 56 (2008) 6061-6076.

[133] J. Nie, Y. Zhu, J. Liu, X.-Y. Fang, Periodic segregation of solute atoms in fully coherent twin boundaries, Science 340 (2013) 957-960.

[134] B. Lv, J. Peng, Y. Peng, A. Tang, The effect of addition of Nd and Ce on the microstructure and mechanical properties of ZM21 Mg alloy, J. Magnesium Alloys 1 (2013) 94-100.

[135] L. Ma, R.K. Mishra, L. Peng, A.A. Luo, W. Ding, A.K. Sachdev, Texture and mechanical behavior evolution of age-hardenable Mg–Nd–Zn extrusions during aging treatment, Mater. Sci. Eng. A 529 (2011) 151-155.

[136] Z.L. Ning, H. Wang, H.H. Liu, F.Y. Cao, S.T. Wang, J.F. Sun, Effects of Nd on microstructures and properties at the elevated temperature of a Mg–0.3Zn–0.32Zr alloy, Mater. Des. 31 (2010) 4438-4444.

[137] S. Gorsse, C.R. Hutchinson, B. Chevalier, J.F. Nie, A thermodynamic assessment of the Mg–Nd binary system using random solution and associate models for the liquid phase, J. Alloys Compd. 392 (2005) 253-262.

[138] J.P. Hadorn, S.R. Agnew, A new metastable phase in dilute, hot-rolled Mg–Nd alloys, Mater. Sci. Eng. A 533 (2012) 9-16.

[139] J. Wang, I.J. Beyerlein, Atomic Structures of $[0\bar{1}10]$ Symmetric Tilt Grain Boundaries in Hexagonal Close-Packed (hcp) Crystals, Metall. Mater. Trans. A 43 (2012) 3556-3569.

[140] J. Wang, I.J. Beyerlein, Atomic structures of symmetric tilt grain boundaries in hexagonal close packed (hcp) crystals, Modell. Simul. Mater. Sci. Eng. 20 (2012) 024002.

[141] V. Herrera-Solaz, P. Hidalgo-Manrique, M.T. Pérez-Prado, D. Letzig, J. Llorca, J. Segurado, Effect of rare earth additions on the critical resolved shear stresses of magnesium alloys, Mater. Lett. 128 (2014) 199-203.

[142] R. Sánchez-Martín, M.T. Pérez-Prado, J. Segurado, J. Bohlen, I. Gutiérrez-Urrutia, J. Llorca, J.M. Molina-Aldareguia, Measuring the critical resolved shear stresses in Mg alloys by instrumented nanoindentation, Acta Mater. 71 (2014) 283-292.

[143] N.V. Dudamell, P. Hidalgo-Manrique, A. Chakkedath, Z. Chen, C.J. Boehlert, F. Gálvez, S. Yi, J. Bohlen, D. Letzig, M.T. Pérez-Prado, Influence of strain rate on the twin and slip activity of a magnesium alloy containing neodymium, Mater. Sci. Eng. A 583 (2013) 220-231.

[144] V. Gärtnerová, Z. Trojanová, A. Jäger, P. Palček, Deformation behaviour of Mg–0.7 wt.% Nd alloy, J. Alloys Compd. 378 (2004) 180-183.

[145] Y.Z. Du, X.G. Qiao, M.Y. Zheng, K. Wu, S.W. Xu, The microstructure, texture and mechanical properties of extruded Mg–5.3Zn–0.2Ca–0.5Ce (wt%) alloy, Mater. Sci. Eng. A 620 (2015) 164-171.

[146] T. Homma, N. Kunito, S. Kamado, Fabrication of extraordinary high-strength magnesium alloy by hot extrusion, Scripta Mater. 61 (2009) 644-647.

[147] Q. Peng, Y. Huang, K.U. Kainer, N. Hort, High ductile as-cast Mg–RE based alloys at room temperature, Mater. Lett. 83 (2012) 209-212.

[148] D. Wu, R.S. Chen, W.N. Tang, E.H. Han, Influence of texture and grain size on the room-temperature ductility and tensile behavior in a Mg–Gd–Zn alloy processed by rolling and forging, Mater. Des. 41 (2012) 306-313.

[149] X. Hou, Z. Cao, L. Zhao, L. Wang, Y. Wu, L. Wang, Microstructure, texture and mechanical properties of a hot rolled Mg–6.5Gd–1.3Nd–0.7Y–0.3Zn alloy, Mater. Des. 34 (2012) 776-781.

[150] J. Fan, G. Yang, S. Chen, H. Xie, M. Wang, Y. Zhou, Effect of rare earths (Y, Ce) additions on the ignition points of magnesium alloys, J. Mater. Sci. 39 (2004) 6375-6377.

[151] G. Garcés, G. Requena, D. Tolnai, P. Pérez, P. Adeva, A. Stark, N. Schell, Influence of rare-earth addition on the long-period stacking ordered phase in cast Mg–Y–Zn alloys, J. Mater. Sci. 49 (2014) 2714-2722.

[152] M. Lentz, S. Gall, F. Schmack, H. Mayer, W. Reimers, Hot working behavior of a WE54 magnesium alloy, J. Mater. Sci. 49 (2014) 1121-1129.

[153] L. Wei, G. Dunlop, H. Westengen, Age hardening and precipitation in a cast magnesium-rare-earth alloy, J. Mater. Sci. 31 (1996) 387-397.

[154] D. Weiss, A. Kaya, E. Aghion, D. Eliezer, Microstructure and creep properties of a cast Mg-1.7% wt rare earth-0.3% wt Mn alloy, J. Mater. Sci. 37 (2002) 5371-5379.

[155] P. Changizian, A. Zarei-Hanzaki, M. Ghambari, A. Imandoust, Flow localization during severe plastic deformation of AZ81 magnesium alloy: Micro-shear banding phenomenon, Mater. Sci. Eng. A 582 (2013) 8-14.

[156] W.C. Liu, J. Dong, X. Song, J.P. Belnoue, F. Hofmann, W.J. Ding, A.M. Korsunsky, Effect of microstructures and texture development on tensile properties of Mg–10Gd–3Y alloy, Mater. Sci. Eng. A 528 (2011) 2250-2258.

[157] Y. Chino, K. Sassa, M. Mabuchi, Texture and stretch formability of Mg-1.5 mass% Zn-0.2 mass% Ce alloy rolled at different rolling temperatures, Mater. Trans. 49 (2008) 2916-2918.

[158] Y. Chino, K. Sassa, M. Mabuchi, Texture and stretch formability of a rolled Mg–Zn alloy containing dilute content of Y, Mater. Sci. Eng. A 513-514 (2009) 394-400.

[159] K. Hagihara, A. Kinoshita, Y. Sugino, M. Yamasaki, Y. Kawamura, H.Y. Yasuda, Y. Umakoshi, Effect of long-period stacking ordered phase on mechanical properties of Mg97Zn1Y2 extruded alloy, Acta Mater. 58 (2010) 6282-6293.

[160] Y. Kawamura, M. Yamasaki, Formation and Mechanical Properties of Mg97Zn1RE2 Alloys with Long-Period Stacking Ordered Structure, Mater. Trans. 48 (2007) 2986-2992.

[161] M. Matsuda, S. Ii, Y. Kawamura, Y. Ikuhara, M. Nishida, Variation of long-period stacking order structures in rapidly solidified Mg97Zn1Y2 alloy, Mater. Sci. Eng. A 393 (2005) 269-274.

[162] X.H. Shao, Z.Q. Yang, X.L. Ma, Strengthening and toughening mechanisms in Mg–Zn–Y alloy with a long period stacking ordered structure, Acta Mater. 58 (2010) 4760-4771.

[163] L.B. Tong, X.H. Li, H.J. Zhang, Effect of long period stacking ordered phase on the microstructure, texture and mechanical properties of extruded Mg–Y–Zn alloy, Mater. Sci. Eng. A 563 (2013) 177-183.

[164] G. Garces, D.G. Morris, M.A. Muñoz-Morris, P. Perez, D. Tolnai, C. Mendis, A. Stark, H.K. Lim, S. Kim, N. Shell, P. Adeva, Plasticity analysis by synchrotron radiation in a Mg97Y2Zn1 alloy with bimodal grain structure and containing LPSO phase, Acta Mater. 94 (2015) 78-86.

[165] L.B. Tong, X. Li, D.P. Zhang, L.R. Cheng, J. Meng, H.J. Zhang, Dynamic recrystallization and texture evolution of Mg–Y–Zn alloy during hot extrusion process, Mater. Charact. 92 (2014) 77-83.

[166] L. Li, Micro structure and texture evolution during super plastic deformation of Mg–Re extruded alloy, J. Alloys Compd. 555 (2013) 255-262.

[167] M. Sanjari, A. Farzadfar, A.S.H. Kabir, H. Utsunomiya, I.-H. Jung, R. Petrov, L. Kestens, S. Yue, Promotion of texture weakening in magnesium by alloying and thermomechanical processing: (I) alloying, J. Mater. Sci. 49 (2013) 1408-1425.

[168] S. Ganeshan, L. Hector, Z.-K. Liu, First-principles study of self-diffusion in hcp Mg and Zn, Computational Materials Science 50 (2010) 301-307.

[169] S. Ganeshan, L. Hector, Z.-K. Liu, First-principles calculations of impurity diffusion coefficients in dilute Mg alloys using the 8-frequency model, Acta Mater. 59 (2011) 3214-3228.

[170] Z.R. Zeng, M.Z. Bian, S.W. Xu, C.H.J. Davies, N. Birbilis, J.F. Nie, Texture evolution during cold rolling of dilute Mg alloys, Scripta Mater. 108 (2015) 6-10.

[171] Z.R. Zeng, Y.M. Zhu, S.W. Xu, M.Z. Bian, C.H.J. Davies, N. Birbilis, J.F. Nie, Texture evolution during static recrystallization of cold-rolled magnesium alloys, Acta Mater. 105 (2016) 479-494.

CHAPTER III

RECRYSTALLIZATION MECHANISMS GOVERNING TEXTURE EVOLUTION IN

COMPLEX RARE EARTH CONTAINING MAGNESIUM ALLOYS

3.1   Introduction

The propensity for magnesium (Mg) to develop sharp textures during

thermomechanical processing has plagued its future as an ideal lightweight material in

the automotive, aerospace, and defense applications. In a similar manner to single

crystals, sharp textures respond to mechanical loads with strong anisotropy and

asymmetry [1, 2]. This can be problematic in application. For example, a typical rolled

sheet cannot withstand large strains along arbitrary directions prior to fracture, a severe

problem for forming of Mg alloys. Moreover, a thin-walled hollow tubes made from Mg

alloys are observed to shatter into pieces prior to absorbing impact under crash conditions

[3-10].

The ease of basal slip and the dislocation recovery mechanisms operating in Mg

alloys have been long understood to promote sharp textures. Basal slip causes the basal

poles to align themselves with the loading direction [1,2], whereas dynamic recovery

confines these planes to rotate, only around the $\langle c \rangle$-axis within subgrains formed by

prismatic dislocations, and the prismatic axes within subgrains constructed by basal and

pyramidal dislocations [11, 12]. Those types of rotations occur because [0001] is the

Taylor axis for prismatic slip, while $\langle 10\bar{1}0 \rangle$ is the common one to both basal and

pyramidal $\langle c + a \rangle$ slips [11, 13-15]. Weak textures could have well developed if rotations could have been effected around an axis that deviates the $\langle c \rangle$-axis from the main loading direction. However, there is no active slip mode with such a desirable Taylor axis.

Dynamic recrystallization (DRX) has been observed to occur either continuously (CDRX) or discontinuously (DDRX) depending on the temperature, strain, and strain rate. These external factors directly affect dislocation generation and multiplication at mantle regions, while microstructure and defects such as grain boundaries (GBs), solutes, and particles could either promote or limit the driving force underscored in dislocation recovery [16-22]. Regardless of the predominant DRX mechanism in the processing condition, the sharp deformation texture would be either untouched or further sharpened in traditional Mg alloys [23]. The most successful approach to overcome this shortage has recently been alloying with rare earth elements (REE) including cerium (Ce), gadolinium (Gd), neodymium (Nd), lanthanum (La), and yttrium (Y) all caused noticeable texture modifications, resulting in a reduction in the strength of the basal texture [15, 24-26].

Not limited to texture weakening, REE additions were suggested to boost ductility by virtue of softening pyramidal $\langle c + a \rangle$ slip. Sandlöbes *et al.* [27, 28] reported that additions of Y could bolster $\langle c + a \rangle$ dislocation activity because Y decreases the energy of the I_1 stacking fault (ISF_1), which acts as a nucleation site for $\langle c + a \rangle$ dislocations [29, 30]. Ce and Nd additions were observed to cause similar non-basal slip enhancement by activating pyramidal $\langle a \rangle$ slip and by decreasing the critical resolved shear stress CRSS ratios between various active slip modes [15, 31, 32]. Despite the ductility improvements associated with REEs in Mg, the required temperatures for acceptable formability of

inner door panels still remain above 150 °C temperature, and one reason for this appears to be the fact that the texture after processing (although modified) is still sharp [24, 33].

These limitations have provoked interest in the mechanisms through which REEs modify textures, motivating research that will lead to identifying a rational design strategy that can harness the beneficial effects of REE to reach the required properties and performance of these alloys. Hantzsche *et al.* [34] and several other authors such as Hadorn *et al.* [15] showed that a compositional threshold exists for each REE whereupon texture intensity drops drastically. Several researchers reported that the essential texture weakening takes place upon DRX [24-26, 34, 35]. Bohlen *et al.* [24] confirmed that a recrystallized portion of the microstructure under extrusion has always a $\langle 11\bar{2}1 \rangle || ED$ (Extrusion Direction) component, characteristic of REEs, and hence referred to as "RE texture" [25, 26]. A $\langle 10\bar{1}1 \rangle || ED$ fiber with lower intensity was also reported to emerge with the RE texture. Furthermore, the RE texture is able to survive subsequent grain growth, which correlates with further texture randomization phenomena [24, 26, 34]. The origin of the RE texture is a metallurgical conundrum, added atop of the mechanisms underlying the effect of REEs on texture weakening.

Research experience with the legacy of cubic materials triggered a few authors to propose the so-called particle stimulated nucleation (PSN) as responsible for the rise of new orientations which do not occur in classical Mg alloys [36, 37], thereby, advocating for discontinues dynamic recrystallization (DDRX). However, Al-Samman *et al.* [38] showed that RE-texture and texture weakening can occur, even in cases where the fraction of RE-containing precipitates remains too dismal to bring about a macroscopic effect. Robson *et al.* [39] confirmed that grains that recrystallized close to grain

boundaries (GBs) attained larger sizes and survived longer than those recrystallized by a PSN effect.

As the PSN mechanism began to prove less than ideal, a few authors such as Hadorn *et al*. [40] suggested that REEs in solid solution could actually alter the deformation mechanisms in a way that disrupts how geometrically necessary dislocation (GND) structures develop in the material. On a related note, Stanford [25] indicated that RE effect greatly depends upon the way solute atoms interact with both dislocations and GBs. A GB with segregated RE solutes becomes sluggish, [40-43], and hence, more resistant to migration and/or bulging, which are essential phenomena for continuous dynamic recrystallization to operate [43]. Nie *et al.* [44] showed in fact a periodic segregation pattern in twin boundaries, while Hadron *et al*. [41] confirmed that segregation proceeds without a truly describable pattern in high angle GBs. Therefore, CDRX and DDRX might be concomitantly active over the course of any thermo-mechanical processing (TMP), making nucleation and growth of grains with the RE texture difficult to examine under the microscope.

Stanford and Barnett [26] captured RE-textured grains forming within shear bands in a Mg-RE alloy, while the rest of recrystallized grains predominantly adopt a $\langle 11\bar{2}0 \rangle$ fiber. Sandlöbes *et al.* [28] corroborated this proposal and further observed that REEs promote a more uniform distribution of shear bands. However, results from several authors [15, 24, 31, 40, 45] showed the omnipresence of RE-texture without any prior formation of shear bands, thus removing the shear band hypothesis from the list of required root-cause mechanisms. Stability of RE oriented nuclei is another aspect to this puzzle, where there might be handful of randomly oriented nuclei that do not get the

chance for further growth [3]. Such nucleation sites would remain undiscovered due to the rather large progress of DRX after processing.

One could also envisage that REEs do not promote nucleation of RE-textured embryos per say, but only promote their stability during the grain growth stages. Thus, the role of grain growth in the grain orientation selection/elimination process must be clarified. While traditional Mg alloys tend to sharpen their texture during static annealing [3, 46], RE-containing Mg alloys do exactly the opposite [34]. Accordingly, one can confidently hypothesize that RE-addition manipulates growth preferences with a specific bias [47].

Recent analyses by the present authors of the misorientation relationships that occur between recrystallized grains and their parents in traditional Mg alloys (AM30) demonstrated the key role that GB energy and mobility play in texture formation and stabilization during nucleation and growth of recrystallized grains, respectively. Cusps in GB energy around a given Taylor axis acts as a trap for rotations of sub-grain, prompting them to settle at singular boundaries, usually twin boundaries, and as such, only a few orientations became favored during the nucleation process. Moreover, some of these boundaries have extremely high mobility, seeing their grains grow abnormally and prevail in the final texture. In this paper, we hypothesize that these mechanisms, which explain sharp texturing in classical Mg alloys, are altered by REEs in a fashion that would lead to the RE-texture and ensuing texture randomization. This hypothesis is supported by the universal agreement that REEs tend to segregate at GBs [39]. Strong GB drag effects have been observed in ternary alloys containing both Ca and Zn, which suggests important co-segregation effects beyond solute segregation of the individual

72

species [48]. We attempt to identify some of the key mechanisms that govern the effect of REEs on the behavior of GBs during nucleation and growth.

We examine four REE containing alloys with different DRX resistance, and vary the processing conditions to track the changes in microstructure and texture evolutions from the nucleation stage to the point where the grain growth stage is nearly completed. Exploiting predesigned processing parameters enables us to identify the most important nucleation sites, and examine the influence of static and dynamic recrystallization on the growth of grains with new orientations.

3.2 Experimental procedure

3.2.1 Alloy compositions

We tested four alloys containing Al, Mn and Y but with varying concentrations of Zn and Mischmetal (MM, see Table 1), and applied two ram speeds to all of them. The purpose of adding Al, Mn, and Zn was to understand the effect of REEs on RE texture formation within complex alloy compositions that have recently been developed by alloy designers. In fact, Mn additions are usually added to getter Fe from solid solution, which would be otherwise deleterious to the corrosion resistance.

Table 3.1   Chemical composition of the experimental alloys in wt. %.

Alloy	Composition (wt. %)				
	Zn	Al	Mn	Y	MM
A	1.20	0.53	0.27	1.70	0.02
B	1.10	0.49	0.30	2.20	0.41
C	0.40	0.57	0.29	2.05	-
D	0.41	0.58	0.29	2.04	0.30
MM composition: 55.90 Ce-30.50 La-6.80 Pd-5.20 Nd-1.60 others (wt. %)					

Chemical compositions were measured by ICP-AES method. The balance metal is Mg.

The Al content was higher than most Mg-RE alloys (>0.2%), but as we will see, it did not hamper formation of RE texture components. Zn content was high in two alloys (1.2 wt. % for Alloys A and B) and low for the other two (0.4 wt. %, Alloys C and D). One of the Zn-rich alloys (Alloy B) was enriched in MM, while the other one was left without, and the same was applied for the two other alloys with low Zn content. Y was added to all the four alloys with a concentration substantially above the threshold for texture weakening observed in binary Mg-Y alloys. However, one should bear in mind that presence of Zn and Al may change the threshold limit as Y tends to segregate into the Mg-Zn-Y precipitates and RE containing aluminides [47, 49]. Nevertheless, the nominal content of Y was high enough to enable RE texture formation even in alloys with highest concentrations of Zn and Al, and no MM.

MM has slow bulk diffusion in Mg, so when it exists in high concentrations (e.g. Alloy B), particularly when accompanied by Zn, recrystallization kinetics are expected to be relatively slower. In fact, co-segregation of Zn and MM into the grain boundaries is believed to retard recrystallization kinetics [48]. As such, their effect will be important during grain growth when the kinetics of recrystallization are counterbalanced by a high extrusion speed, promoting the density of nucleation sites through larger area reduction/plastic strain. In contrast, at low extrusion speed, where recrystallization is supposed to be slow, the absence of MM (Alloys A and C) makes it suitable to observe the effect of Y on the development of RE texture during grain nucleation. In general, the slow recrystallization kinetics at low extrusion speed are expected to allow tracing nucleation of grains with an RE/random texture type orientation at early stages for all alloys as they all contain Y. Similarly, the fast kinetics are expected to allow appreciating

74

how varying concentration of REEs, with or without Zn, affects the overall texture strength and RE texture development during dynamic recrystallization and grain growth. The chemical composition of the alloys are listed in Table 1.

3.2.2   Experiments

The alloy billets, in cast condition, were solution annealed at 450 ºC for 10 h under flowing argon gas atmosphere followed by immediate water quenching. After annealing, the chemical composition was analyzed using atomic emission spectroscopy (ICP-AES) method. Solution treated alloys were machined to cylindrical specimens ~32 mm (1.25 in) in diameter and ~25 mm (1 in) and were subject to indirect extrusion at a ram speeds of 10 mm/min and 40 mm/min with an area reduction ratio of 6 at 450 ºC followed by air cooling. Post annealing was conducted for 20 and 180 mins at 450 ºC on select samples to address the influence of static recrystallization and further grain growth. Samples were cut along the radial and transverse directions to examine the microstructural and texture evolutions on planes normal to extrusion direction (ED) and normal to extrusion radial direction (ERD). The extrusion radial direction is a radial direction of the cylinder that is normal to ED.

The different samples were then characterized using several different techniques. Samples were extracted from the center of the extrudates in the steady state region, and were ground by standard metallographic techniques and polished using 0.06 μm colloidal silica (Struers OPS) for 10 min. In preparation for electron back scattered diffraction (EBSD), Electro-polishing was carried out on polished samples in chilled Struers C1 solution at 25 V for 120 s. Samples were sonicated for 20 min after preparation in absolute ethanol to remove artifacts from the surface. Texture measurements were

conducted on transverse cross-sectional (plane normal to ERD) and radial cross-sectional (plane normal to ED) planes using EBSD and X-ray diffraction (XRD), respectively. EBSD analyses were performed using a field emission scanning electron microscope (SEM) at the operating voltage of 20 kV. XRD macro-texture measurements were conducted by measuring six incomplete experimental pole figures from $\alpha = 5°$ to $\alpha = 80°$ using Cu-Kα radiation at 40 kV and 30 mA with a Rigaku-SmartLab. The experimental pole figures ($\{0002\}$, $\{10\bar{1}0\}$, $\{10\bar{1}1\}$, $\{10\bar{1}2\}$, $\{10\bar{1}3\}$, $\{11\bar{2}0\}$) were used to calculate the orientation distribution function (ODF) using MTEX toolbox in MATLAB [50]. TEM discs with 3 mm in diameter were punched from foils grounded to the thickness of 200 μm followed by ion milling at 3.5 kV until perforation. TEM imaging and STEM EDX analysis were conducted by a JEOL 2100 TEM operating at 200 kV.

3.3   Results and Discussion

The outcomes of this study are organized in the following manner. The experimental results are separated into the texture and microstructure evolutions during low and high speed extrusions (Section 2.3.1). Section 2.3.2 explores DRX nucleation sites and the role of active recrystallization mechanisms exploiting low speed extrusions in the early stages of recrystallization. Afterwards, the results of fast extrusion along with post annealing not only did display the significance of the grain growth on texture evolutions, but also unraveled some discernable distinctions in the texture patterns of the dynamically and statically recrystallized samples (Section 2.3.3).

3.3.1   Influence of chemical composition and extrusion condition

In order to analyze the effect of extrusion condition and chemical composition on texture modification of RE, a series of extrusions at 10 and 40 mm/min and 450 ºC were conducted. Faster recrystallization kinetics during high-speed extrusion pertain to a higher nucleation rate of DRX grains, which is granted by the high level of the strain energy delivered and stored in the matrix.

3.3.1.1   Texture evolution

3.3.1.1.1   Low speed extrusions

Figure 3.1a-d shows recalculated XRD inverse pole figures of the four slowly extruded alloys. Recalculated inverse pole figures reveal a quite strong $\langle 10\bar{1}0 \rangle || ED$ fiber texture along with a relatively weak RE-texture. This RE-texture has been identified to lie very closely to $\langle 22\bar{4}3 \rangle || ED$ component. For traditional Mg alloys, $\langle 10\bar{1}0 \rangle$ fiber has been shown to correlate with the parent grains and a portion of the recrystallized grains [51]. For the parent grains, it results from extensive basal, pyramidal $\langle c + a \rangle$ and prismatic slip modes, which, having the $\langle 10\bar{1}0 \rangle$ and $[0001]$ as Taylor axes, respectively, align the basal planes with ED. Our texture and micro-texture analyses indicate that this must be also the case for the present alloys. Due to small area reduction ratio (i.e. 1:6) and thus, probably a lack of sufficient stored deformation energy, approximately over 85% area fraction of the microstructures in Figure 3.1a-d are composed of deformed grains. Hence, the texture intensities remain noticeably high. However, these high texture intensities did not prohibit formation of strong RE texture component [34].
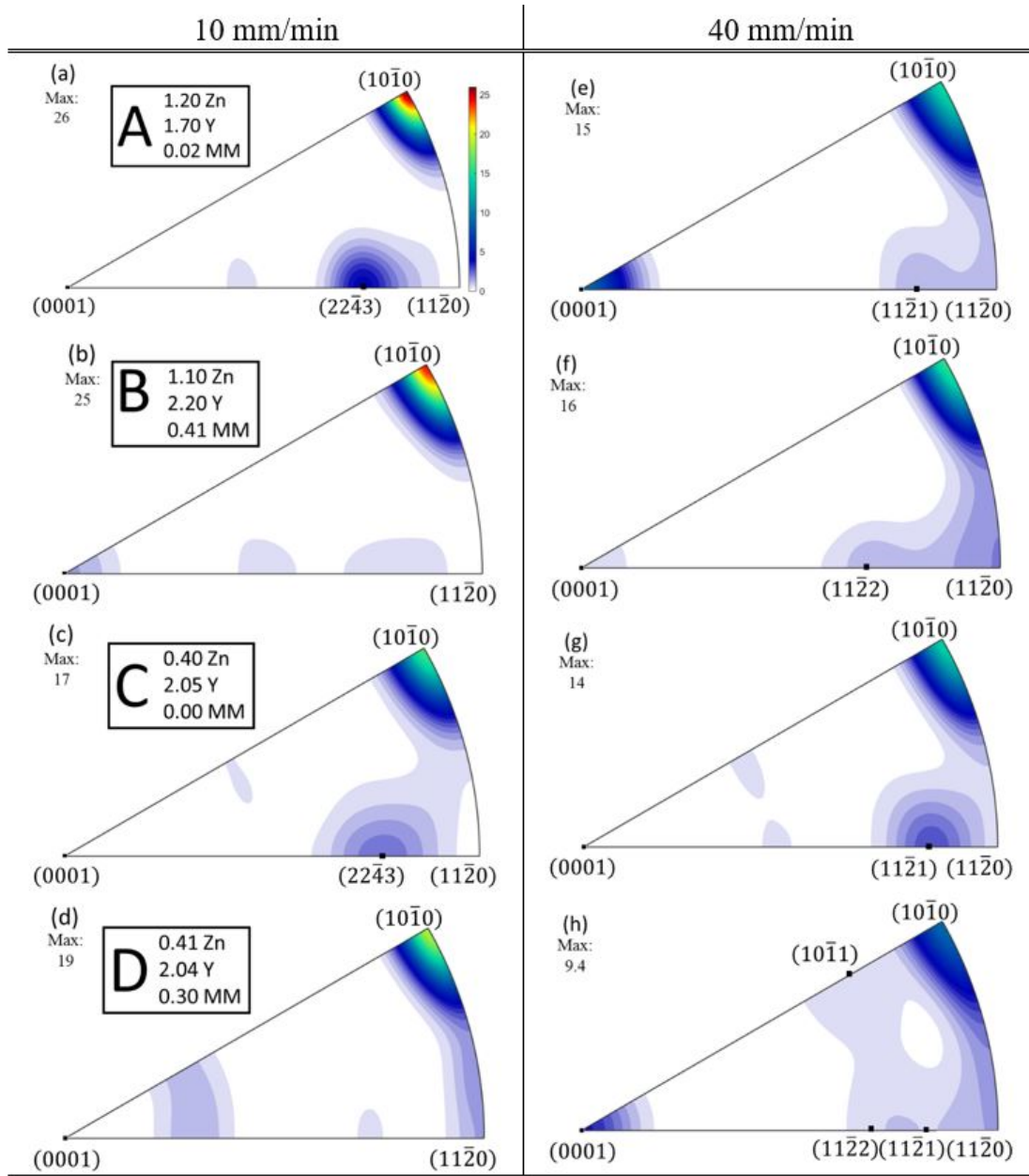
Figure 3.1   Recalculated inverse pole figures (IPF) of extruded alloys.

After 10 and 40 mm/min – 450°C extrusion (with 1:6 area reduction ratio) of (a, e) Alloy A with 1.2% zinc and 0.02% Mischmetal; (b, f) Alloy B with 1.1% zinc and 0.41% Mischmetal; (c, g) Alloy C with and 0.4% zinc and no Mischmetal, and (d, h) Alloy D with 0.41% zinc and 0.31% Mischmetal. All alloys contain about 2% of yttrium. The accuracy of texture measurements was ±0.2. IPFs refer to extrusion direction. The concentration of key elements are also noted on the IPFs in wt. %.

This must be due to the relatively pronounced presence of Y, which despite the presence of Zn, Al, and Mn and their ability to reduce its solid solution content by precipitation, was added in sufficient quantities to prompt nucleation of grains with orientations characterizing the effect of REEs (Figure 3.1a and Figure 3.1c). However, relying only on the content of REEs to expect texture weakening entails that alloys D and B, having the highest contents of MM should have the weakest texture of them all. In reality, Alloy C has the lowest maximum texture intensity value among the slowly extruded billets. This apparent contention is explained by the difference in the rate of recrystallization, which is relatively faster in Alloy C with no MM. As previously indicated, the kinetics of recrystallization is dependent upon the combined amount of Zn, Y and MM content of the alloys which would tend to slow down recrystallization. In fact, a high combined content of these elements could result in an increased mutual segregation and/or diffusion in dislocation core, which would hamper grain boundary and/or dislocation mobility [48]. Therefore, it is no wonder why Alloy C, having the lowest net content of Zn, Y and MM, developed the lowest texture intensities. Actually, according to this interpretation, the kinetics are expected to be faster in the following order: $Alloy\ C \geq Alloy\ D \gg Alloy\ A > Alloy\ B$, which is fully consistent with our observations (Figure 3.2). However, as the development of RE texture hinges on mutually fast recrystallization kinetics and higher REE concentrations, Alloys A and C showed higher intensities of RE texture than Alloys B and D (Figure 3.1). Alloys A and C in fact had sufficient fraction of DRX grains for the RE texture to emerge in the texture plots.

79
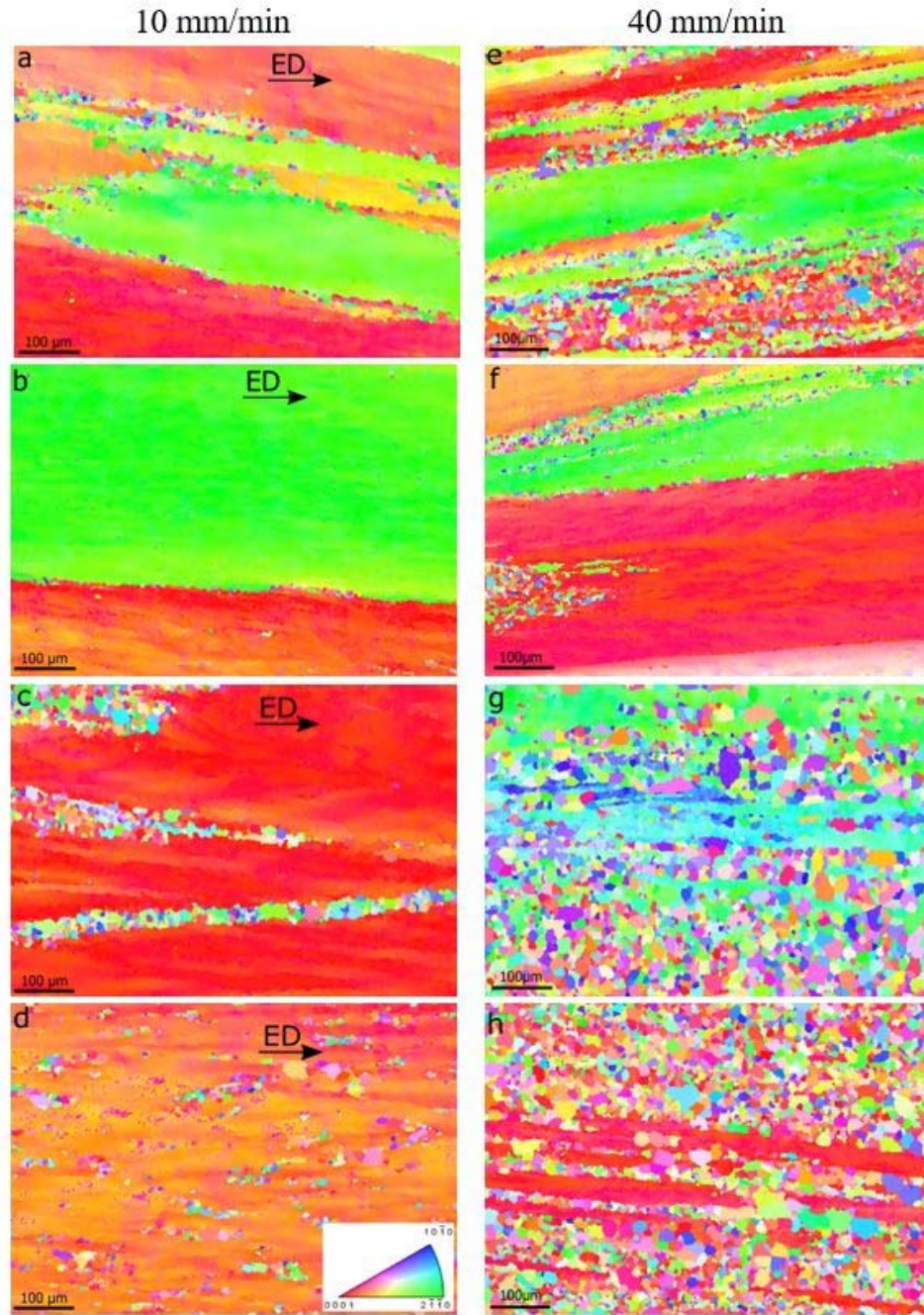
Figure 3.2   Inverse pole figure maps of extruded alloys.

(a, e) Alloy A with 1.2% zinc and 0.02% Mischmetal, (b, f) Alloy B with 1.1% zinc and 0.41% Mischmetal, (c, g) Alloy C with 0.40% zinc and no Mischmetal, and (d, h) Alloy D with 0.41% zinc and 0.30% Mischmetal after 10 and 40 mm/min – 450°C extrusion with 1:6 area reduction ratio. The concentration of key elements are in wt. %

Y and MM ought to be high enough to produce typical RE effect, while net Zn, Y and MM concentration should be sufficiently low to allow for reasonable amount of recrystallization to occur. That is, while the texture component became more diversified as MM concentrations increased, RE texture evolution was substantially delayed so much so that it was hardly any visible in Alloys B.

From a statistical point of view, the intensity of RE texture depends on the density of available nucleation sites and the stability of their nucleated grains during the grain growth stages. For instance, EBSD analyses indicate that Alloy A (with less MM content) has relatively thinner bands of deformed grains than Alloy B, and hence more GB area and a higher probability for the RE orientations to nucleate (Figure 3.2a-b). Additionally, as mentioned, DRX kinetics were very sluggish in Alloy B due to the higher concentrations of MM that obstruct GB motion [43]. Hence, in stark agreement with the results of recalculated IPFs shown in Figure 3.1, Alloy B has less potential for developing RE texture than Alloy A. Furthermore, Alloys C and D with slightly higher volume fraction of DRX grains than Alloys A and B, as illustrated by Figure 3.2a-d, exhibit smaller maximum texture intensities (Figure 3.1). Comparing the IPFs of Alloys C and D in Figure 3.1 proves that the intensity of RE-texture component is directly connected to the DRX kinetics. Having undergone slower DRX kinetics due to the greater net amount of MM, Alloy D develops reduced RE texture intensities than Alloy C (no MM additions). Finally, Alloy D displays a weaker texture compared to all others alloys, which had either a slower recrystallization rate (Alloy B) or a lower fraction of MM content (Alloy C). Thus, Y proves less effective than MM in texture modification.

3.3.1.1.2　　　**High speed extrusions**

The highly stored energy level associated with the high-speed extrusion allowed substantial texture weakening, as intensities were approximately 10 m.r.d. (multiple of a random distribution) less than those retrieved from low-speed extrusion (Figure 3.1). IPF mapping shows that Alloys C and D have developed a higher fraction of DRX grains and a wider range of texture components than Alloys A and B (Figure 3.2e-h). However, RE texture (e.g. $\langle 11\bar{2}1 \rangle \, || ED$) was pervasive in all the four alloys. Alloy D exhibited the most versatile texture components owing to the added presence of MM. In contrast, Alloy A not only recrystallized slower, it did not benefit from MM. However, it still shows RE texture atop of a stronger $[0001] \, || ED$ component. This phenomenon underscores that the all alloys tend to develop RE texture during the nucleation stage, but it is just a problem of the kinetics for this texture to manifest itself in the IPFs.

As pointed out, in addition to a pervasive $\langle 11\bar{2}1 \rangle \, || ED$ texture component for all alloys, there is a fairly high fraction of grains having the basal pole parallel to ED, i.e. $[0001] \, || ED$, (Figure 3.2e-h). These grains have been detected in IPF maps, revealing that the misorientation angle and axis across the GB are approximately $90 \pm 2°$ and $[13 \, \bar{27} \, 14 \, \bar{1}]$, respectively. This misorientation axis is actually very close to $\langle 1\bar{2}10 \rangle$. There are two very low energy GBs that fall close to this misorientation relationship. First is the coherent $\{10\bar{1}2\}$ twin boundary (TB) with about 87° misorientation angle, and the second is the basal-prismatic (BP) asymmetric tilt GB with 90° misorientation. Barrett and El Kadiri [52] demonstrated that the BP boundary develops the lowest excessive potential energy among all asymmetric-tilt boundaries observed in the literature. In addition, it systematically facets with the $\{10\bar{1}2\}$ TB making it easy to form

two-dimensional embryos. The low energy of this type of boundary may be a driving

force for DDRX/parent interface may be the driving force for nucleation and growth of

such a boundary, leading to a new texture component in the microstructure.

3.3.1.1.3 Microstructural observations

Figure 3.2 shows typical microstructures obtained by slow and fast extrusion. The

grains in pancake-like morphology lying parallel to the extrusion direction correspond to

parent grains. Their orientations are majorly clustered near the $\langle 10\bar{1}0\rangle||ED$ fiber,

accounting for the sharp texture intensities in the calculated inverse pole figures in

Figure 3.1. Both shape and orientation of grains develop in a similar fashion as in

traditional Mg alloys, prompting GBs with a predominant tilt character.

Alloy B shows comparatively a dearth of recrystallized grains, (Figure 3.2b and

2.2f) but very large parent grains. Next, recrystallized grains in fine lines are detectable in

Alloy A as they nucleate on GBs between parent grains. Alloy D exhibits a higher

fraction of recrystallized grains than Alloy A, but they seem to spread more

homogeneously in the matrix, whereas GBs of parent grains remain harder to define. In

Alloy C, uninterrupted necklaces of recrystallized grains decorate most GBs in relatively

thick lines. These microstructural observations substantiate the order of recrystallization

kinetics between the four alloys described in the previous section.

3.3.2 Contribution of recrystallization mechanisms

One approach to elucidate the mechanisms of dynamic recrystallization is to

generate partially recrystallized microstructures in which it is possible to find

recrystallized and parent grains together, allowing details of the misorientation

relationships between the two to be examined. In this study, we were able to track the DRX behavior from the very early stages by performing low speed and low area reduction ratio types of extrusions on Mg-RE alloys, having various levels of DRX resistance. As such, we are able to assess the relative contributions of concurrently active DRX mechanisms in the development of new texture components.

3.3.2.1 Continuous dynamic recrystallization, CDRX

The slow recrystallization kinetics in Alloy B, having the highest sum of Y, MM, and Zn concentrations among all other alloys, and low speed of extrusion enabled us to capture early stages of CDRX. The IPF maps of Figure 3.3 illustrate that CDRX occurs in Alloy B through formation of elongated grains with $\langle 10\bar{1}0 \rangle$ fiber texture component (Figure 3.3a), which may result in a sharper fiber texture. CDRX assisted the parent grains to rotate around their $\langle 10\bar{1}0 \rangle$ poles by rotation of sub-grains, and they contribute to the $\langle 10\bar{1}0 \rangle$ fiber texture component in the extruded condition, in good agreement with XRD recalculated inverse pole figures (Figure 3.1b). Rotation around $\langle 0001 \rangle$ occasionally took place (Figure 3.3b), revealing the formation of subgrains from arrays of prismatic dislocations. This seems to be also in good agreement with the results by Hadorn *et al.* [40] who reported the predominance of either $[0001]$ or $\langle 10\bar{1}0 \rangle$ Taylor axes but not both in any CDRX grain nucleation event. After the rotation of sub-grains inside the elongated grains, wide bands of deformed grains set the stage for other restoration mechanisms to begin.
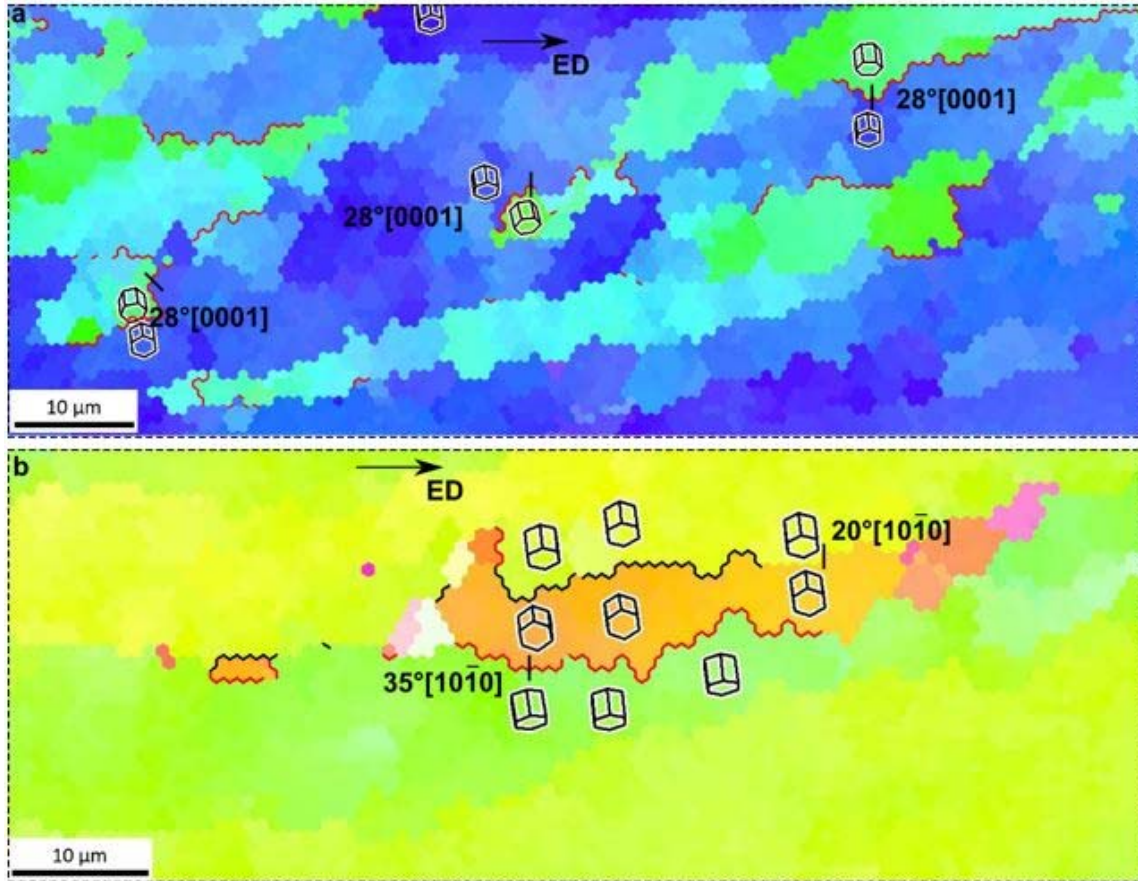
Figure 3.3   Electron backscattered diffraction analyses revealing dynamic recovery taking place in Alloy B.

Extruded at 450 ºC with 10 mm/min ram speed. (a) An inverse pole figure ED map showing continuous dynamic recrystallization by 28° rotation around [0001] axis. (b) An inverse pole figure ND map showing continuous dynamic recrystallization by rotations around ⟨10$\bar{1}$0⟩.

3.3.2.2   Discontinuous dynamic recrystallization, DDRX

Throughout our microstructural investigations, we observed immense activity of bulging and nucleation of recrystallized grains at the GB protrusions, which is fully consistent with discontinuous dynamic recrystallization (DDRX) [53]. Therefore, we focus on this mechanism and its consequent effects on texture nucleation in detail.

85

3.3.2.2.1   Nucleation sites

Figures 3.4 and 3.5 depict typical misorientation profiles and their corresponding axis/angles. The IPF maps were taken from planes normal to ERD. The misorientation axes for all the calculated axes/angles correspond essentially to $\langle 10\bar{1}0 \rangle$ with slight deviations due to the relatively trivial activity of other slip modes [3]. The range of measured angles was $\sim 70 - 80°$ for interfaces between bands with orientations close to $[0002]/\langle 11\bar{2}1 \rangle \| ERD$, $\sim 41 - 52°$ for ones close to $\langle 11\bar{2}0 \rangle/\langle 11\bar{2}2 \rangle \| ERD$, $\sim 51 - 60°$ for ones close to $\langle 11\bar{2}0 \rangle/\langle 11\bar{2}3 \rangle \| ERD$ and $\sim 21 - 24°$ for ones close to $\langle 11\bar{2}2 \rangle/$ $\langle 11\bar{2}3 \rangle \| ERD$. Assuming those interfaces to be perfectly aligned with the corresponding poles, the misorientation angles would be $2\theta = 61.4°$ for $[0002]/\langle 11\bar{2}1 \rangle$ interface, $2\theta = 47.1°$ for $\langle 11\bar{2}2 \rangle/\langle 11\bar{2}0 \rangle$, $2\theta = 58.3°$ for $\langle 11\bar{2}0 \rangle/\langle 11\bar{2}3 \rangle$, $2\theta = 11.1°$ for $\langle 11\bar{2}2 \rangle/\langle 11\bar{2}3 \rangle$. Differences between the calculated and measured angles are attributed to the misalignment between actual directions and presumed ones. It is worth noting that the frequent presence of these boundaries could be rationalized by their low energy, which makes them more favorable during dislocation recovery (See Figures 3.3 and 3.5).

Atomistic simulations have helped to explain some of the observed grain boundaries within experimental samples. For example, Wang *et al.* [54] calculated angles for $\langle 10\bar{1}0 \rangle$ symmetric tilt grain boundaries (STGB)s in Mg. Tilt angle, θ, locate at 28.41°, 39.06°, 58.36°, 72.88° for the observed energy cusps in the excess potential energies diagram for $\langle 10\bar{1}0 \rangle$ STGBs. In addition to STGBs, quite a few asymmetric tilt boundaries have been identified for HCP structures. Bruggeman *et al.* [55] identified the potential symmetric and asymmetric tilt boundaries for rotations around $\langle 10\bar{1}0 \rangle$, $\langle 11\bar{2}0 \rangle$, $\langle 0001 \rangle$ axes based on the coincidence-site lattice (CSL) and near-CSL theory. According

to this theory, in near-CSLs for $\langle 10\bar{1}0 \rangle$ tilt boundaries some asymmetric structural units

would possess shorter periods than symmetric structural units, and hence, many of the

$\langle 10\bar{1}0 \rangle$ tilt boundaries composed of short structural units are asymmetric. The potential

near-CSL $\langle 10\bar{1}0 \rangle$ tilt boundaries identified by Bruggeman *et al.* [55] are as follows: $\sum 10$

with $2\theta = 78.6^{+0.2}_{-0.5}$, $\sum 11$ with $2\theta = 62.8^{+0.5}_{-0.1}$, $\sum 11$ with $2\theta = 35.3^{+0.7}_{-1.1}$, $\sum 14$ with $2\theta =$

$44.4^{+0.2}_{-0.2}$ and $\sum 25$ with $2\theta = 23.0^{+0.2}_{-0.1}$. Among the actual GBS captured in the

microstructures, ones with 2θ values of $\sim70° - 80°$, $\sim51° - 60°$, $\sim41° - 52°$, and

$\sim21° - 24°$ seem to fall very close to $\sum 10$ or $(\bar{2}114)$ STGB, $(\bar{2}116)$ STGB, $\sum 14$ and

$\sum 25$ near-CSL boundaries, respectively. As mentioned above, the rotation axis was

rather close to $\langle 10\bar{1}0 \rangle$. Actually, the close match between the theoretical and

experimental axis/angles may suggest that the low energy of such GBs is the reason

behind their abundance. As such, they are frequently observed in Mg and HCP

microstructures, and they are the most active sites for nucleation of grains with new

orientations including RE component.

3.3.2.2.2   Evidence of Bulging

The relatively slow recrystallization kinetics in Alloy A allowed revealing an

important feature in the deformed portion of the microstructure. Throughout the sample,

GBs between parent grains display significant serrations, which manifest as local

protrusions of about 5 μm in diameter spreading along the entire interface length (Figure

3.4c and 3.4a). These GB protrusions correspond to bulging phenomena that have been

traditionally associated with discontinuous dynamic recrystallization (DDRX) events [3].
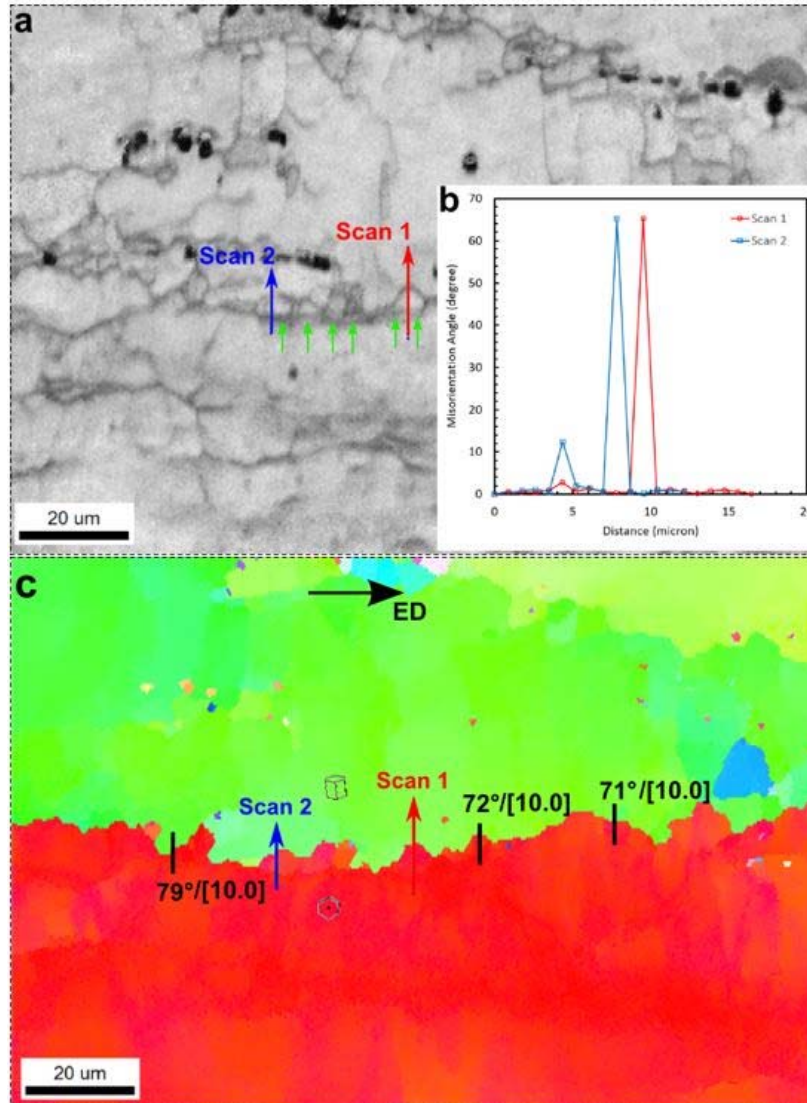
Figure 3.4   Electron backscattered analyses of alloy A.

In terms of (a) an image quality map and (c) corresponding inverse pole figure maps revealing substantial bulging of a very stable $70-80°/[10\bar{1}0]$ boundary with minimum misorientation fluctuation along the interface. The image quality map reveals also the formation of low angle boundaries at the backside of most grain boundary protrusions (indicated by green arrows). (b) The misorientation angle of these low angle boundaries range from 2 to 10º indicating the occurrence of DDRX.
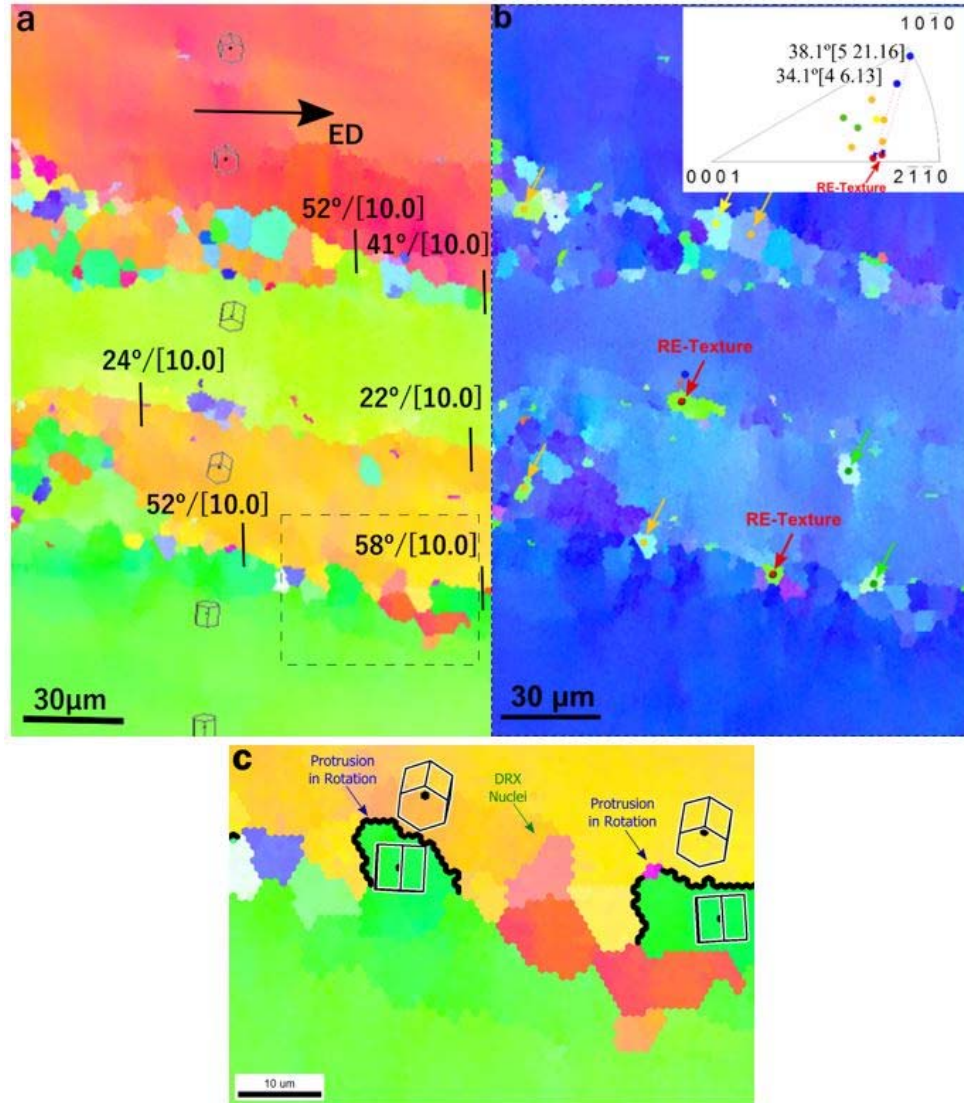
Figure 3.5   Inverse pole figure maps of Alloy A extruded at 450 ºC with 10 mm/min ram speed.

Revealing (a) high angle boundaries subject to recrystallization through the bulging mechanism. The ED-mapped IPF in (b) allowed discerning grains with orientations characteristic to the effect of rare earth including the RE-texture (indicated with red arrows). The IPF map illustrates the rotation of two parent grains toward the RE-texture orientations as well as formation of several random orientations from the same parents. The IPF map in (c) reveals two protrusions still in intermediate stages of recrystallization as well as some protrusions that almost completed the recrystallization process by developing into a grain with random orientation, which were indicated by arrows in (b).

Close examination of many locations in Figure 3.4 shows that the GB misorientation remains pretty much the same along the wavy interface, indicating that the boundary misorientation is relatively stable with respect to the action of plastic deformation (Figures 3.4a-c). Traditionally, GBs act as an effective source of defects and host much of the sub-grain formation during recovery, so their associated misorientations tend to fluctuate. Figure 3.6 is a bright-field STEM image with EDAX mapping of Zn and Y in Alloy A taken at areas adjoining a GB. These chemical analyses reveal the segregation of Zn to the grain boundaries. By co-segregating to GB free volume sites or substituting for Mg GB sites, Zn and Y co-segregation may lead to significant solute drag effects [40, 41, 44]. Zn in classical alloys such as AZ31 or AZ61, though added with concentrations as high as in Alloy A, does not segregate with as much intensities.
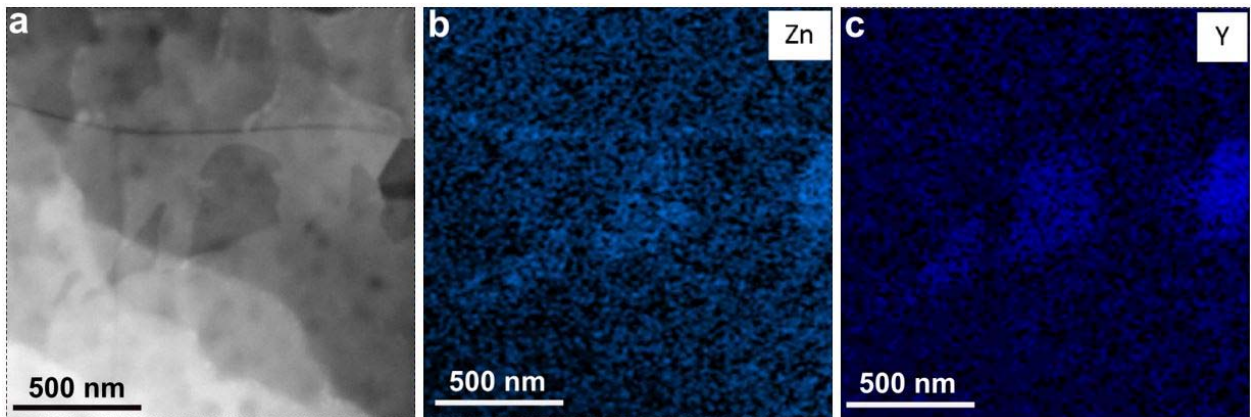
Figure 3.6   TEM analysis of an extrudate from alloy A.

(a) A bright field scanning transmission electron microscopy (STEM) image of a region taken near a grain boundary in Alloy A on which energy dispersive X-ray mapping of (b) zinc, (c) yttrium revealed substantial segregation of zinc into the boundary. Moreover, intermetallic particles seems to be rich with zinc and yttrium after extrusion at 450 ºC and under 10 mm/min ram speed.

Nie et al. [44] observed in fact a strong co-segregation potential of Gd and Zn in Mg, which is greater than if either Zn or Gd exist in the alloy. Similar co-segregation enhancements were observed when Ca was added atop of Zn [48, 56]. This binding effect is attributed to the atomic size effects (small - Zn) and (large - Gd, Y) [57].

3.3.2.2.3   Bulging mechanism

Bulging along GBs during high temperature recrystallization comprises two stages that are essential for describing the effect of REEs. The first stage corresponds to the mechanisms that drive migration of the GB, while the second stage relates to the inhomogeneity of this migration, giving rise to the observed protrusions.

During high temperature deformation, dislocation climb and cross-slip are common modes of recovery. It has been widely admitted that REEs of the likes of Y and MM, when added to Mg, tend to reduce the stacking fault energy (SFE) on basal planes [28], and hence, disrupt the ease of cross-slip and climb [20]. Inhibiting recovery processes sets the stage for recrystallization by a range of mechanisms including the GB migration mechanism known as strain-induced boundary migration, or SIBM [53].

TEM and STEM analyses revealed precipitates, which could contribute to the serrated structure of the interface (Figures 3.7a-b). Upon migration, GB may have advanced in the spaces between particles so its surface became bulged around precipitates. These fine particles had long periodic hexagonal structure Mg solid solution and cube $Mg_{24}Y_5$ [58]. STEM analyses also revealed particles that were rich in Y, Zn and Al (Figures 3.8a-d), suggesting they correspond to the eutectic β (FCC) phase which was

identified in ternary and complex Mg-RE alloys to precipitate through a four stage

process from a super-saturated solid solution [59-61].
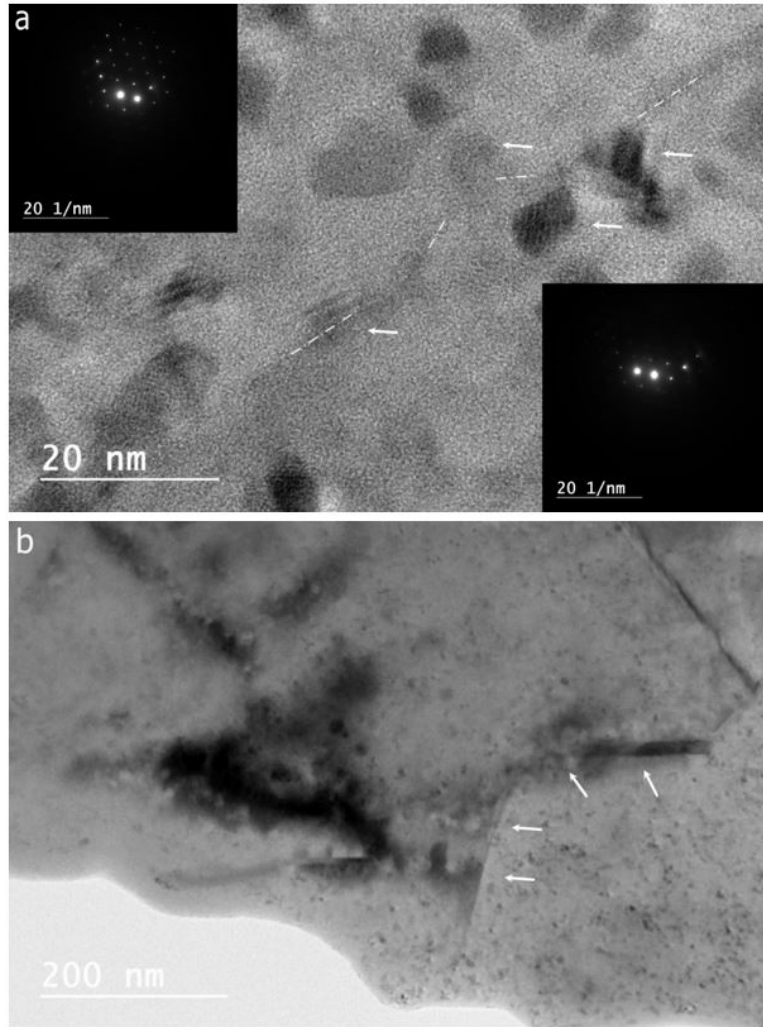
Figure 3.7   Bright field transmission electron microscopy images of alloy A.

Extruded at 450 ºC with 10 mm/min ram speed showing: (a) a low angle grain boundary with a local protrusion in the midst of several particles, and (b) a beta precipitate that induces the formation of a grain boundary protrusion indicated by white arrows.
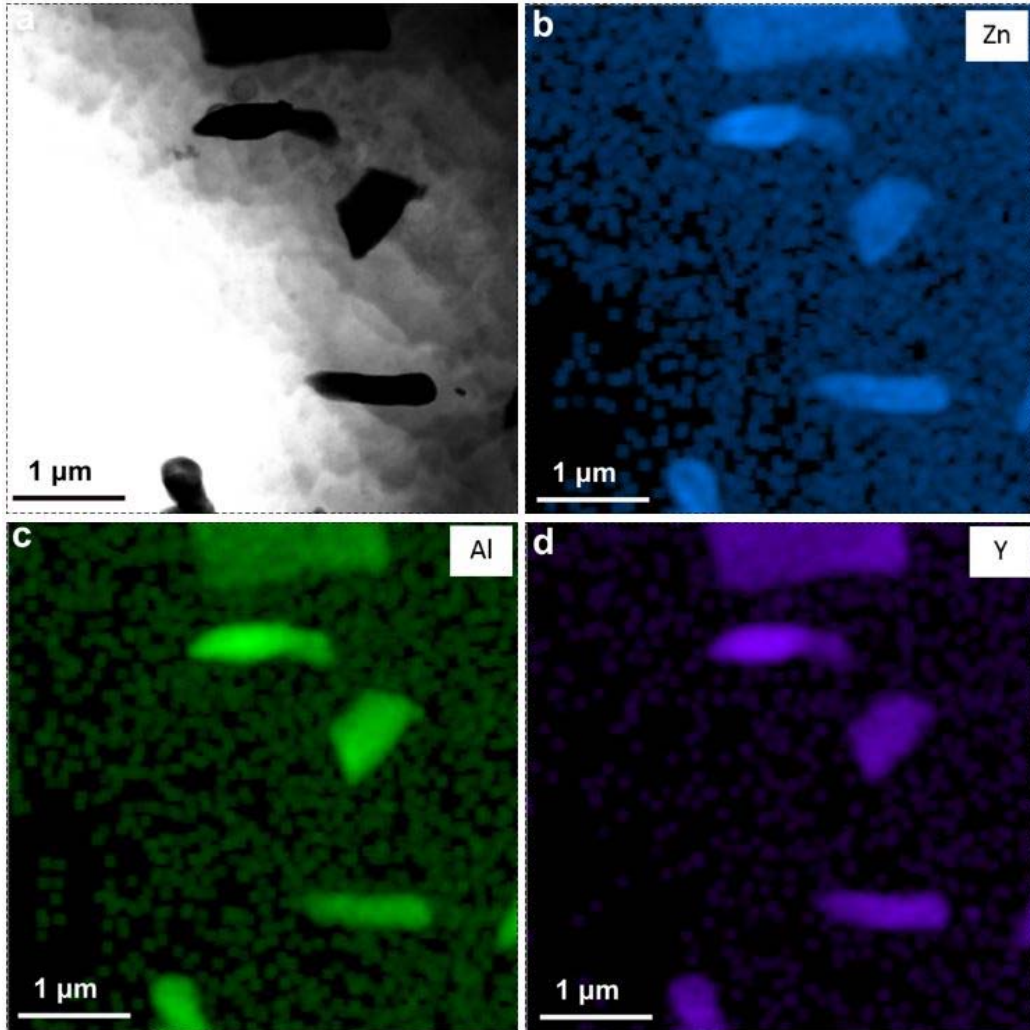
Figure 3.8   STEM analysis of alloy A.

(a) A bright field transmission electron microscopy image on which energy dispersive (EDS) X-ray maps of (b) Zn, (c) Al and (d) Y revealed the abundance of coarse beta particles in Alloy A extruded at 450 ºC with 10 mm/min ram speed.

3.3.2.2.4   Nucleation of new orientations

In this section, the slow-recrystallizing microstructures are examined to identify early stages of nucleation events between parent grains and their daughters. We carefully examine the misorientation relationships developing before and after the new orientations stabilize, further clarifying the role of GB nucleation.

The image quality map associated with the IPF map in Figure 3.4a reveals that the GB protrusions are consistently accompanied by low-angle boundaries forming at the backside of the crests (Figure 3.4a). Misorientation profiles across these crest areas typically displayed in Figure 3.4b and 4c demonstrate that these low angle boundaries make misorientation angles evolving between 2° to 10°. The gradual formation of these low angle boundaries at the base of the crests are clearly a trademark of the bulging-induced DDRX grain nucleation mechanism proposed by Sitdikov and Kaibyshev [21]. These authors suggested that the process takes place through three stages. Beginning with SIBM-induced bulging, a subsequent confined strain localization stage promotes formation of a low-angle boundary at the base of the protrusion, which gives rise to an unripe nucleus. Then the process ends up with rotations that stabilize the orientation of the DDRX nucleus as it traps more dislocations at the boundaries. A more detailed schematic based on our observations throughout the extrusion process in this study is shown in Figure 3.9. It is observed that pancake shaped grains rotate around either c-axis or $\langle 10\bar{1}0 \rangle$, which results in formation of fairly wide bands of deformed grains with nearly the same crystallographic orientation (Figure 3.9a-c). Afterwards, bulging occurs at the boundaries of deformed bands of grains leading to nucleation of new orientations (Figure 3.9d-e).

The IPF maps in Figure 3.5 captured advanced stages of DDRX grain rotations, leading to different orientations than that of parent grains. These mature orientations are clearly ruled by the axis of rotation which ought to be defined by the type of dislocations generated at the protrusions. Thus, the driving force during the final GB misorientation transformation is granted by the type and density of dislocations being captured by the

94

protruded boundary segments. These dislocations upset the atomic structure of the nucleus GBs, which induces the lattice to rotate to lower the energy state and minimize the density of misfit and interfacial disconnections [62].
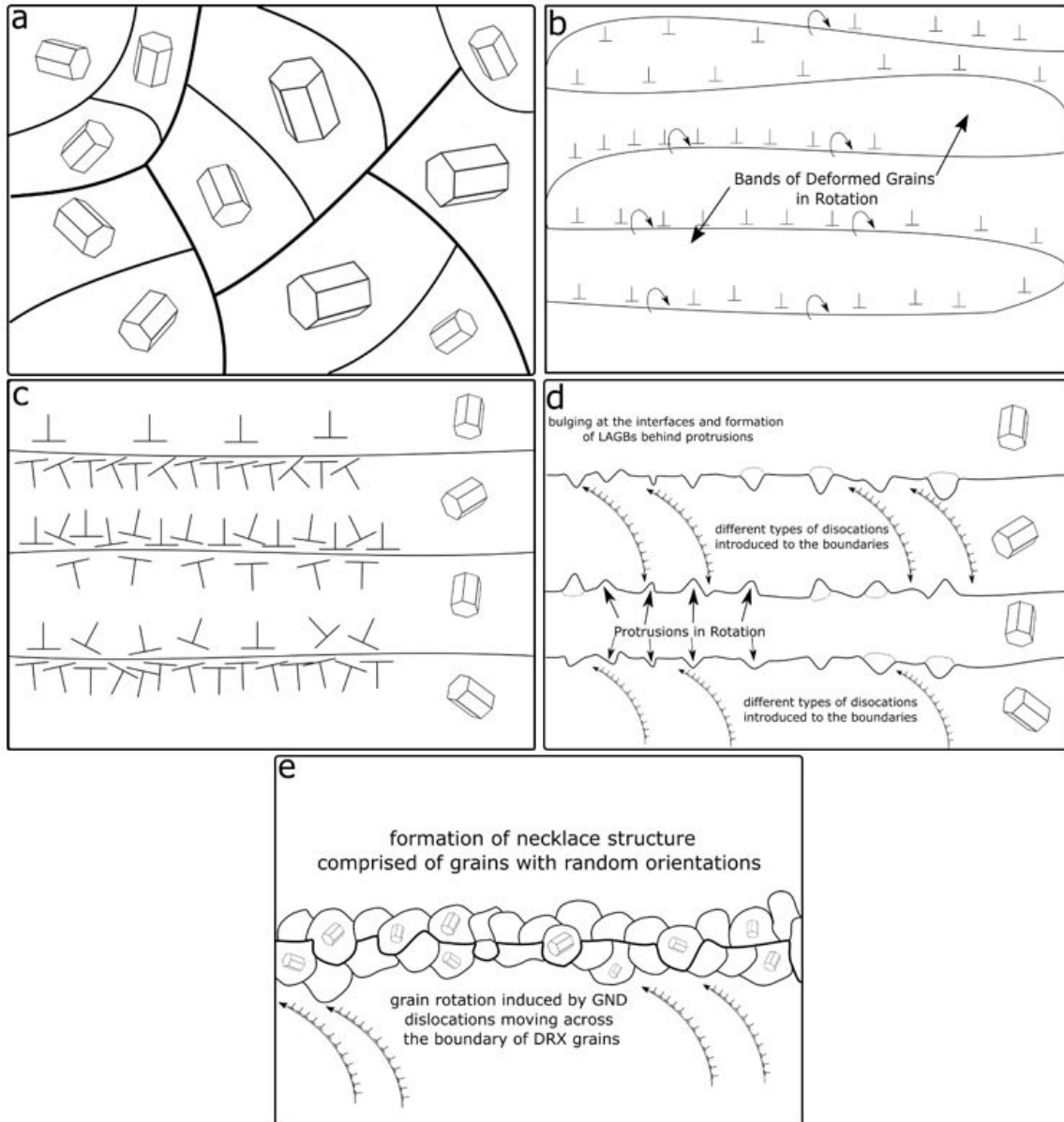
Figure 3.9   Schematic representation of dynamic recrystallization (DRX) stages.

a) a microstructure with a random texture prior to extrusion, b) early stages of extrusion expressing immature bands of deformed grains going through rotations induced by continuous dynamic recrystallization (CDRX), c)formation of stable interfaces between bands of deformed grains after the completion of CDRX, d) initiation of bulging and formation of low angle grain boundaries (LAGBs) behind the protrusion that rotate due to intake of variety of geometrically necessary dislocations, e) formation of necklace structure comprised of DRX grains with random orientations.

Phenomenologically, the total rotation of a fresh nucleus can be approximated to be a function of the density of dislocations trapped in the boundaries surrounding the nucleus. Indeed, the net rotation axis/angle between the DRX grain and nucleus could be interpreted as a total combination of geometrically necessary dislocations (GND) acting around the nucleus. The net Taylor/rotation axis of active dislocations (or slip systems) and the net amount of rotation can be hypothesized to be an arithmetic summation of all active slip systems [15, 63]:

$$\overrightarrow{T_{net}} = \Sigma_i \gamma_i \vec{T}_i \qquad (3.1)$$

Where γ_i is the shear strain induced by i^{th} slip system, and $\overrightarrow{T_{net}}$ is a vector in the direction of the rotation axis and with a magnitude equal to the total amount of rotation. DDRX grains with new and stable orientations (i.e. final stage in Figure 3.8, and RE grains in Figure 3.4) were observed on interfaces of deformed pancake-shaped grain.

For the case of RE-texture formation from a $\langle 10\bar{1}0 \rangle$ fiber, one can hypothesize a simple two-stage rotation: 28° around $[0001]$ direction, demonstrated by Barrett et al. [64] to correspond to the $\{13\bar{4}0\}$ twin followed by 28.6° around $[10\bar{1}0]$. This rotation is illustrated in Figure 3.10d for the grain nuclei exhibited in the IPF maps of Figures 3.10a-c. The decomposition of the RE texture rotation into two-step rotation is strongly supported by almost all the texture plots in Figure 3.1.
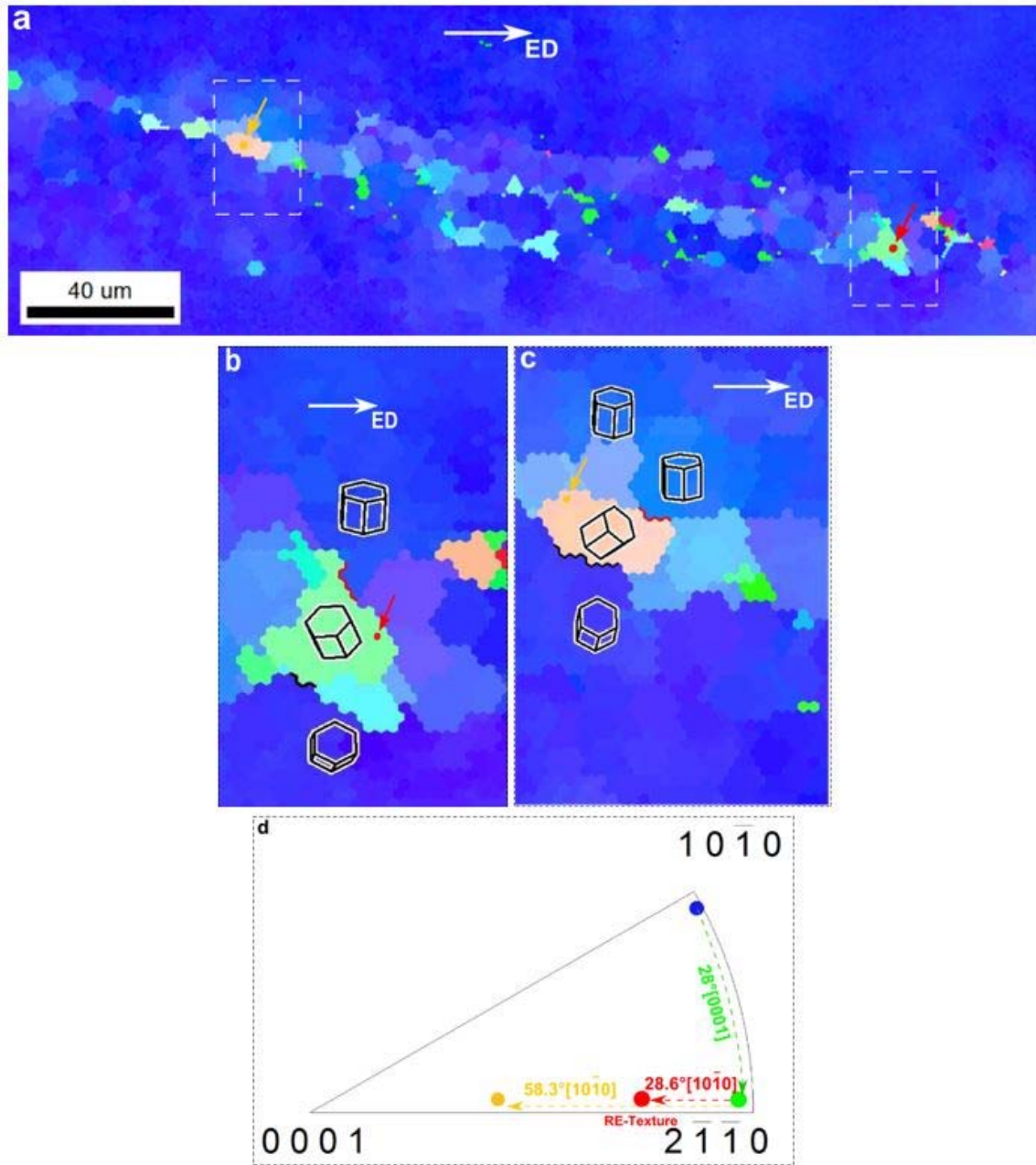
Figure 3.10   EBSD analyses showing ED-mapped inverse pole figures of alloy A.

Revealing (a-c) the development of orientation during recrystallization along a high angle grain boundary by the bulging mechanism in alloy A extruded at 450 ºC with 10 mm/min ram speed. The rotation could be decomposed into two successive rotations as illustrated in the inverse pole figure of (d). The first rotation corresponds to a 28º around [0001] characteristic of $\{\bar{4}310\}$ twinning, which is followed by a rotation around $\langle 10\bar{1}0 \rangle$ of various degrees characteristic of basal and $\langle c + a \rangle$ dislocations Taylor axis. The formation of RE-texture corresponds to a rotation of around 28.6°

In fact, the orientations quit the $\langle 10\bar{1}0 \rangle \| ED$ parent fiber by edging toward $\langle 11\bar{2}0 \rangle$ fiber and then edge again toward the RE texture. There is actually no orientations directly lying in between the $\langle 10\bar{1}0 \rangle \| ED$ and RE texture component. Texture plots and analyses of the progressive rotations indicate that the rotations proceed in two steps: (1) rotation around $[0001]$ axis, and (2) rotations around $\langle 10\bar{1}0 \rangle$ leading to the final RE-texture. According to recent work by some of the authors [65], rotations around $[0001]$ can create symmetric $\{\bar{4}310\}$ (28°) twins, so further work shall be performed if the remaining rotation around $[10\bar{1}0]$ is achieved by any $[10\bar{1}0]$ symmetric tilt twins, and whether there is a transmutation event associated with disconnections. Although pyramidal $\langle a \rangle$ slip alone cannot explain the rotations from the predominant $\langle 10\bar{1}0 \rangle$ orientation to the RE orientation, it could act in concert with basal $\langle a \rangle$ and prismatic $\langle a \rangle$ slip (or even $\langle c + a \rangle$ slip) to bring the local orientation to that of the RE orientation.

The two consecutive rotations would yield a net Taylor axis, which can be approximated by, $[7\ \bar{2}\ \bar{5}\ 8]$ and a net rotation angle of ~40º. Several misorientation axis/angle between parent and DRX grains in the IPF maps were observed to be close to the calculated values. Two instances are represented in the inset IPF of Figure 3.5b. Such a high-index Taylor axis is not close to any of the axes known for slip/twinning systems in Mg, and could only be a net sum of multiple rotations that are correlated with the active dislocation modes and how they proceed to relax the boundaries of the ripening nucleus [15]. We conducted a small step size (i.e., 0.2 µm) EBSD analysis to observe the concurrent activity of dislocations (Figure 3.11). Figure 3.11a shows the misorientations associated with the activity of basal/$\langle c + a \rangle$ and prismatic dislocations within and around the fresh DRX grains, and their net induced rotation tallies the deviation from parent

orientation. The kernel average misorientation (KAM) map in Figure 3.11b proves that

dislocation activation sites commensurate with higher degrees of misorientations, which

induce rotations through relaxation into the boundaries.
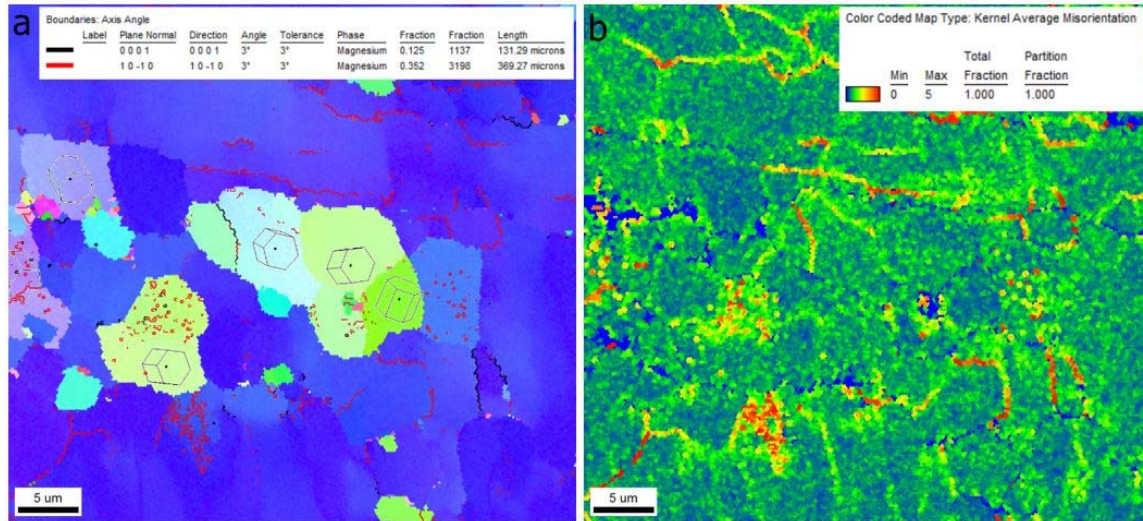
Figure 3.11   IGMA analysis of alloy A extruded at 450 ºC with ram speed of
              10 mm/min.

a) The inverse pole figure ED map depicting the presence of misorientations associated
with the activity of basal/$\langle c + a \rangle$ (red lines) and prismatic (black lines) dislocations
activity, b) the corresponding kernel average misorientation (KAM) image indicating the
higher degrees of misorientations in the sites of dislocation activity.

However, if disconnections were active in the process of GB formation, which is

very likely to occur, their shear needs to be taken into account. For instance, if the first

rotation is effected by $\{13\bar{4}0\}$ twinning due to relaxation of prismatic dislocation arrays

as identified by Barrett et al. [64, 66], any dislocation that persists, in now the twin

lattice, must be transmuted according to the twin shear [52, 67-71]. A first inspection

based on the correspondence matrix rule (CMR) [72] yields a transmutation of the basal

and pyramidal Taylor axes $\langle d \rangle$, to either $\langle a \rangle$, $(\langle a \rangle + \langle d \rangle)/2$, or $\langle d \rangle + \langle a \rangle/2$, which,

strikingly, yield to the RE-texture observed in the IPF plots. It should be noted that several combination of rotations may yield such a net rotation, and the one discussed here is an ideal one. Hence, this mechanism is not further developed in this paper.

In general, the spread around the RE-texture fiber could be attributed to the starting orientation positions of the parent grains within the $\langle 10\bar{1}0 \rangle$ fiber. The inset in Figure 3.5b illustrates the initial and final positions of two parent grains and their respective DRX grains in the IPF (indicated by red arrows in Figure 3.5b). While both parent grains lie within the RE-texture fiber, the difference remain unclear. However, based on the aforementioned Taylor analyses, it is very plausible that all of basal, prismatic, and pyramidal dislocations contribute at the same time to the rotation of the nucleus lattice, only for the amount of absorbed dislocations by the GBs to tally the difference.

It is important to realize that our EBSD inspections in the slowly recrystallized alloys suggest that the contour of RE-texture intensities, measured by XRD, are not dictated by the number fraction of corresponding grain orientations. There is in fact a very significant number of grains with orientations substantially deviated from that fiber, but they remain rather small (Figure 3.5b). Grains closely approaching the center of the RE-texture contours are usually bigger in size. In general, the size of DRX grains scales inversely with the distance from that fiber center. We examine this tendency further in samples extruded with higher speeds. In general, RE-texture occurs between $\langle 11\bar{2}1 \rangle \, ||ED$ and $\langle 11\bar{2}2 \rangle \, ||ED$ texture components, which is consistent with published literature [25]. Away from the RE-texture components, the IPF maps in Figures 3.10 highlight some of the DRX grains with orientations falling close to the $\langle 11\bar{2}3 \rangle \, ||ED$ texture component

identified by XRD-measured IPFs of Alloys A and B (Figure 3.1). This texture would simply arise from a more significant rotation around $\langle 10\bar{1}0 \rangle$ in the aforementioned two-stage rotation, suggesting higher local activity of basal/$\langle c + a \rangle$ dislocations in some grains [73]. In most cases, these grains correspond to a rotation angle of approximately ~58° around $\langle 10\bar{1}0 \rangle$.

3.3.2.2.5   Shear-banding induced DRX

Shear bands oblique to the extrusion direction were captured in Alloy C and reported in the IPF maps of Figure 3.12. We were not able to capture them prior to the development of DRX grains, which is because of the relatively faster DRX kinetics in this alloy.
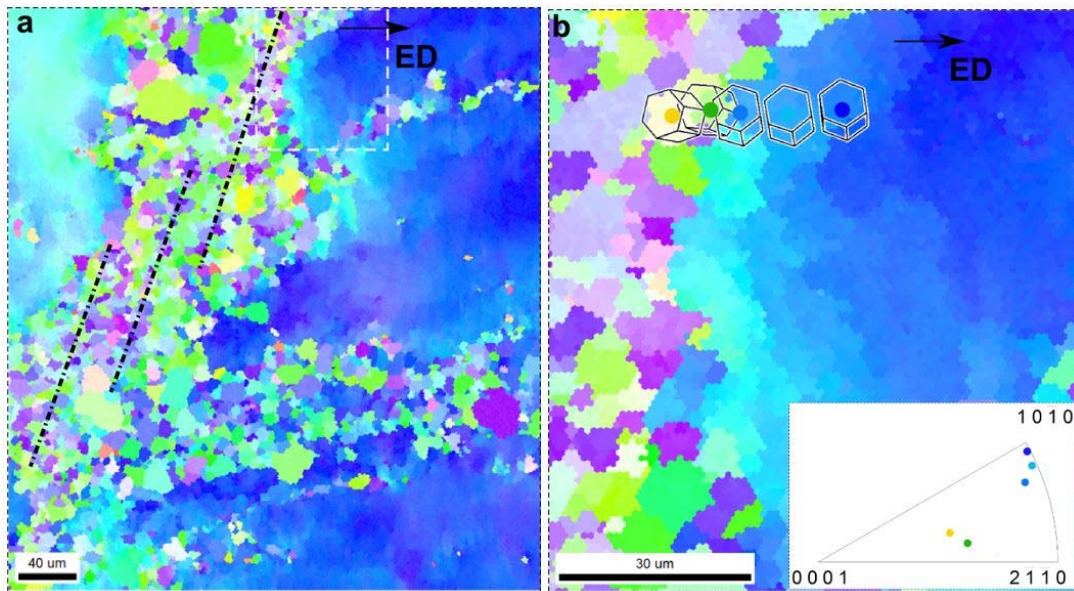
Figure 3.12   Electron backscattered diffraction analyses showing inverse pole figure ED maps of a region in Alloy C.

Extruded at 450 ºC under 10 mm/min ram speed, undergoing (a) continuous dynamic recrystallization at the vicinity of the shear bands and (b) leading to orientations falling close to the RE-texture.

102

Gradual rotations across the shear band borders around [0001] axis were omnipresent, and thus indicate that these shear bands were responsible for all recrystallization events that consumed them. Similar to previous observation, there are significant rotations observed inside the shear bands [74]. Few of the extruded billets showed noticeable traces of shear banding, and most DRX occurred within the GB protrusions.

3.3.3   Grain growth

The objective of post-deformation annealing was to examine if there is any competition between different orientations during grain growth that would lead to a certain growth preference affecting the final texture. Additionally, static annealing provides the partially recrystallized extrudates with sufficient diffusion time for texture modification potential to be assessed. The heat treatments began with isothermal soaking at 450 ºC for either 20 min or 180 min, and ended by water quenching. After 20 min of annealing, no discernable grain growth was noticed in the slowly recrystallizing Alloys A and B. However, rapidly recrystallizing Alloys C and D began grain growth stages while the nucleation stage was not saturated, and their microstructure was still partially recrystallized (Figure 3.13). IPF plots of three different major grain size ranges reveal similar, weak textures for all detectable ranges, indicating that no growth preferences occur during early stages of static recrystallization (Figure 3.13).

After 180 min of annealing at 450 ºC, grain growth is expected to occur with differences in grain growth behavior. It reveals that alloys could not all preserve/grow the nucleated RE grains during static recrystallization (Figure 3.14). Alloy A with higher content of Zn and no MM strengthen the $\langle 10\bar{1}0 \rangle$ fiber with negligible amount of RE-

oriented grains after annealing. The RE-textured grains ended up vanishing, as the amounts of MM was too low to sufficiently bring down the energy contrast level between GBs.
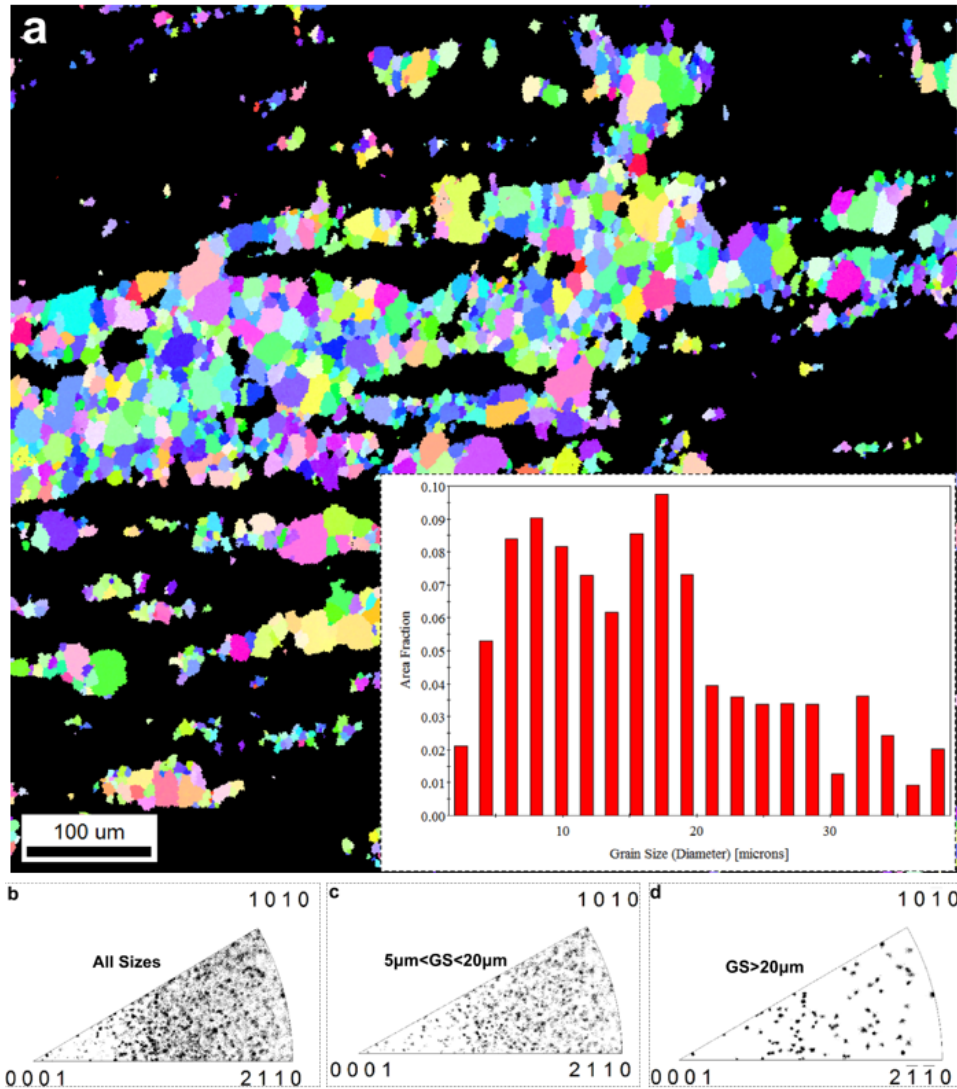
Figure 3.13   Electron backscattered diffraction with (a) inverse pole figure ED map and grain size distribution of the recrystallized portion of the microstructure of Alloy D.

Extruded at 450 ºC with ram speed of 10 mm/min, and post annealed at 450 ºC for 20 min. Grain sizes have been partitioned into three ranges and their respective textures are plotted in the inverse pole figures of (b-d).

104

Hence, they disappeared during grain growth although they were present in the dynamically recrystallized microstructure resulting from high extrusion velocities (Figure 3.14a). It is worth noting that slow recrystallization kinetics of alloy A and alloy B suppressed static recrystallization at a temperature as high as 450 ºC. Figure 3.14b shows that Alloy B with MM was able to retain only small number of the RE-oriented grains, though it displayed stronger fiber texture. The high portion of GBs with misorientation angles less than 5 º is due to the formation of subgrains during static recrystallization, as these alloys failed to express static grain growth (Figures 3.14b). Moreover, we tried eliminating misorientation values smaller than 10 º to better observe the misorientation distribution of high angle boundaries. However, the misorientation profiles appeared to express nearly the same distribution.

Alloy C, with high nucleation rate and a strong RE-texture after extrusion, showed substantial grain growth, but the RE-textured grains nearly completely vanished after static recrystallization (Figure 3.14c). The only composition that fully met the requirements of fast nucleation rates and optimum Zn, Y and REE additions for isotropic grain growth was Alloy D, and therefore, it developed a fairly weak texture (Max intensity of 2.3 m.r.d) after annealing (Figure 3.14d). This is a proof that MM-additions promote RE-texture persistence. The broader distribution of misorientation angles in Alloy D after static recrystallization could be ascribed to a more isotropic grain growth process, which may be explained by a GB co-segregation effect that decreases the anisotropy in GB energy and mobility (Figure 3.6). The homogeneous spectrum of misorientation angles indicate that the lower Zn and high MM contents allowed all type of GBs to compete favorably with each other even during grain growth despite its high

kinetics. Al-Samman *et al.* [47] observed that their MM-containing alloy developed the most uniform misorientation distribution. Their results agree well with the more uniform misorientation distribution shown by Alloy D in the near fully recrystallized state in Figure 3.14d.
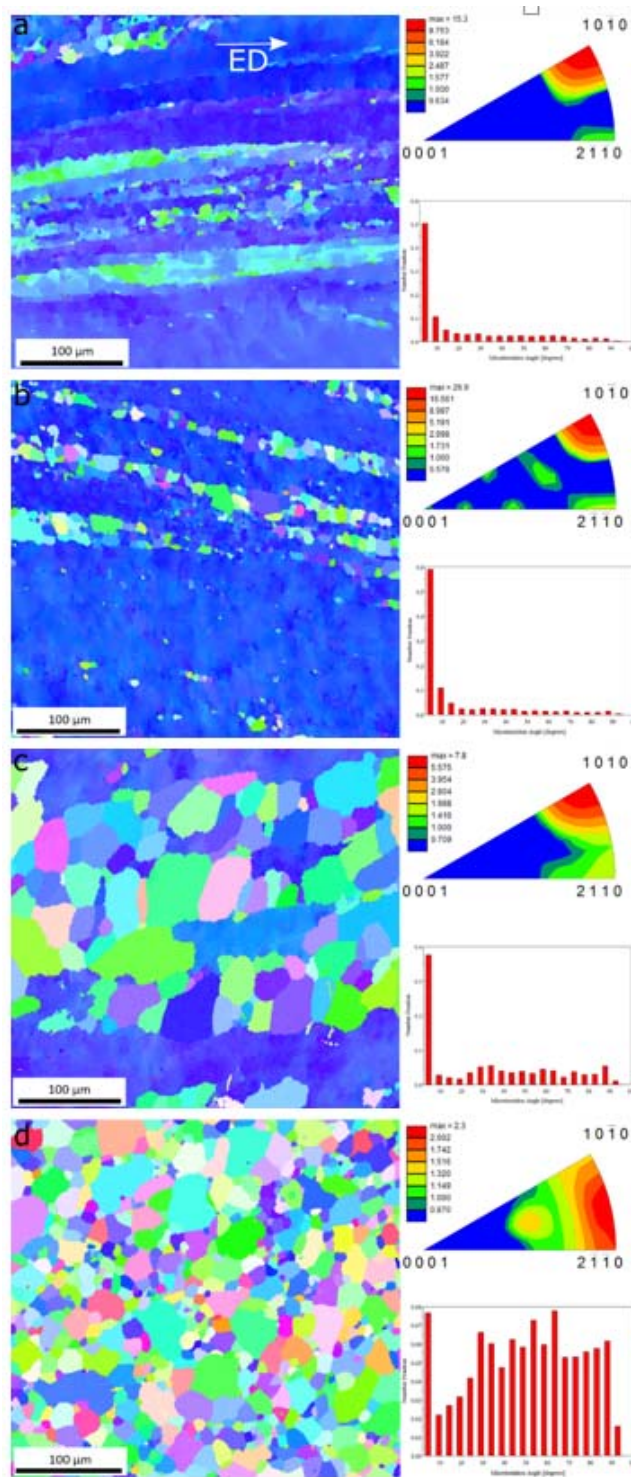
Figure 3.14   Electron backscattered diffraction analyses of annealed extrudates.

Showing inverse pole figure ED maps and their corresponding misorientation angle distribution and IPFs, taken from typical regions of (a) Alloy A, (b) Alloy B, (c) Alloy C, and (d) Alloy D after at 450 ºC – 10 mm/min extrusion and 450 ºC – 3 h annealing.

A stark comparison between the texture of high speed extrusion and low speed extrusion followed by annealing, particularly for Alloy D, reveals the key influence of grain growth on texture modification (compare Figure 3.1 and 3.14) [75]. Either dynamic or static grain growth, in the presence of optimum RE and Zn addition, favor texture weakening in similar manners. In fact, regardless of the state of grain growth, it is the driving force for grain growth that is essential. For instance, slowly extruded Alloy D with strong fiber texture (Figure 3.1d) displayed the weakest texture intensity after it was fully recrystallized (Figure 3.14d). Additionally, high speed extrusion yielded more driving force for dynamic grain growth, which resulted in significant texture weakening as well (Figure 3.14d). Therefore, this observation substantiates the fact that texture modification through RE addition would not be effective unless the driving force for growth is supplied. In other words, homogeneous grain growth seems to be essential, in terms of texture modification, for the effectiveness of RE-driven randomly nucleated grains.

Hence, when designing RE-containing Mg alloys, one must predict final texture of the product based on the mutual interaction of all alloying elements, Zn and RE in particular. REEs are needed for triggering new texture components, but if accompanied by relatively higher amount of Zn and Y, they can also slow down the kinetics of dynamic recrystallization through co-segregation to grain boundaries [48], thus sharpening the texture by preserving the deformed parent grains in the microstructure (e.g. Alloy B). Moreover, one may thoroughly optimize processing variables (e.g. extrusion temperature, speed and area reduction ratio) to obtain the desired texture upon processing.

3.4 Conclusions

This paper has helped clarify the mechanisms responsible for the origin of the so-called "RE-texture" in RE-containing magnesium alloys.

1. The RE texture components correspond to orientations lying between $\langle 11\bar{2}1 \rangle \,||ED$ and $\langle 11\bar{2}2 \rangle \,||ED$ with a marked concentration close to $\langle 22\bar{4}3 \rangle \,||ED$.

2. The main nucleation sites of grains with these characteristic orientations of the RE texture correspond to grain boundary protrusions along grain boundaries between bands of deformed grains. Grain boundary bulging is shown to be the predominant RE texture nucleation mechanism. This mechanism is consistent with the widely reported mechanism of discontinuous dynamic recrystallization. Transmission electron microscopy in this work revealed particles at grain boundaries close to protrusions, which is reminiscent of particle pinning, and promotes strain induced boundary migration (SIBM).

3. EBSD of the new orientations that form within the protrusions show that they correspond to contributions from $\langle 10\bar{1}0 \rangle$ and $[0001]$ rotation axes in the same protruded region. This is consistent with a concomitant action of multiple slip modes.

4. Continuous dynamic recrystallization contributed to the formation and rotation of sub-grains inside the bands of deformed grains, which resulted in the thickening of the bands and texture sharpening.

5. While shear localization events were found to occur in these alloys, they were far from having a dominant effect on the overall texture, and in all relevant cases, bulging-induced discontinuous dynamic recrystallization remains the prevailing mechanism for texture modification.

6. After static recrystallization and grain growth, even more random textures are attained. According to recent work [65], this phenomenon is consistent with rare earth element segregation to grain boundaries, which could alter the effective grain boundary energy and mobility variations among grain boundary types. Future work should focus on further illuminating this important aspect of RE addition on the final texture in Mg alloys.

3.5 Acknowledgment

3.6 References

[1] A. Imandoust, C. Barrett, T. Al-Samman, K. Inal, H. El Kadiri, A review on the effect of rare-earth elements on texture evolution during processing of magnesium alloys, J. Mater. Sci. 52 (2017) 1-29.

[2] S.R. Agnew, P. Mehrotra, T.M. Lillo, G.M. Stoica, P.K. Liaw, Texture evolution of five wrought magnesium alloys during route A equal channel angular extrusion: Experiments and simulations, Acta Mater. 53 (2005) 3135-3146.

[3] S.R. Agnew, Ö. Duygulu, Plastic anisotropy and the role of non-basal slip in magnesium alloy AZ31B, Int. J. Plast. 21 (2005) 1161-1193.

[4] S.R. Agnew, J.A. Horton, T.M. Lillo, D.W. Brown, Enhanced ductility in strongly textured magnesium produced by equal channel angular processing, Scripta Mater. 50 (2004) 377-381.

[5] S.R. Agnew, C.N. Tomé, D.W. Brown, T.M. Holden, S.C. Vogel, Study of slip mechanisms in a magnesium alloy by neutron diffraction and modeling, Scripta Mater. 48 (2003) 1003-1008.

[6] M. Barnett, M. Nave, C. Bettles, Deformation microstructures and textures of some cold rolled Mg alloys, Mater. Sci. Eng. A 386 (2004) 205-211.

[7] J. Bohlen, S.B. Yi, J. Swiostek, D. Letzig, H.G. Brokmeier, K.U. Kainer, Microstructure and texture development during hydrostatic extrusion of magnesium alloy AZ31, Scripta Mater. 53 (2005) 259-264.

[8] J.A. del Valle, F. Carreño, O.A. Ruano, Influence of texture and grain size on work hardening and ductility in magnesium-based alloys processed by ECAP and rolling, Acta Mater. 54 (2006) 4247-4259.

[9] B. Mordike, T. Ebert, Magnesium: properties—applications—potential, Mater. Sci. Eng. A 302 (2001) 37-45.

[10] H. Watanabe, T. Mukai, K. Ishikawa, Effect of temperature of differential speed rolling on room temperature mechanical properties and texture in an AZ31 magnesium alloy, J. Mater. Process. Technol. 182 (2007) 644-647.

[11] S. Agnew, M. Yoo, C. Tome, Application of texture simulation to understanding mechanical behavior of Mg and solid solution alloys containing Li or Y, Acta Mater. 49 (2001) 4277-4289.

[12] I. Ulacia, N.V. Dudamell, F. Gálvez, S. Yi, M.T. Pérez-Prado, I. Hurtado, Mechanical behavior and microstructural evolution of a Mg AZ31 sheet at dynamic strain rates, Acta Mater. 58 (2010) 2988-2998.

[13] L.L. Chang, E.F. Shang, Y.N. Wang, X. Zhao, M. Qi, Texture and microstructure evolution in cold rolled AZ31 magnesium alloy, Mater. Charact. 60 (2009) 487-491.

[14] Y. Chino, K. Kimura, M. Mabuchi, Twinning behavior and deformation mechanisms of extruded AZ31 Mg alloy, Mater. Sci. Eng. A 486 (2008) 481-488.

[15] J.P. Hadorn, K. Hantzsche, S. Yi, J. Bohlen, D. Letzig, S.R. Agnew, Effects of Solute and Second-Phase Particles on the Texture of Nd-Containing Mg Alloys, Metall. Mater. Trans. A 43 (2012) 1363-1375.

[16] T. Al-Samman, G. Gottstein, Dynamic recrystallization during high temperature deformation of magnesium, Mater. Sci. Eng. A 490 (2008) 411-420.

[17] M.R. Barnett, Quenched and annealed microstructures of hot worked magnesium AZ31, Mater. Trans. 44 (2003) 571-577.

[18] J. Del Valle, O.A. Ruano, Influence of texture on dynamic recrystallization and deformation mechanisms in rolled or ECAPed AZ31 magnesium alloy, Mater. Sci. Eng. A 487 (2008) 473-480.

[19] S.M. Fatemi-Varzaneh, A. Zarei-Hanzaki, H. Beladi, Dynamic recrystallization in AZ31 magnesium alloy, Mater. Sci. Eng. A 456 (2007) 52-57.

[20] A. Galiyev, R. Kaibyshev, G. Gottstein, Correlation of plastic deformation and dynamic recrystallization in magnesium alloy ZK60, Acta Mater. 49 (2001) 1199-1207.

[21] O. Sitdikov, R. Kaibyshev, Dynamic Recrystallization in Pure Magnesium, Mater. Trans. 42 (2001) 1928-1937.

[22] P. Changizian, A. Zarei-Hanzaki, M. Ghambari, A. Imandoust, Flow localization during severe plastic deformation of AZ81 magnesium alloy: Micro-shear banding phenomenon, Mater. Sci. Eng. A 582 (2013) 8-14.

[23] S. Agnew, P. Mehrotra, T. Lillo, G. Stoica, P. Liaw, Texture evolution of five wrought magnesium alloys during route A equal channel angular extrusion: Experiments and simulations, Acta Mater. 53 (2005) 3135-3146.

[24] J. Bohlen, S. Yi, D. Letzig, K.U. Kainer, Effect of rare earth elements on the microstructure and texture development in magnesium–manganese alloys during extrusion, Mater. Sci. Eng. A 527 (2010) 7092-7098.

[25] N. Stanford, Micro-alloying Mg with Y, Ce, Gd and La for texture modification—A comparative study, Mater. Sci. Eng. A 527 (2010) 2669-2677.

[26] N. Stanford, M.R. Barnett, The origin of "rare earth" texture development in extruded Mg-based alloys and its effect on tensile ductility, Mater. Sci. Eng. A 496 (2008) 399-408.

[27] S. Sandlöbes, M. Friák, S. Zaefferer, A. Dick, S. Yi, D. Letzig, Z. Pei, L.F. Zhu, J. Neugebauer, D. Raabe, The relation between ductility and stacking fault energies in Mg and Mg–Y alloys, Acta Mater. 60 (2012) 3011-3021.

[28] S. Sandlöbes, S. Zaefferer, I. Schestakow, S. Yi, R. Gonzalez-Martinez, On the role of non-basal deformation mechanisms for the ductility of Mg and Mg–Y alloys, Acta Mater. 59 (2011) 429-439.

[29] S. Agnew, R. Mulay, F. Polesak, C. Calhoun, J. Bhattacharyya, B. Clausen, In situ neutron diffraction and polycrystal plasticity modeling of a Mg–Y–Nd–Zr alloy: effects of precipitation on individual deformation mechanisms, Acta Mater. 61 (2013) 3769-3780.

[30] K. Máthis, G. Csiszár, J. Čapek, J. Gubicza, B. Clausen, P. Lukáš, A. Vinogradov, S. Agnew, Effect of the loading mode on the evolution of the deformation mechanisms in randomly textured magnesium polycrystals–Comparison of experimental and modeling results, Int. J. Plast. 72 (2015) 127-150.

[31] J.P. Hadorn, R.P. Mulay, K. Hantzsche, S. Yi, J. Bohlen, D. Letzig, S.R. Agnew, Texture Weakening Effects in Ce-Containing Mg Alloys, Metall. Mater. Trans. A 44 (2012) 1566-1576.

[32] R.K. Mishra, A.K. Gupta, P.R. Rao, A.K. Sachdev, A.M. Kumar, A.A. Luo, Influence of cerium on the texture and ductility of magnesium extrusions, Scripta Mater. 59 (2008) 562-565.

[33] Y. Chino, M. Kado, M. Mabuchi, Enhancement of tensile ductility and stretch formability of magnesium by addition of 0.2wt%(0.035at%)Ce, Mater. Sci. Eng. A 494 (2008) 343-349.

[34] K. Hantzsche, J. Bohlen, J. Wendt, K.U. Kainer, S.B. Yi, D. Letzig, Effect of rare earth additions on microstructure and texture development of magnesium alloy sheets, Scripta Mater. 63 (2010) 725-730.

[35] N. Stanford, D. Atwell, A. Beer, C. Davies, M.R. Barnett, Effect of microalloying with rare-earth elements on the texture of extruded magnesium-based alloys, Scripta Mater. 59 (2008) 772-775.

[36] E. Ball, P. Prangnell, Tensile-compressive yield asymmetries in high strength wrought magnesium alloys, Scripta Metallurgica et Materialia 31 (1994) 111-116.

[37] L. Mackenzie, B. Davis, F. Humphreys, G. Lorimer, The deformation, recrystallisation and texture of three magnesium alloy extrusions, Mater. Sci. Technol. 23 (2007) 1173-1180.

[38] T. Al-Samman, X. Li, Sheet texture modification in magnesium-based alloys by selective rare earth alloying, Mater. Sci. Eng. A 528 (2011) 3809-3822.

[39] J. Robson, D. Henry, B. Davis, Particle effects on recrystallization in magnesium–manganese alloys: particle-stimulated nucleation, Acta Mater. 57 (2009) 2739-2747.

[40] J.P. Hadorn, K. Hantzsche, S. Yi, J. Bohlen, D. Letzig, J.A. Wollmershauser, S.R. Agnew, Role of Solute in the Texture Modification During Hot Deformation of Mg-Rare Earth Alloys, Metall. Mater. Trans. A 43 (2011) 1347-1362.

[41] J. Hadorn, T. Sasaki, T. Nakata, T. Ohkubo, S. Kamado, K. Hono, Solute clustering and grain boundary segregation in extruded dilute Mg–Gd alloys, Scripta Mater. 93 (2014) 28-31.

[42] J.F. Nie, K. Oh-ishi, X. Gao, K. Hono, Solute segregation and precipitation in a creep-resistant Mg–Gd–Zn alloy, Acta Mater. 56 (2008) 6061-6076.

[43] R. Cottam, J. Robson, G. Lorimer, B. Davis, Dynamic recrystallization of Mg and Mg–Y alloys: Crystallographic texture development, Mater. Sci. Eng. A 485 (2008) 375-382.

[44] J. Nie, Y. Zhu, J. Liu, X.-Y. Fang, Periodic segregation of solute atoms in fully coherent twin boundaries, Science 340 (2013) 957-960.

[45] L. Mackenzie, M. Pekguleryuz, The recrystallization and texture of magnesium–zinc–cerium alloys, Scripta Mater. 59 (2008) 665-668.

[46] M. Steiner, J. Bhattacharyya, S. Agnew, The origin and enhancement of texture during heat treatment of rolled AZ31B magnesium alloys, Acta Mater. 95 (2015) 443-455.

[47] T. Al-Samman, X. Li, Sheet texture modification in magnesium-based alloys by selective rare earth alloying, Mater. Sci. Eng. A 528 (2011) 3809-3822.

[48] Z.R. Zeng, Y.M. Zhu, S.W. Xu, M.Z. Bian, C.H.J. Davies, N. Birbilis, J.F. Nie, Texture evolution during static recrystallization of cold-rolled magnesium alloys, Acta Mater. 105 (2016) 479-494.

[49] G. Song, Recent progress in corrosion and protection of magnesium alloys, Adv. Eng. Mater. 7 (2005) 563-586.

[50] R. Hielscher, H. Schaeben, A novel pole figure inversion method: specification of the MTEX algorithm, J. Appl. Crystallogr. 41 (2008) 1024-1037.

[51] C.D. Barrett, A. Imandoust, A.L. Oppedal, K. Inal, M.A. Tschopp, H. El Kadiri, Effect of Grain Boundaries on Texture Formation during Dynamic Recrystallization of Magnesium Alloys, Acta Mater. (2017).

[52] C.D. Barrett, H. El Kadiri, The roles of grain boundary dislocations and disclinations in the nucleation of {10 2} twinning, Acta Mater. 63 (2014) 1-15.

[53] A. Rollett, F. Humphreys, G.S. Rohrer, M. Hatherly. Recrystallization and related annealing phenomena, Elsevier, 2004.

[54] J. Wang, I.J. Beyerlein, Atomic Structures of $$ [0\bar{1}10] $$ Symmetric Tilt Grain Boundaries in Hexagonal Close-Packed (hcp) Crystals, Metall. Mater. Trans. A 43 (2012) 3556-3569.

[55] G. Bruggeman, G. Bishop, W. Hartt. Coincidence and near-coincidence grain boundaries in hcp metals. The Nature and Behavior of Grain Boundaries. Springer, 1972. pp. 83-122.

[56] Z.R. Zeng, M.Z. Bian, S.W. Xu, C.H.J. Davies, N. Birbilis, J.F. Nie, Texture evolution during cold rolling of dilute Mg alloys, Scripta Mater. 108 (2015) 6-10.

[57] G.B. Stephenson, Deformation during interdiffusion, Acta Metall. 36 (1988) 2663-2683.

[58] A. Inoue, Y. Kawamura, M. Matsushita, K. Hayashi, J. Koike, Novel hexagonal structure and ultrahigh strength of magnesium solid solution in the Mg–Zn–Y system, J. Mater. Res. 16 (2001) 1894-1900.

[59] L. Li, Deformation band and texture of a cast Mg–RE alloy under uniaxial hot compression, Mater. Sci. Eng. A 528 (2011) 7178-7185.

[60] L. Li, Micro structure and texture evolution during super plastic deformation of Mg–Re extruded alloy, J. Alloys Compd. 555 (2013) 255-262.

[61] Z.X. HE SM, L. PENG, X. GAO, J. NIE, W. DING, Precipitation in a Mg-10Gd-3Y-0.4 Zr (wt.%) alloy during isothermal ageing at 250℃, J. Alloys Compd. 421 (2006) 309-313.

[62] J.P. Hirth, R.C. Pond, J. Lothe, Disconnections in tilt walls, Acta Mater. 54 (2006) 4237-4245.

[63] Y.B. Chun, M. Battaini, C.H.J. Davies, S.K. Hwang, Distribution Characteristics of In-Grain Misorientation Axes in Cold-Rolled Commercially Pure Titanium and Their Correlation with Active Slip Modes, Metall. Mater. Trans. A 41 (2010) 3473-3487.

[64] C.D. Barrett, A. Imandoust, A.L. Oppedal, K.A. Inal, S.R. Agnew, H. El Kadiri, Effect of Grain Boundaries on Texture Formation during Dynamic Recrystallization of Mg Alloys, Acta Mater. Under Review.

[65] C.D. Barrett, A. Imandoust, A.L. Oppedal, K. Inal, M.A. Tschopp, H. El Kadiri, Effect of grain boundaries on texture formation during dynamic recrystallization of magnesium alloys, Acta Mater. 128 (2017) 270-283.

[66] C.D. Barrett, A. Imandoust, H. El Kadiri, Homogenization of grain boundary energy in magnesium by yttrium segregation, Scripta Mater. Under Review.

[67] C. Barrett, H. El Kadiri, M. Tschopp, Breakdown of the Schmid law in homogeneous and heterogeneous nucleation events of slip and twinning in magnesium, J. Mech. Phys. Solids 60 (2012) 2084-2099.

[68] H. El Kadiri, C.D. Barrett, J. Wang, C.N. Tomé, Why are twins profuse in magnesium?, Acta Mater. 85 (2015) 354-361.

[69] H. El Kadiri, J. Kapil, A. Oppedal, L. Hector, S.R. Agnew, M. Cherkaoui, S. Vogel, The effect of twin–twin interactions on the nucleation and propagation of twinning in magnesium, Acta Mater. 61 (2013) 3549-3563.

[70] J. Jordon, H. Brown, H. El Kadiri, H. Kistler, R. Lett, J. Baird, A. Luo, Investigation of fatigue anisotropy in an extruded magnesium alloy, Int. J. Fatigue 51 (2013) 8-14.

[71] A. Oppedal, H. El Kadiri, C. Tomé, S.C. Vogel, M. Horstemeyer, Anisotropy in hexagonal close-packed structures: improvements to crystal plasticity approaches applied to magnesium alloy, Philosophical Magazine 93 (2013) 4311-4330.

[72] M. Niewczas, Lattice correspondence during twinning in hexagonal close-packed crystals, Acta Mater. 58 (2010) 5848-5857.

[73] L. Toth, P. Gilormini, J. Jonas, Effect of rate sensitivity on the stability of torsion textures, Acta Metall. 36 (1988) 3077-3091.

[74] I. Basu, T. Al-Samman, G. Gottstein, Shear band-related recrystallization and grain growth in two rolled magnesium-rare earth alloys, Mater. Sci. Eng. A 579 (2013) 50-56.

[75] J.W. Senn, S.R. Agnew, Texture randomization of magnesium alloys containing rare earth elements, Proceedings of Magnesium Technology 2008 (2008) 153-158.

CHAPTER IV

NUCLEATION AND PREFERENTIAL GROWTH MECHANISM OF

RECRYSTALLIZATION TEXTURE IN BINARY MAGNESIUM-

RARE EARTH ALLOYS

4.1 Introduction

Over the past two decades, industries have shown an ever increasing demand for

low density alloys, spurring a strong interest in magnesium (Mg) [1-8]. Despite its

favorable specific strength, poor low temperature formability has dramatically restricted

the wide use of wrought magnesium alloys in critical safety components [9]. This

inadequacy is directly associated with the limited number of active slip systems in

directions other than those contained in the basal plane of the hexagonal close packed

(HCP) structure [10-16]. Moreover, rolling and extrusion systematically lead to very

sharp textures, intensifying strain-path anisotropy, asymmetry and damage propensity

[17-20]. For instance, a typical $\langle 10\bar{1}0\rangle$ fiber texture develops during the extrusion

process, which may transform to $\langle 10\bar{1}0\rangle - \langle 11\bar{2}0\rangle$ fiber [21]. This type of texture

evolution aligns the basal planes parallel to extrusion direction (ED) [10]. A $\langle 10\bar{1}0\rangle||ED$

texture is subject to strong plastic anisotropy as compressive deformation along the ED

activates profuse $\{10\bar{1}2\}$ twinning, while tension along ED would hardly cause any

twinning of the same type. Usually, strong slip-twin interactions take place at the twin

boundaries leading to hot stress spot and acceleration of damage [12].

In contrast to traditional Mg alloys such as AZ31B, rare earth (RE) element containing Mg alloys express ameliorated formability [19, 21-24]. RE addition activates non-basal dislocations (e.g. $\langle c + a \rangle$ dislocations) at low temperatures, which mitigates the need of twinning and thus improves ductility. This has been attributed to an effect that tends to decrease the difference in the critical resolved shear stress (CRSS) values of the available slip systems [5, 25-27]. Moreover, RE elements tend to decrease the energy of the I_1 stacking fault (ISF_1), which serves as a nucleation site for $\langle c + a \rangle$ dislocations [27, 28]. However, although RE addition offers the prospect of improved mechanical properties, understanding of the mechanisms by which they can enhance ductility is still lagging. Moreover, the expense of RE elements means that only very small concentrations of them can be present in cost-effective alloys, and such alloys have not met yet ductility requirements in critical safety components. Therefore, a more rigorous understanding of the effect of RE elements on dynamic recrystallization is critical to improve their texture modification action.

Alloying with RE elements weakens the tendency of magnesium to retain a sharp texture during recrystallization [22, 29-31]. This tendency is prevalent for both single RE element additions and cheaper RE alloy additions such as Mischmetal (MM) [32-34]. Hantzsche *et al.* [35] found that binary Mg-RE alloys with concentrations above the threshold limit intrinsic to each RE element (e.g. Ce and Nd) develop weaker texture intensities during rolling, while more dilute alloys retained their sharp basal texture that is typical of conventional Mg alloys [8]. In other words, a sudden drop from a strong basal texture to weak texture intensities was observed as the RE concentration exceeded a threshold limit [35]. A number of authors correlated the threshold limits to solubility

118

limits [35]. However, for all the elements they studied, texture modification started off well below the solubility limit, which rules out precipitate formation as the cause of this correlation [9]. Stanford [23] also found small concentrations are required to induce RE texture. For example, only 400 ppm of Ce is required for texture modification in pure magnesium. On the other hand, Robson *et al.* [36] pointed out the variation of dominant texture components with extrusion condition in a Mg-RE alloy. In a recent study by the present authors [37], extrusion speed was a crucial factor in developing RE texture, as the driving force for dynamic recrystallization (DRX) is in fact stored strain energy. Therefore, one can perceivably question the dependence of the RE threshold limit on extrusion condition. Is defining an absolute value as a threshold concentration for texture modification realistic? The first aim of the present study is to explore the combined effect of RE concentration and extrusion condition on texture evolutions in binary Mg-RE alloys.

Several approaches have been exploited to understand the mechanisms underlying texture modification associated with RE addition [24, 31, 32, 34, 38, 39]. Although particle stimulated nucleation (PSN) was believed to account for this phenomenon [40], further studies demonstrated texture weakening in solid solution Mg-RE alloys, indicating that the role of PSN is not necessary [32-34]. Stanford and Barnett [24] observed shear band formation in extruded Mg-RE alloys, within which DRX grains had "RE texture" orientation (i.e. $\langle 11\bar{2}1 \rangle || ED$). However, shear band formation and consequent texture alterations have been reported in traditional Mg alloys [3]. Furthermore, RE texture formation was reported in Mg-RE alloys with no shear banding events, which questioned its necessity as a mechanism for texture modification [33, 34].

Deformation twinning has also been observed to serve as DRX nucleation sites for randomly oriented grains, as RE additions bolster contraction and secondary twin formation [35, 41]. Nevertheless, the effectiveness of such nuclei in terms of grain growth, and hence texture modification, are limited by twin boundaries [42]. In a recent study by the present authors, boundaries with tilt character between bands of deformed grains were suggested to be the main contributor for widespread DRX nucleation [37]. Stanford [23] suggested that a strong interaction of solute atoms with dislocations and grain boundaries may account for the remarkable influence of RE elements on the recrystallization texture of Mg-RE alloys. Employing intragranular misorientation axis (IGMA) analysis, Hadorn *et al*. [34] determined that the population of geometrically necessary dislocations (GNDs) shifts from a predominantly basal $\langle a \rangle$ type to non-basal $\langle a \rangle$ type dislocations by increasing the RE content [33]. Therefore, a change in recrystallization mechanism was envisaged. They also reported a significant segregation of yttrium (Y) to grain boundaries. Segregation of RE elements to grain boundaries and dislocation cores suppress recrystallization kinetics [29, 34]. This can potentially diversify crystal orientations of grain nuclei by boosting the available time period for basal and non-basal dislocations to migrate into DRX nuclei and induce random crystal rotations. However, these mechanisms are yet to be demonstrated and described in detail. The second goal of this study is to directly observe the occurrence of such phenomenon and to explicate formation of random nuclei in binary Mg-RE alloys.

It is well understood that growth of grains with new orientations, following DRX nucleation, is essential for modification of recrystallization texture [43-44]. The growth advantage of $[0001]||ND$ grains (i.e. c-axis nearly normal to rolling direction) in rolled

sheets of traditional Mg alloys retains strong basal texture upon recrystallization [45]. A similar tendency for retaining a sharp fiber texture was observed in extruded products [46-49]. RE addition ought to suppress/alter the preferential growth over the course of static or dynamic recrystallization [9, 33,44]. In a recent study, the present authors found that Mg-RE alloys with randomized texture possess a broader range of misorientation distribution, which imparts the grains with nearly equal chance for growth [37]. Barrett *et al.* [50] showed that addition of Y to Mg reduces the gap between energy cusps in the excess potential energy plot for c-axis tilt boundaries, which they hypothesized would eliminate the preference to nucleate special boundaries, instead stabilizing grains with a wide variety of orientations and giving them nearly equal opportunity for growth. This may rationalize the isotropic growth of DRX nuclei in Mg-RE alloys. However, isotropic grain boundary mobility can only partially solve the preferential growth puzzle, as the growth behavior in Mg-RE alloys seems to act rather selectively. Barrett *et al.* [51] also found that high mobility of $\{13\bar{4}0\}$ twin boundary was accountable for the formation of $\langle 11\bar{2}0 \rangle || ED$ fiber in AM30 Mg alloy during dynamic recrystallization. However, for the case of Mg-RE alloys, one can perceive the existence of all types of grain boundaries due to the diversity of nuclei orientation. Hence, there must be another factor influencing the growth behavior in the presence of RE elements. Does this factor pertain to a geometrical effect operating during thermo-mechanical processing? This question is key to uncover RE effect on texture modification and would constitute our third and last goal in this paper.

In order to address the abovementioned questions, we use extensive and fine electron back scattered diffraction (EBSD) characterization. The reasonability of defining

121

a threshold limit for two RE elements (Ce and Gd) was examined through four extrusion conditions. Additionally, different processing parameters and RE concentrations allowed us to observe microstructural and texture evolutions through the entire restoration phenomena. Nucleation and growth of new orientations was elucidated fastidiously and step-by-step. Schmid factor analysis explains the geometrical effect behind the preferred growth of RE texture.

4.2   Experimental Procedure

We selected Ce and Gd as poorly and highly soluble RE elements, respectively, to represent two extremes of a spectrum of RE texture modification characteristics. We designed the chemical composition of investigated binary alloys based on the available data in the literature [23, 34, 35]. Three concentrations were considered for each RE element, all of which were above the reported threshold limits. We aimed to track the minute details of texture evolution from the initiation point in dilute alloys to the saturation point in alloys relatively rich with RE elements. High purity magnesium was also cast as bench mark. The concentration of RE elements are listed in Table 1. The designed binary alloys were cast using 99.99999% pure magnesium and the 99.999% pure rare earth elements in a vacuum induction melt furnace using a tantalum crucible at AMES Laboratory. The as-cast billets were solution treated at 450 ºC for 10 h under flowing argon gas atmosphere followed by immediate water quenching. After annealing, the chemical compositions were analyzed using atomic emission spectroscopy (ICP-AES) method. Solution treated alloys were machined to cylindrical specimens ~32 mm (1.25 in) in diameter and ~25 mm (1 in) long cylinders and were subject to indirect

extrusion at ram speeds of 10 mm/min and 40 mm/min at 450 ºC with extrusion ratios of 1:6 and 1:25 followed by air cooling.

Table 4.1   Chemical composition of binary Mg-RE alloys in wt. % measured by ICP-AES method

Alloy	Concentration (wt. %)	
	Ce	Gd
Mg	-	-
Mg- 0.23 Ce	0.23	-
Mg- 0.40 Ce	0.40	-
Mg- 0.52 Ce	0.52	-
Mg- 0.38 Gd	-	0.38
Mg- 0.96 Gd	-	0.96
Mg- 2.51 Gd	-	2.51

Samples were cut along the radial direction to examine the microstructural and texture evolutions on the plane normal to extrusion radial direction (ERD). The extrusion radial direction is a radial direction of the cylinder that is normal to ED.

The samples were extracted from the center of the extrudates in the steady state region (i.e. not from the beginning or end of the extrudate), and were prepared by standard metallographic techniques and polished using 0.06 μm colloidal silica (Struers OPS) for 10 minutes. In preparation for electron back scattered diffraction (EBSD) technique, Electro-polishing using a Struers LectroPol-5 was conducted on polished samples in chilled (-5 ºC) Struers C1 electrolyte at 25 V for 120 s. Samples were sonicated for 20 minutes after preparation in absolute ethanol to remove artifacts from the surface. Texture measurements were conducted on transverse cross-sectional (plane normal to ERD) using EBSD. EBSD analyses were performed using a field emission scanning electron microscope (SEM, Zeiss Supra 40) at the operating voltage of 20 kV. Scanning step size was 1 μm for micro-texture measurements and 0.1 μm for ones used

for intragranular misorientation axes (IGMA) analysis. IGMA analysis was conducted to investigate the activity Taylor axes [34] corresponding to basal/$\langle c + a \rangle$ and prismatic slip. Grain orientation spread (GOS) charts were used to differentiate between deformed and recrystallized grains. We selected GOS values smaller than 2º to isolate DRX grains and explore their microstructural and textural characteristics. Inverse pole figures (IPF), all referring to extrusion direction, were obtained from EBSD. All the EBSD processing was performed employing EDAX-OIM Analysis 7 software.

4.3   Results and discussion

The results of our experiments in this work are presented through the following sections. The influence of extrusion conditions and the content of RE elements on the microstructure and texture evolution is elaborated in Section 3.3.1, while distinct sub-sections are dedicated for each element. Section 3.3.2 elucidates the roles of continuous and discontinuous recrystallization mechanisms in microstructure evolution and their texture modifying characteristics. The last section, Section 3.3.3, demonstrates a novel reasoning for preferential grain growth in binary alloys, enabling the RE texture to thrive.

4.3.1   Influence of rare earth concentration and extrusion condition

Although the formation of "RE texture" (i.e. $\langle 11\bar{2}1 \rangle || ED$) has been undisputed upon high temperature extrusion of binary RE containing Mg alloys [23, 24], capturing the "RE texture" phenomenon from its initiation stage to completion imposes a substantial characterization challenge. In an endeavor to stack the odds in favor of observing the details of this phenomenon, our approach was to vary the content of RE elements and extrusion conditions. This strategy was based on varying the potential for

124

texture modification and the driving force for dynamic recrystallization. Therefore, we selected high purity Mg as a benchmark, and chose three concentrations of RE elements (i.e. Ce and Gd) ranging from the texture modification threshold limit to higher concentrations wherein, reportedly, the texture intensity vs. concentration curve reaches to a plateau [33, 35]. The designed set of alloys along with pure Mg were then subject to four different levels of deformation stored energy by extrusion.

Figure 4.1 depicts the inverse pole figure (IPF) maps along with their IPFs of the pure Mg extruded with extrusion ratio of 1:6 and ram speeds of 10 and 40 mm/min. Due to similarity of the results, only one area reduction is addressed. As in traditional Mg alloys, $\langle 10\bar{1}0 \rangle - \langle 11\bar{2}0 \rangle$ fiber texture forms in both conditions, while increasing the extrusion speed intensifies the 30º misorientation peak (Figure 4.1b). A recent study by the present authors demonstrated that the extremely high mobility of a $28°/\{13\bar{4}0\}$ twin boundary between the parent and DRX grains in traditional Mg alloys accounts for the growth advantage of grains with $\langle 11\bar{2}0 \rangle||ED$ orientation [51]. However, addition of RE elements disrupts Mg's tendency for developing a sharp fiber texture.

4.3.1.1   Mg-Ce binary alloys

Figure 4.2 represents the IPFs of the extruded Mg-Ce binary alloys obtained from the recrystallized portion of EBSD scans. DRX grains were differentiated from deformed grains by selecting grain orientation spread (GOS) values smaller than 2º (see an example in Figure 4.3). Although the volume fraction of DRX grains were different from one extrusion condition to another, we compare the texture of only DRX grains to impartially measure their potential for "RE texture" development. Our results in Figure 4.2 demonstrated that "RE texture" formation essentially requires adequate deformation

stored energy combined with sufficient RE concentration. While the binary alloys have

Ce concentrations above the reported threshold limit for texture modification [23, 33],

samples extruded with 10 mm/min speed and 1:6 extrusion ratio fail to develop a

remarkable intensities of RE component in their corresponding IPFs, as the most dilute

alloy (Mg- 0.23 wt. %Ce) shows an arc spanning from $\langle 20\bar{2}3 \rangle$ to $\langle 11\bar{2}2 \rangle$.

Figure 4.1   Inverse pole figure (IPF) ED maps of pure Mg.
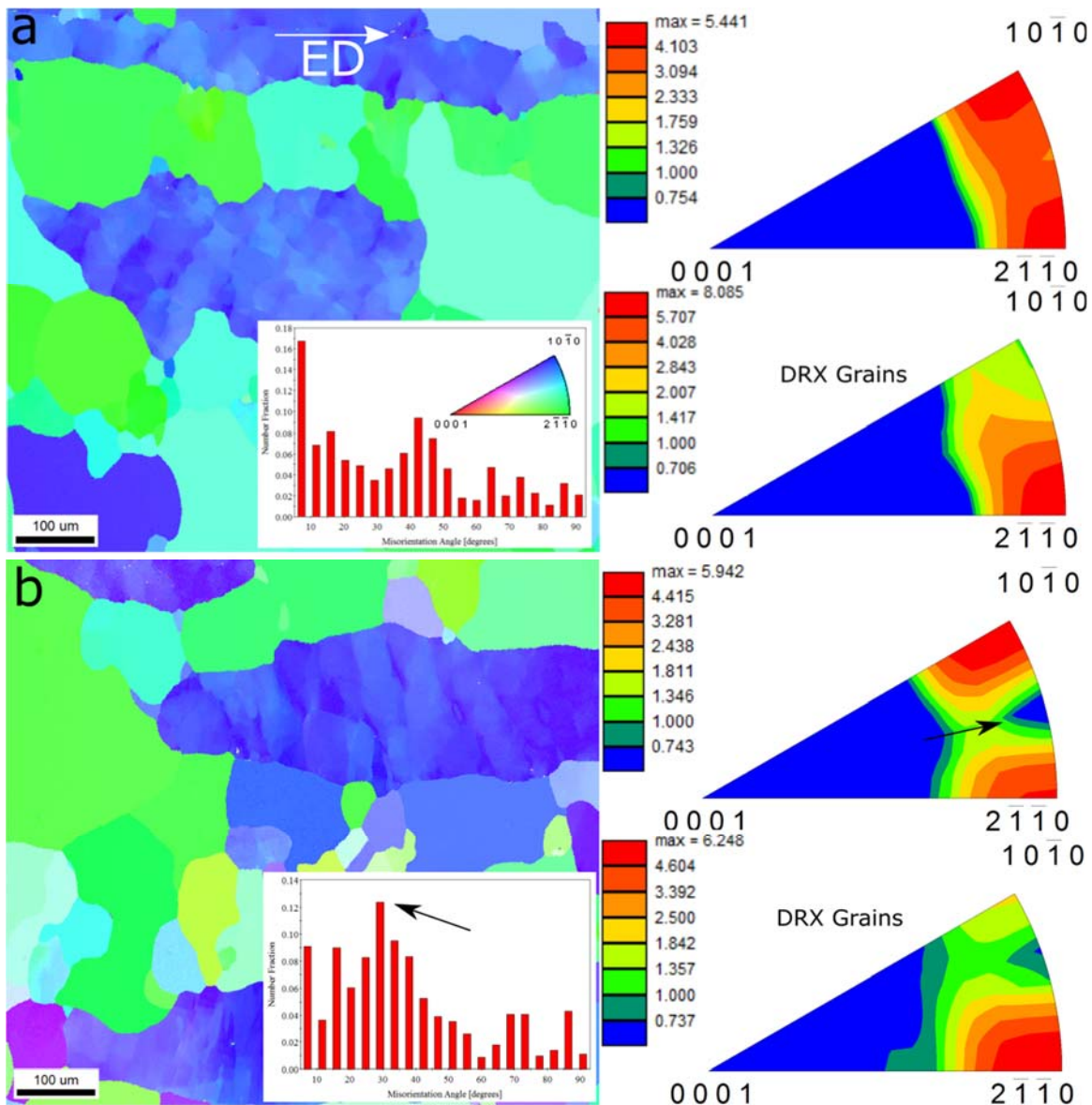
Along with their corresponding misorientation distribution, typical IPFs, and IPFs of recrystallized grains extruded at 450 ºC **a)** with 10 mm/min ram speed and 1:6 area reduction ratio, **b)** with 40 mm/min ram speed and 1:6 area reduction ratio. IPFs refer to extrusion direction. The IPF map legend in picture **a** applies to all of the IPF maps in this paper.
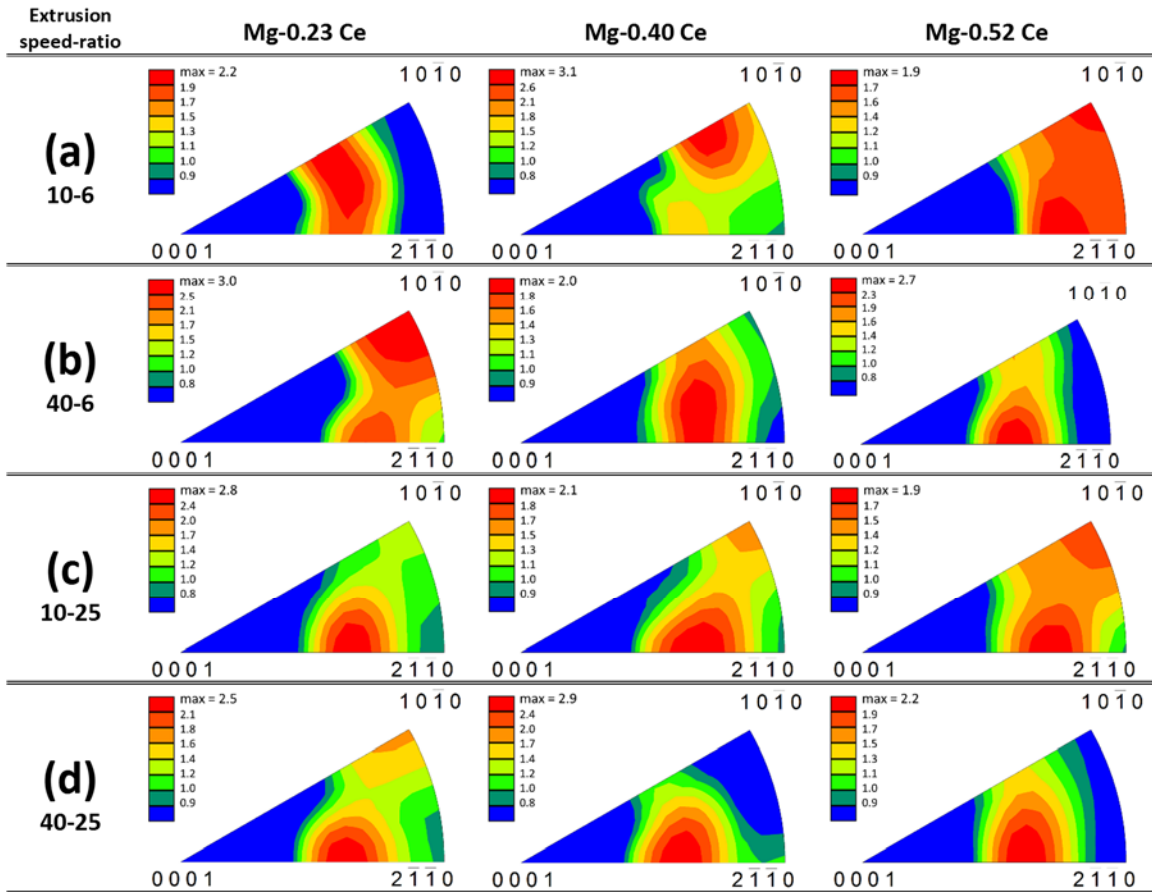
Figure 4.2 Inverse pole figures (IPF) of the recrystallized grains of the binary Mg-Ce alloys with 0.23, 0.4 and 0.52 wt. % Ce.

Extruded at 450 ºC **a)** with 10 mm/min ram speed and 1:6 area reduction ratio, **b)** with 40 mm/min ram speed and 1:6 area reduction ratio, **c)** with 10 mm/min ram speed and 1:25 area reduction ratio, **d)** with 40 mm/min ram speed and 1:25 area reduction ratio. IPFs refer to extrusion direction.

Whilst, in the same extrusion condition, alloys with higher concentrations of Ce (e.g. 0.40 and 0.52 wt. %) appear to be in the midst of a textural transition as they see their global bulk diffusion rate decreased by the higher content of Ce (Figure 4.2a). Hence, a threshold limit of RE concentration can only be defined with respect to a predesigned processing parameters.

128
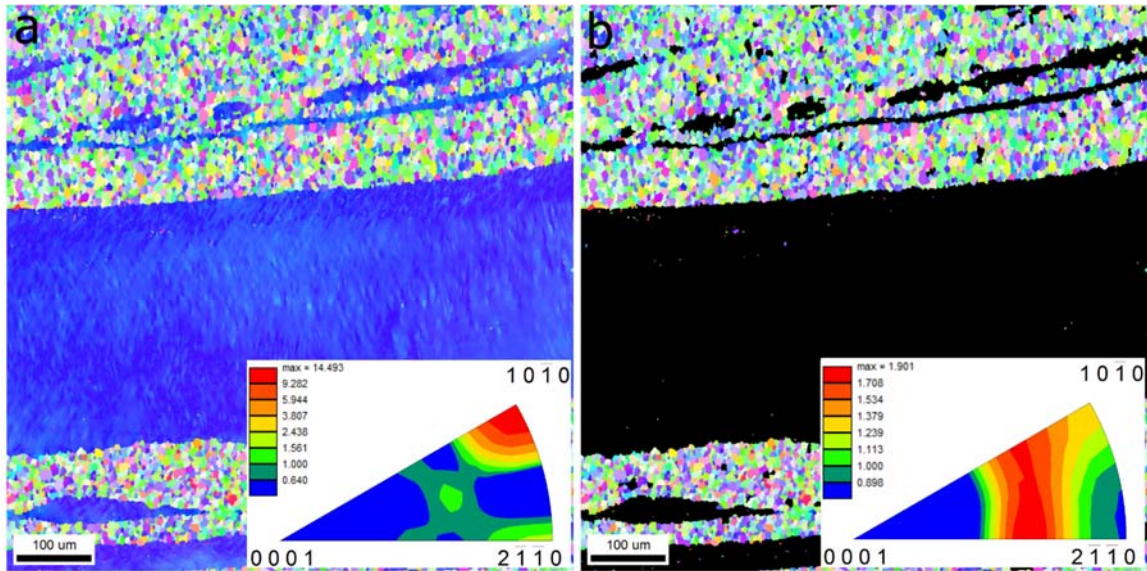
Figure 4.3   Inverse pole figure (IPF) ED maps of Mg- 2.51 wt. % Gd alloy along with their corresponding IPFs refering to extrusion direction.

Extruded at 450 ºC with 10 mm/min ram speed and 1:25 area reduction ratio; **a)** a typical EBSD scan, **b)** recrystallized grains differentiated from deformed grains by selecting grain orientation spread (GOS) values smaller than 2º.

Although increasing the ram speed to 40 mm/min provides more nucleation sites, due to the abundance of deformation stored energy, as a driving force for grain growth, it results in larger DRX grain size (Figure 4.4a). As a result, the intensity of RE component is bolstered up to a well-defined hot spot in the IPFs of Figure 4.2b. However, our observations indicate that the RE component does not have a specific orientation because it moves toward the [0001] pole for samples with higher Ce concentrations (Figure 4.2b). Assuming the orientation of DRX grains to be dependent upon the "backward rotation" induced by dislocation recovery, the position of RE texture on the IPF would be a function of dislocation population recovered through DRX. Depending on the Ce concentration and extrusion condition, the hot spot in the RE component in Mg-Ce alloys

seems to lie between $\langle 11\bar{2}1 \rangle$ and $\langle 11\bar{2}2 \rangle$. The details of such recovery induced rotations will be analyzed in Section 3.3.2.
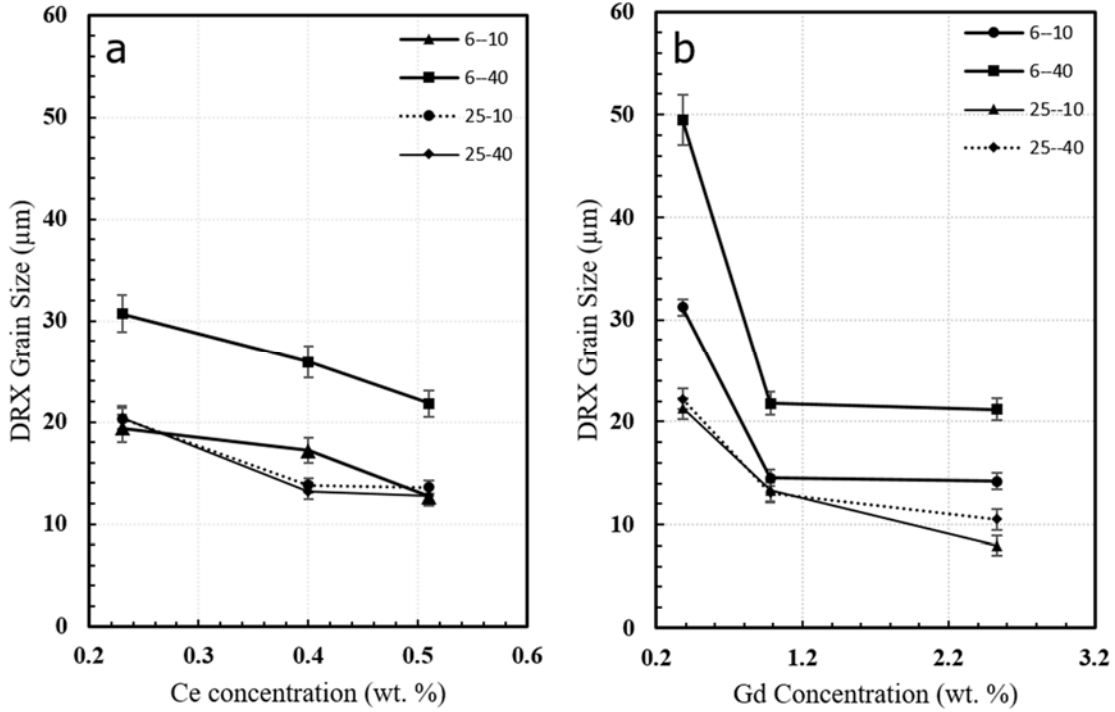
Figure 4.4   Typical plots displaying DRX grain size against RE concentration. For the designed extrusion conditions; **a)** Mg-Ce alloys, **b)** Mg-Gd alloys.

Interestingly, Figure 4.2a and c show that low ram speed extrusions failed to supply adequate driving force for transition of $\langle 10\bar{1}0 \rangle$ fiber to RE component, as the Ce rich alloys somehow preserved their $\langle 10\bar{1}0 \rangle$ fiber due to their slower dislocation dynamics [29]. In fact, the intensity of $\langle 10\bar{1}0 \rangle$ fiber increased by increasing Ce concentration for low ram speed extrusions (Figure 4.2a and c). On the other hand, the opposite trend was observed for high ram speed extrusions where higher Ce concentration was associated with weaker $\langle 10\bar{1}0 \rangle$ fiber intensities (Figure 4.2b and d).

Conducting extrusion with high ram speed and high area reduction ratio results in the texture evolution developing a strong RE fiber in the cost of $\langle 10\bar{1}0 \rangle$ fiber (Figure 4.4d). This observation suggests that higher concentrations of RE addition requires more deformation stored energy to boost dislocation motion, and vice versa.

4.3.1.2   Mg-Gd binary alloys

We observed the same grain size trend for extruded Mg-Gd alloys, where increasing ram speed generally led to larger average grain size (Figure 4.4). However, Gd-containing alloys had smaller grain size than Ce rich alloys. Figure 4.5 shows the IPFs of extruded Mg-Gd binary alloys acquired from the recrystallized portion of the EBSD scans. For the case of the most dilute Mg-Gd alloy (0.38 wt. %), regardless of area reduction ratio, low extrusion speed yields a fairly strong $\langle 10\bar{1}0 \rangle$ fiber texture for DRX grains (Figure 4.5a and c). Figure 4.6, as a representative, is an ED mapped IPF map of Mg-0.38 Gd alloy extruded with low speed and extrusion ratio. A stark comparison between the EBSD map and the image quality (IQ) map reveals the propensity of DRX grains to preserve their parent's texture. As a matter of fact, small concentration of Gd and imposed strain energy, as a combined factor, does not exceed the limit for texture modification of DRX grains. On the other hand, deploying higher extrusion speed for the most dilute alloy appears to be a quite efficient strategy for texture modification. In fact, higher strain stored energy triggers RE effects by enhancing the number of nucleation sites and boosting dynamic grain growth (Figure 4.5b and d). This observation also supports dependence of the RE threshold limit on processing condition.
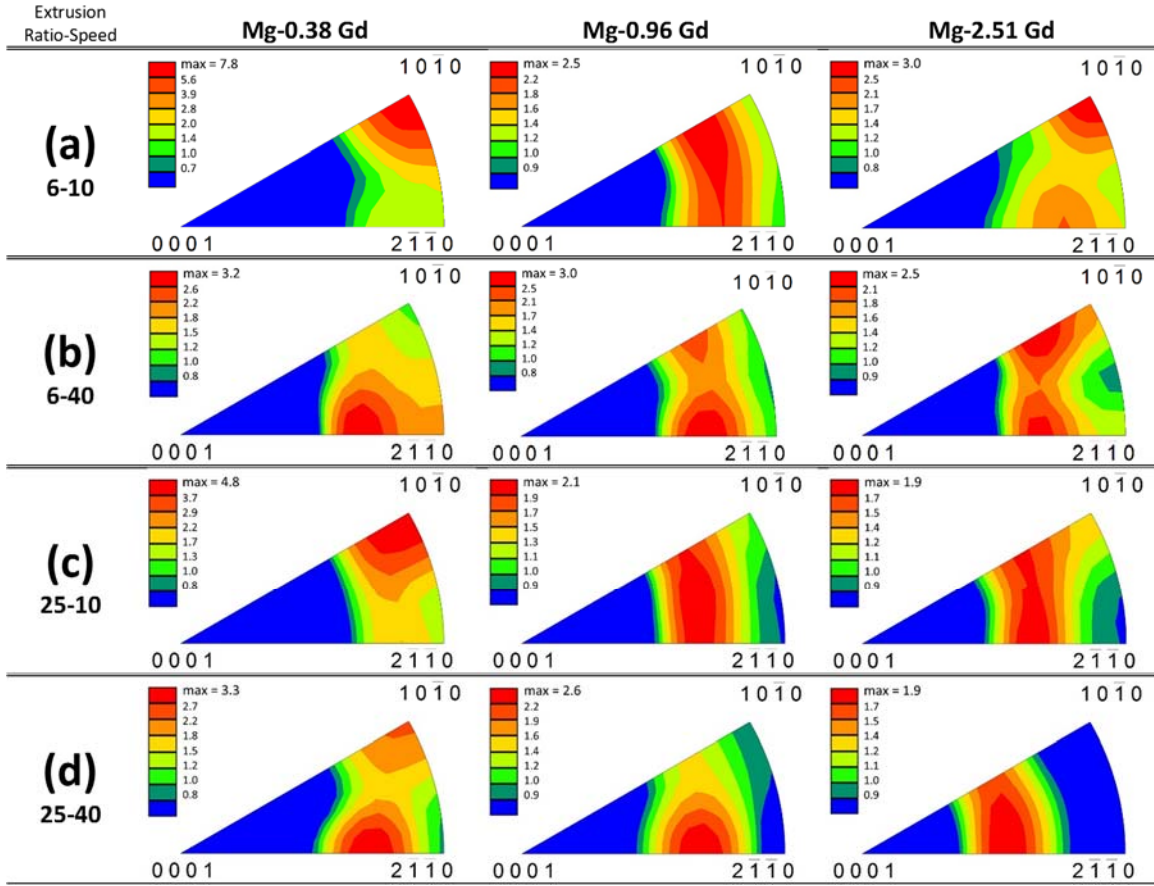
Figure 4.5   Inverse pole figures (IPF) of the recrystallized grains of the binary Mg-Gd alloys with 0.38, 0.96 and 2.51 wt. % Gd.

Extruded at 450 ºC **a)** with 10 mm/min ram speed and 1:6 area reduction ratio, **b)** with 40 mm/min ram speed and 1:6 area reduction ratio, **c)** with 10 mm/min ram speed and 1:25 area reduction ratio, **d)** with 40 mm/min ram speed and 1:25 area reduction ratio. IPFs refer to extrusion direction.

At low speed extrusions, with inadequate strain energy, higher content of Gd is required to form RE textures (Figure 4.5a and c). In Figure 4.5a, increasing Gd concentration from 0.38 to 0.96 wt. % changes the texture pattern from a $\langle 10\bar{1}0 \rangle$ fiber to an $\langle 10\bar{1}1 \rangle - \langle 11\bar{2}2 \rangle$ arc, while addition of 2.51 wt. % Gd results in development of a RE component along with $\langle 10\bar{1}0 \rangle$ fiber. We consider the arc as an intermediate configuration for the process of RE texture formation.

Figure 4.6   Inverse pole figure ED map of Mg-0.38 wt. % Gd alloy.

extruded at 450 ºC with 10 mm/min ram speed and 1:6 extrusion ratio with its corresponding IPF referring to extrusion direction, **b)** the corresponding image quality (IQ) map.

The texture evolution seems to start off from a parent with $\langle 10\bar{1}0 \rangle - \langle 11\bar{2}0 \rangle$ fiber rotating toward [0001] pole, stablishing an arc in the middle of stereographic triangle, and to end by developing distinct texture components including RE texture and $\langle 10\bar{1}0 \rangle$ fiber. However, the proportion of each texture component depends upon the materials and process variables. For instance, $\langle 10\bar{1}0 \rangle$ fiber disappears in Gd-containing alloys after high speed extrusions, while dilute alloys exhibit fairly strong $\langle 10\bar{1}0 \rangle$ fiber after low speed extrusions (Figure 4.5). Moreover, like Mg-Ce alloys, the position of RE fiber changes on the stereographic triangle for different samples. One can interpret this observation to be linked with dependence of recovery induced "backward rotation" with RE concentration and extrusion parameters. Our results suggest that RE fiber moves toward [0001] with increasing the Gd content or deformation stored energy.

133

Additionally, RE fiber seems to cover a range of orientations rather than a single pole. Hence, we propose that this phenomenon is induced by recovery of all active types of dislocations. Nucleation of a specific orientation during DRX is not defendable based on our results. It is worth noting that textural transition remains incomplete in samples with relatively small DRX grain sizes (10-14 μm), which reflects the key role of grain growth. The details of such textural development will be elaborated in the next sections with an emphasis on the role of DRX nucleation mechanisms and the origin of preferred grain growth.

4.3.2   Nucleation of dynamic recrystallization in binary Mg-RE alloys

Varying materials and process parameters not only facilitated observing texture evolution step by step, but also enabled us to link the evolution with the corresponding DRX driven microstructural changes. As the very first step in our characterization, we examine a microstructure in the early nucleation stage to assess the role of DRX mechanisms in nuclei formation. Figure 4.7 represents the microstructure and texture of Mg-0.41Ce extruded with 10 mm/min ram speed and 1:6 area reduction ratio. IQ maps around the boundaries of pancake shaped grains, as the main nucleation sites, are superimposed on the ED and ERD mapped IPF maps to help us observe the active DRX mechanism at the vicinity of each boundary. Interestingly, the top boundary in Figure 4.7a indicates formation of necklace structure through formation of sub-grains (indicated by arrows), which is reminiscent of CDRX mechanism. In the same IPF map, the boundary in the middle of Figure 4.7b shows signs of bulging.
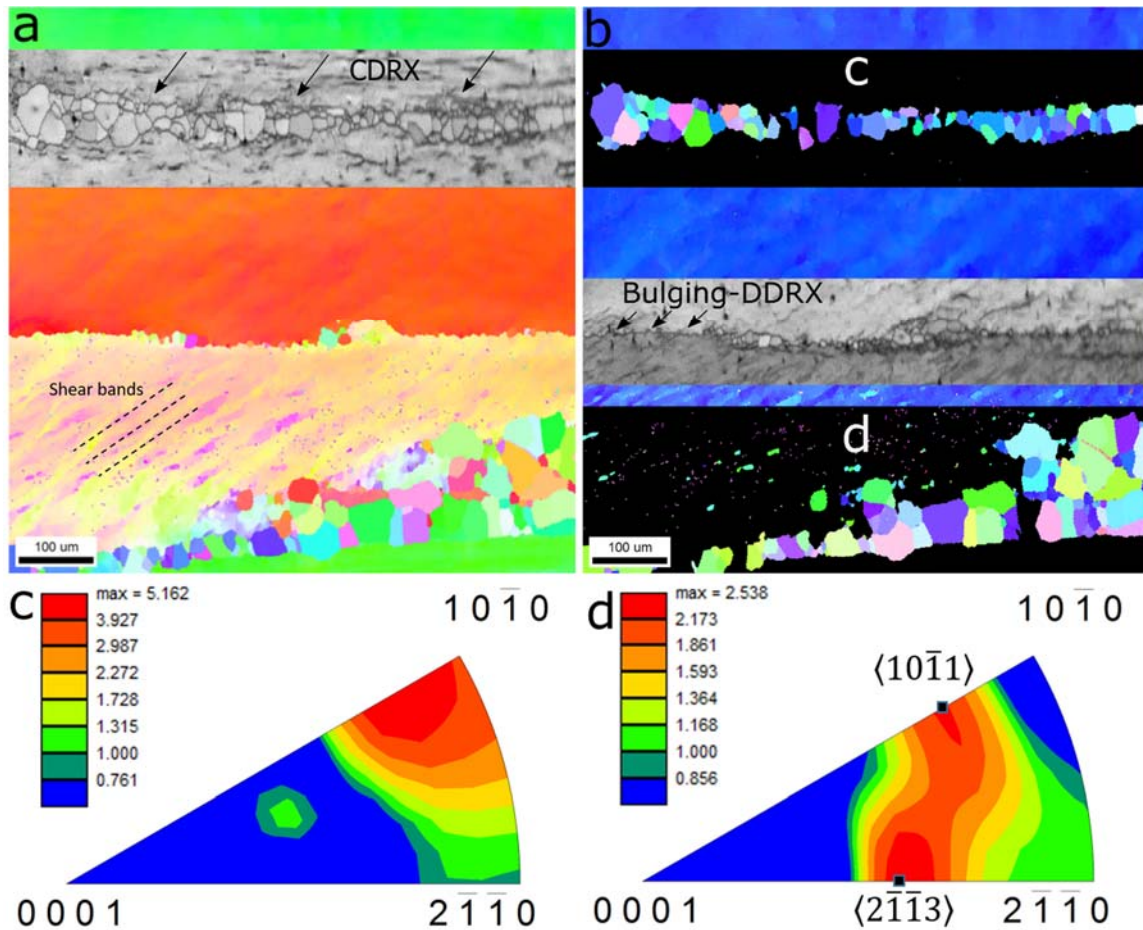
Figure 4.7   EBSD scan of extruded Mg-0.40 wt. % Ce alloy.

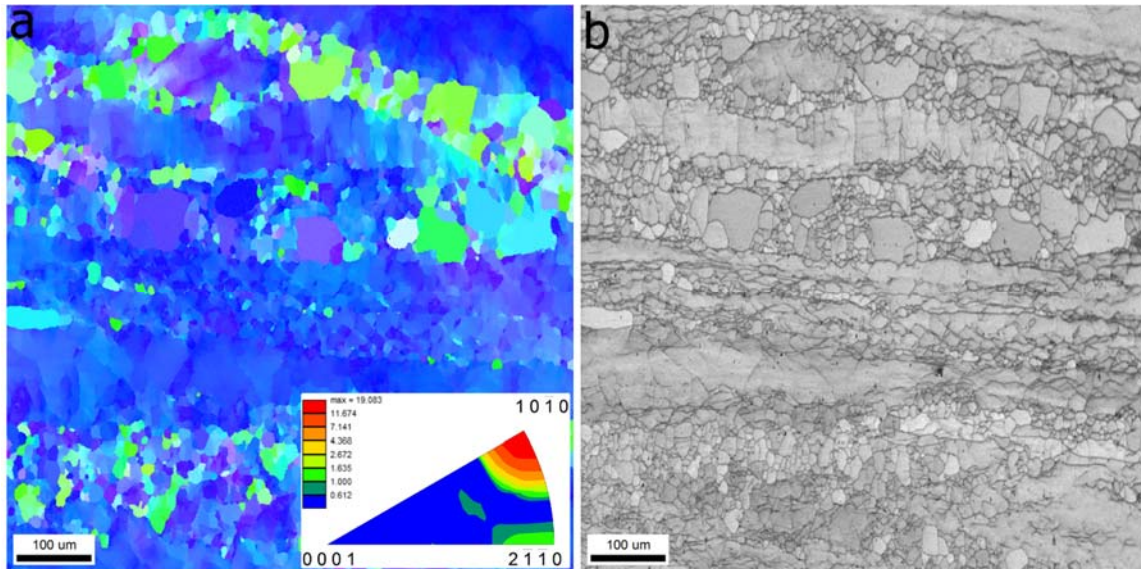**a)** Inverse pole figure (IPF) map of Mg-0.40 wt. % Ce alloy extruded at 450 °C with 10 mm/min ram speed and 1:6 extrusion ratio. The superimposed image quality (IQ) map indicates activity of continuous dynamic recrystallization (CDRX) through formation of low angle grain boundaries indicated by arrows. **b)** The superimposed IQ map indicates activity of discontinuous dynamic recrystallization (DDRX) through bulging mechanism. **c)** IPF of region *c* labeled in picture *(b)* associated with small CDRX grains displaying early stages of texture transition. **d)** IPF of region *d* labeled in picture *(b)* associated with larger CDRX grains representing the progress of textural transition with DRX grain growth. IPFs correspond to extrusion direction.

This observation demonstrates that both CDRX and DDRX mechanisms are active in the nucleation stage. Nevertheless, larger size of the grains nucleated by CDRX highlights the predominance of this mechanism over DDRX in binary Mg-RE alloys.

Although DDRX was observed to be the predominant mechanism in some Mg-RE alloys by the present authors [37], absence of other alloying elements in binary alloys, particularly Zn, facilitates the formation of cell structures by arranging a path with less elastic distortions for dislocation motion in a matrix with a faster bulk diffusion rate compared to complex Mg-RE alloys.

4.3.2.1   Nucleation of new orientations

Figure 4.8 is an EBSD scan with 0.1 µm step size from an area in a Mg-0.51Ce alloy sample extruded with 40 mm/min speed and 1:6 area reduction ratio. The selected area in Figure 4.8 is undergoing CDRX as the process continues by formation of sub-grains around the DRX nuclei in deformed Mg matrix. In Figure 4.8a, arrays of prismatic dislocations (highlighted in black) and basal/$\langle c + a \rangle$ dislocations (highlighted in red) construct the low angle grain boundaries (LAGB). Sub-grain embryos do not express any discernable rotation in their nucleation stage as they still carry the inherent misorientation of the dislocations at their boundaries (Figure 4.8b). On the other hand, CDRX nuclei in Figure 4.8a have undergone through a remarkable rotation, seeing their orientation relatively settled as the kernel average misorientation (KAM) map reveals small misorientations at their boundaries (Figure 4.8b). From a phenomenological point of view, the net rotation of these nuclei may be approximated as a function of type and population of dislocations being relaxed into their boundaries.
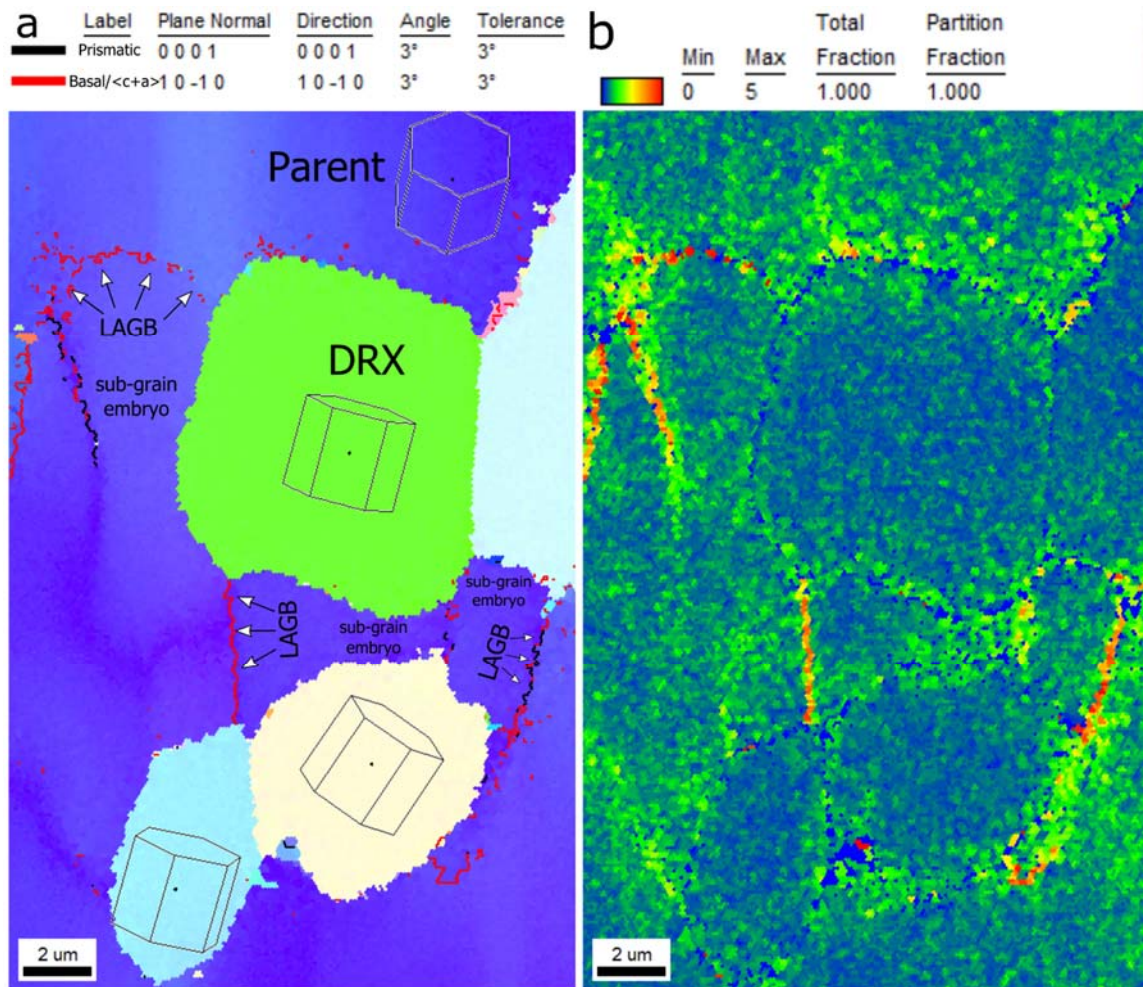
Figure 4.8   IGMA analysis of extruded 0.51 wt. % Ce alloy.

a) Inverse pole figure (IPF) ED map of Mg-0.51 wt. % Ce alloy extruded at 450 ºC with 40 mm/min ram speed and 1:6 extrusion ratio. Formation of low angle grain boundaries (LAGB) next to recrystallized grains within deformed matrix is indicated by arrows. Relaxation of basal/$\langle c + a \rangle$ (red lines) and prismatic dislocations (black lines) results in rotation of DRX embryos while LAGBs are forming. b) The corresponding kernel average misorientation (KAM) map showing high profiles of misorientation at the sites of LAGBs confirming higher misorientations induced by dislocations.

The total Taylor/rotation axis of active dislocations (or slip systems) and the total rotation can be estimated to be an arithmetic summation of all active slip systems [33, 52]:

137

$$\overrightarrow{T_{net}} = \sum_i \gamma_i \vec{T_i} \qquad (4.1)$$

Where γ_i is the shear strain induced by i^{th} slip system, and $\overrightarrow{T_{net}}$ is a vector in the direction of the rotation axis and with a magnitude equal to the total amount of rotation. Hence, one can reasonably envisage nucleation of a broad range of orientations induced by relaxation of a stochastic combination of GNDs.

In fact, a continuous formation of cell structures and sub-grains along the border of pancaked parents and CDRX necklaces transforms a sharp $\langle 10\bar{1}0 \rangle$ fiber texture into a randomized texture pattern. Figure 4.9 shows such a transformation in a Mg-2.51 Gd alloy extruded with 40 mm/min ram speed and extrusion ratio of 1:25. The IQ and KAM maps in Figure 4.9b and c show the formation of sub-structures at the DRX front with a fairly high misorientation profiles at LAGBs, by which the DRX front consumes the deformed zone, which leads to necklace structures coalescence. As aforementioned, a random combinations of all dislocations in the DRX front enables it to leave chains of randomly oriented grains behind (Figure 4.9d). Depending on the pace of DRX, the final microstructure may turn out being either partially or fully recrystallized. Figure 4.10 represents the microstructures of Gd and Ce containing alloys extruded with 40 mm/min ram speed and extrusion ratio of 1:25. The Mg-2.51Gd alloy depicts the big picture of a microstructure partially through the textural transformation, in which both $\langle 10\bar{1}0 \rangle$ fiber and RE driven components exist in the inset IPF of Figure 4.10a. On the other hand, Mg-0.51Ce alloy sees the nucleation stage almost completed as the $\langle 10\bar{1}0 \rangle$ fiber vanishes into a relatively stronger RE component (Figure 4.10b). Although the alloys in Figure 4.10 have different concentrations of Ce and Gd, our overall microstructural observations and DRX grain size measurements (Figure 4.4) suggests that Gd is more potent than Ce in

terms of recrystallization retardation and grain refinement while Ce seems to be a better choice for texture modification deploying thermo-mechanical processing (e.g. extrusion or rolling) without any further treatments.
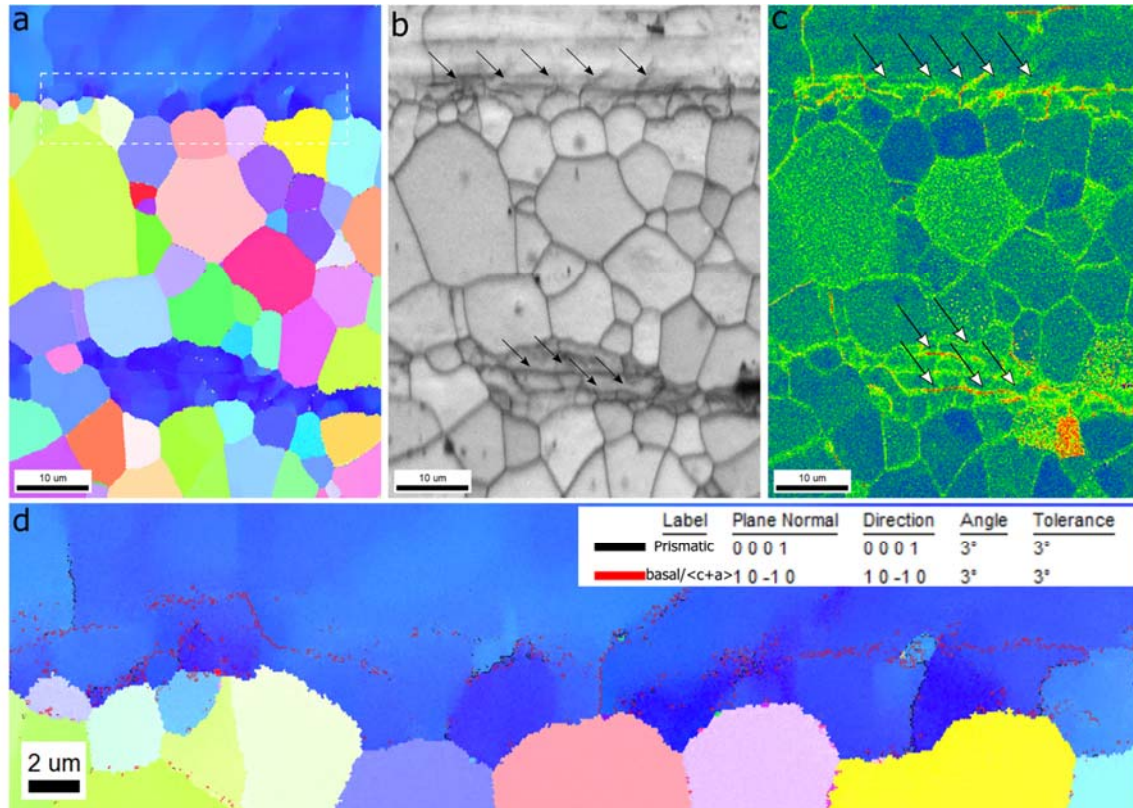
Figure 4.9   EBSD analysis of extruded Mg-2.5 wt. % Gd alloy.

a) A typical invers pole figure (IPF) ED map of Mg-2.5 wt. % Gd extruded at 450 ºC with 40 mm/min ram speed and 1:25 extrusion ratio. **b)** The corresponding image quality (IQ) map and **c)** kernel average misorientation (KAM) map show proceeding of continuous dynamic recrystallization (CDRX) front leading to coalescence of CDRX necklaces. **d)** Higher magnification of the region indicated by white dashes in picture *(a)* displaying concomitant relaxation of basal/$\langle c + a \rangle$ (red lines) and prismatic dislocations (black lines) at CDRX front, which leads to the formation of chains of randomly oriented DRX grains.
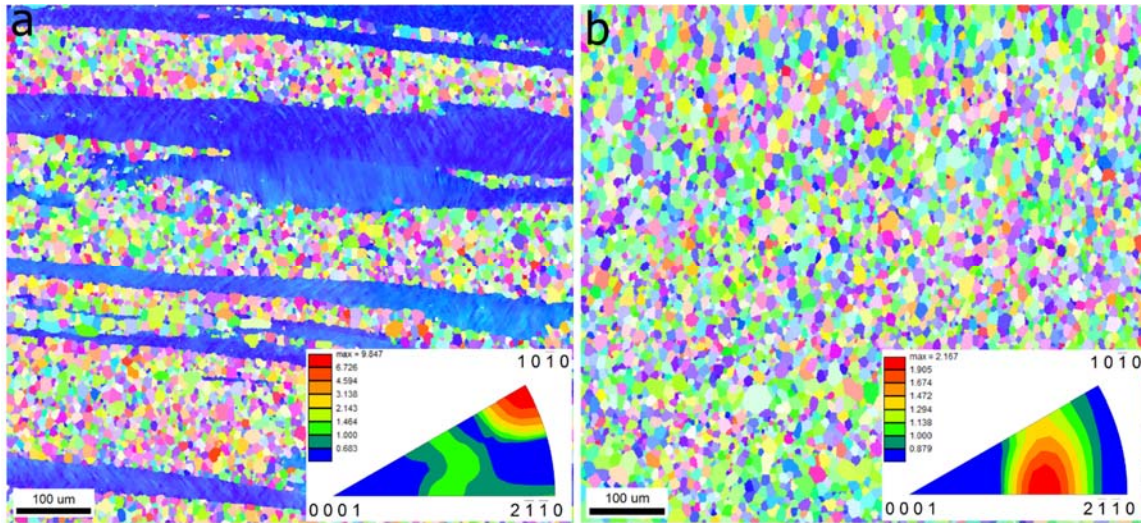
Figure 4.10   Typical inverse pole figure (IPF) ED maps along with their corresponding IPFs.

For **a)** Mg-2.5 wt. % Gd and **b)** Mg-0.51 wt. % Ce; extruded at 450 ºC with 40 mm/min ram speed and 1:25 extrusion ratio. IPFs correspond to extrusion direction.

4.3.2.2   Rotation of crystal lattices by dislocation recovery

Figure 4.7c and d are the IPF representation of regions c and d in figure 4.7b. Region c has its sharpest component slightly rotated from $\langle 10\bar{1}0 \rangle$ fiber toward $[0001]$ pole, while the IPF of region d displays a rotation from $\langle 10\bar{1}1 \rangle$ to $\langle 11\bar{2}3 \rangle$. Comparing regions c and d reveals the fact that larger DRX grain size of region d accounts for its lead in the progress for texture modification, which was yet undergoing changes toward a mature RE texture formation. The texture pattern of region c may indicate that RE texture phenomenon starts with a rotation from a parent grain with $\langle 10\bar{1}0 \rangle$ fiber texture toward $\langle 10\bar{1}1 \rangle$ around $\langle 11\bar{2}0 \rangle$ axis [37]. However, extreme mobility of the $28°/\{13\bar{4}0\}$ twin boundary may concomitantly enhance the population of grains with $\langle 11\bar{2}0 \rangle || ED$ component [51], thereby establishing an arc, e.g. $\langle 10\bar{1}0 \rangle - \langle 11\bar{2}0 \rangle || ED$, prior to rotation toward $[0001]$ pole. Therefore, depending on the amount of deformation stored energy

and RE concentration, such rotation around ⟨11$\bar{2}$0⟩ axis may yield an arc in the midst of stereographic triangle (see Figure 4.3 and 4.5). Thus we propose that recovery of basal/⟨$c + a$⟩ dislocations in RE containing Mg alloys initiates a "backward rotation" toward the [0001] pole, which in traditional Mg alloys rarely moves the grains more than 15 degrees toward the [0001] pole. This result we think is made possible by the combined effects of several properties of RE alloys: 1) RE additions homogenize and reduce the grain boundary energy [51]. This stabilizes a wide variety of grain boundary and mitigates Mg's preference for "special" boundaries. 2) RE additions reduce the CRSS for <c+a> slip, resulting in increased dislocation densities. 3) RE additions slow dislocation motion, again leading to increased dislocation densities to achieve the same rate of deformation 4) Most importantly, RE additions retard the DRX process, and thus allow DRX grain nuclei to "ripen" more extensively than occurs in traditional Mg alloys. In combination, these effects mean that the nucleation stage is prolonged by RE additions and that higher dislocation densities, particularly of <c+a> dislocations, are present to drive it. These dense dislocations repel one another which induces the backward crystal rotation as they move apart during recovery.

After the completion of recrystallization, formation of a hot spot around ⟨11$\bar{2}$2⟩ in the IPFs rather than an arc conveys a message regarding the stability of nuclei in one side of the pre-existing arc over the opposite side. A rotation around ⟨c⟩ axis induced by prismatic dislocation recovery may align the crystals with the RE component. However, consecutive cycles of prismatic dislocations recovery could potentially rotate a grain to a random orientation along the arc. Therefore, substantial abundance of grains along the

$[0001] - \langle 11\bar{2}0 \rangle$ side of the stereographic triangle can be rationalized by growth preference caused by geometrical factors of the deformation process, as we show below.

4.3.3   The mechanism of grain growth

Upon completion of the nucleation stage, the ensuing grain growth determines the final texture of a thermo-mechanically processed product. In contrast to traditional Mg alloys with a tendency to sharpen their texture upon grain growth [12], RE containing alloys have the tendency to develop texture components deviating from their parents [24, 32, 39]. Despite the consensus in the literature on the growth advantage of "RE oriented" grains, the main reasons behind this phenomenon remain ambiguous. In a recent study by the present authors on complex Mg-RE alloys [37], co-segregation of Zn and RE elements to grain boundaries was argued to promote a DDRX mechanism which supported random nuclei orientations. This observation gave rise to the hypothesis of grain boundary energy and mobility homogenization in Mg-RE alloys which was supported by atomistic simulations [51], and equips all the boundaries with nearly the same growth potential. Hence, texture randomization, including RE texture formation, was observed in MM-containing alloys [37]. However, binary Mg-RE alloys tend to prefer a certain range of orientations [23, 24], so the homogenization of grain boundary mobility leaves much unexplained. Another key factor must be considered to rationalize this phenomenon. Here, we take a closer look at growth behavior by using Schmid factor analysis to address the impact of any potential geometrical factors.

4.3.3.1   Dynamic grain growth

In order to examine the potency of dynamic grain growth for developing a modified texture, we compare the corresponding IPF patterns of all DRX grains against the ones for DRX grains greater than 20 μm in diameter (Figure 4.11). To this end, we selected two samples, one for each RE element, manifesting arc type IPF patterns to assess the potential of larger DRX grains to alter the IPF patterns. Additionally, we selected microstructures with high DRX volume fractions to assure our characterization's legitimacy.
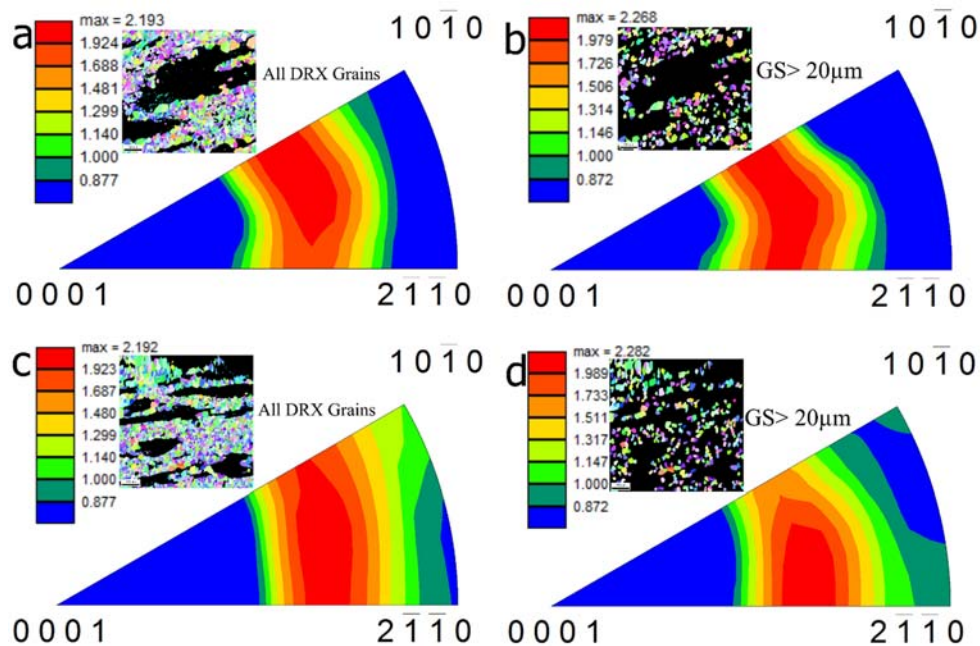
Figure 4.11   Inverse pole figures (IPF) of Mg-RE alloys extruded at 450 ºC with 10 mm/min ram speed;

a, b) Mg-0.23 wt. % Ce alloy (1:6 extrusion ratio), and **c, d)** Mg-0.96 wt. % Gd alloy (1:25 extrusion ratio). Left and right hand side IPFs represent texture of all recrystallized grains and ones larger than 20 μm in diameter, respectively. A comparison between the IPF patterns unravels that dynamic growth preference is not activated at low extrusion speeds. IPFs correspond to extrusion direction.

A stark comparison in Figure 4.11 reveals that, without adequate deformation energy, dynamic growth preference imposes a negligible effect on the final texture patterns, as they preserve their arc shape even at considerably larger grain sizes. Although the IPF patterns in Figure 4.11 seem to move slightly toward $[0001] - \langle 11\bar{2}0 \rangle$ side of the stereographic triangle, the change comes short of fulfilling a remarkable transformation. Hence, considering the extrusion condition, either Ce or Gd as fairly strong texture modifiers, seem to be incapable of modifying the dynamic growth behavior of magnesium in favor of RE component. However, with the same concentration of Ce, the transition from an arc to a hot spot was observed in Figure 4.12 to be finished off in a sample subject to higher deformation stored energy (imposed by greater extrusion ratio in this case). In fact, the intensity of RE component greatly increases when measuring only grains larger than 25 μm in diameter, by which "RE grains" manifest their dominant nature. One can hypothesize this observation to be driven by the larger population of GNDs generated by higher imposed strain, leading to the faster ripening of DRX grains. On the other hand, air cooling after extrusion renders this discussion contentious as to whether static grain growth assisted the completion of this textural transformation. We will address this question in the next section.

4.3.3.2   Static grain growth

We conducted isothermal annealing for 20 minutes and 3 hours at 450 ºC followed by water quenching to further substantiate the effect of static grain growth on texture evolution. Figure 4.13 shows that after soaking at 450 ºC for 20 minutes, RE texture is remarkably intensified compared to the as-extruded state in Figure 4.2a and 4.7.

144

Figure 4.12   A typical inverse pole figure (IPF) ED map of a Mg-0.23 wt. % Ce alloy.

Extruded at 450 ºC with 10 mm/min ram speed and 1:25 extrusion ratio along with IPFs corresponding to all grains, recrystallized (DRX) grains and DRX grains bigger than 25 μm in diameter. IPF for larger grains displays stronger RE texture compared to ones including all grain size ranges.

This straight forward comparison proves the significance of static grain growth in terms of orientation selection for DRX grains. Indeed, intensified RE texture in Figure 4.13 pertains to static grain growth as a large volume of deformed grains containing some shear bands retain their structure with no noticeable sign of static nucleation. With this in mind, we deem static grain growth as an influential factor, perhaps necessary in practice, to finish off the textural transformation. However, one should bear in mind that a mature RE textured product is achievable through dynamic recrystallization as well. For 3 hours annealing, we selected one sample for each RE element (e.g. Mg- 0.41 Ce and Mg-0.96 Gd extruded with 10 mm/min speed and 1:25

extrusion ratio (Figure 4.2c and 4.5c, respectively)). Their as-extruded IPF patterns represent middle stages of the above mentioned texture evolutions.
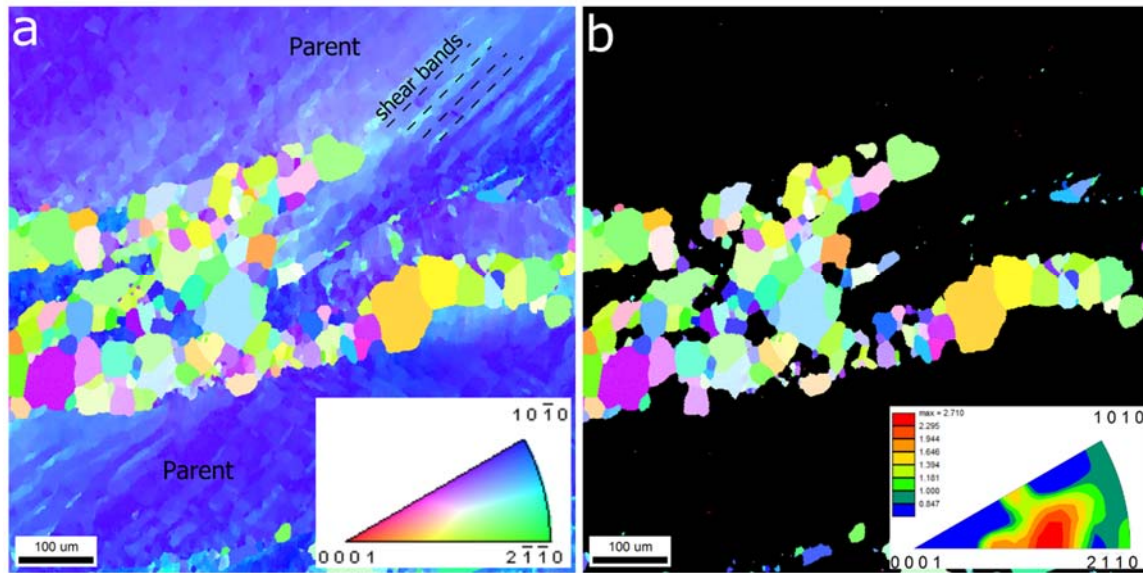
Figure 4.13   EBSD analyses of samples after annealing for 20 minutes.
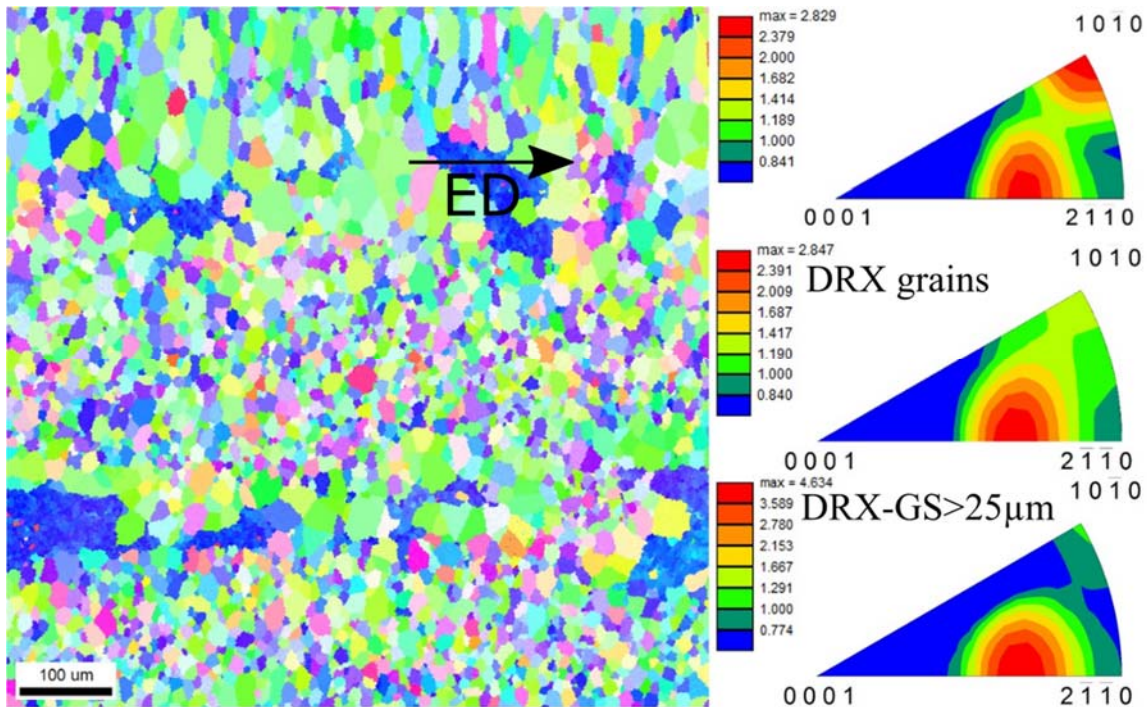
a) Inverse pole figure (IPF) ED map of a Mg-0.40 wt. % Ce alloy extruded at 450 ºC with 10 mm/min ram speed and 1:6 extrusion ratio, and annealed for 20 mins at 450 ºC. Despite the formation of shear bands, recrystallization nucleated on grain boundaries. **b)** Recrystallized grains with grain orientation spread (GOS) values smaller than 2º, showing a discernable static grain growth resulting in transition of texture pattern from an arch to a hot spot.

After annealing for 3 hours, static grain growth accomplishes the textural transformation strengthening the RE component. The Mg-0.41 Ce alloy transforms from a double component pattern (i.e. RE and $\langle 10\bar{1}0 \rangle$ fiber) to a single component that covers nearly half length of the $[0001] - \langle 11\bar{2}0 \rangle$ side of the stereographic triangle (Figure 4.14a). Despite the obvious similarity to the well-known RE texture component, the broader range of this fiber insinuates a growth advantage for $[0001] - \langle 11\bar{2}0 \rangle$ side over the $[0001] - \langle 10\bar{1}0 \rangle$ side of the stereographic triangle. The Gd-containing alloy,

after annealing for 3 hours, shows nearly the same textural features in Figure 4.14b

compared to the Ce-containing alloy in Figure 4.14a. In this case, the broad $\langle 11\bar{2}1 \rangle -$

$\langle 11\bar{2}4 \rangle$ fiber develops from an arc (Figure 4.5c). Therefore, regardless of the orientation

of non-RE oriented grains, they lose the growth race to RE grains. It is worth noting that

dynamic and static growth seem to act similarly in terms of texture selection, though the

available time span for static grain growth is an adjustable parameter that renders it a

more effective.
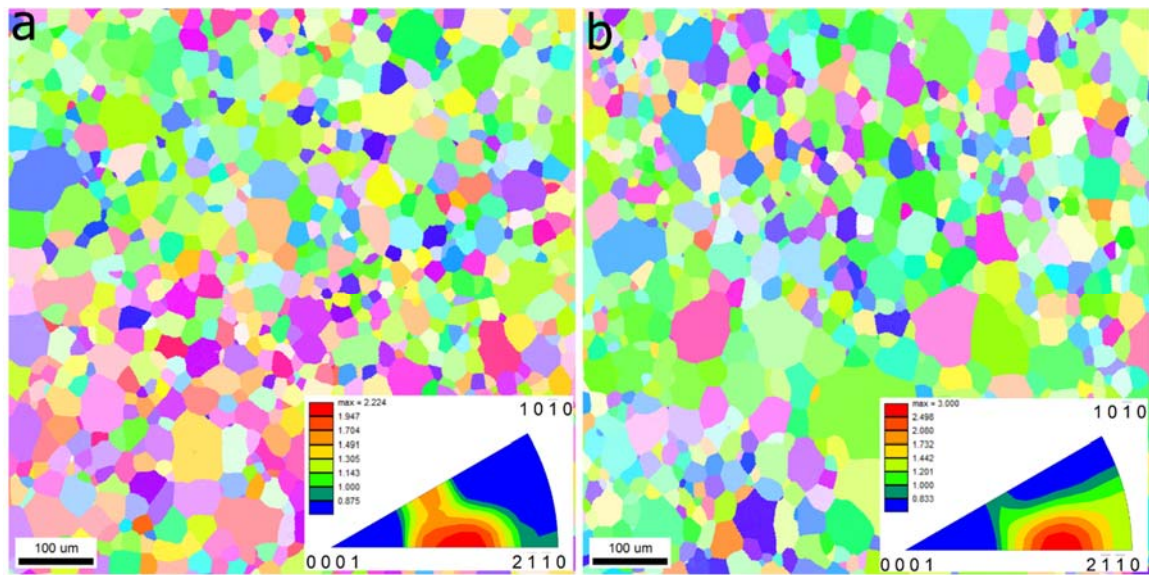
Figure 4.14   EBSD analysis of samples annealed for 3 hours.

Typical inverse pole figure (IPF) ED maps along with their corresponding IPFs for **a)** Mg-0.40 wt. % Ce and **b)** Mg-0.96 wt. % Gd; extruded at 450 ºC with 10 mm/min ram speed and 1:25 extrusion ratio, and annealed for 3 hours at 450 ºC. IPFs correspond to extrusion direction. Static grain growth completes textural transformation from an arch to a hot spot through granting time for preferential grain growth.

Considering the widespread variation of orientations in RE grains and their

surrounding RE/random grains, it was implausible to find a specific grain boundary with

high mobility accounting for the growth privilege of RE grains. We were not able to

recognize an identifiable trend in the misorientation axis/angle distribution, as a great

variety for high angle boundaries existed throughout the microstructure. On the other

hand, the observed broad $\langle 11\bar{2}1 \rangle - \langle 11\bar{2}4 \rangle$ fibers in Figure 4.14 intrigues a geometrical

viewpoint in which the orientation of crystals within an extrudate may play a decisive

role.

4.3.3.3 Schmid factor analysis

Figure 4.15 depicts the Schmid factor (SF) map along with ED mapped IPF and

image quality (IQ) map for a Mg-0.41Ce alloy extruded at 40 mm/min speed and 1:25

extrusion ratio. Employing TSL-OIM software, Schmid factor analysis was conducted for

a combined set of dislocation types including basal, prismatic and $\langle c + a \rangle$ dislocations.

We defined the critical resolved shear stress (CRSS) ratios as 1:5:10 (i.e.

$CRSS_{basal}$:$CRSS_{prismatic}$:$CRSS_{<c+a>}$) [10]. The stress state was defined as compressive in-

plane stress. The SF analysis in Figure 4.15a reveals higher SF values for the

corresponding purple and blue grains in the ED mapped IPF (Figure 4.15b), which

belong to the $[0001] - \langle 10\bar{1}0 \rangle$ side of the stereographic triangle. The actual reason

behind this effect is totally geometric. In essence, extrusion exerts nearly the same state

and magnitude of stress to all the neighboring grains, wherein the crystallographic

orientation tallies the net plastic deformation carried by a grain. Hence, a higher net

activity of dislocations is conceivable for blue and purple grains in Figure 4.15b. They

have a noticeably smaller grain size in Figure 4.15c, implying their proneness to

annihilation during grain growth. In fact, the driving force for the preferred growth of RE

grains (green in color) is supplied by their lower SF values, and hence smaller population

of GNDs. In other terms, high angle grain boundaries select their motion direction based

on the dislocation density gradient that applies a force to the boundary toward the grain

with higher dislocation density.
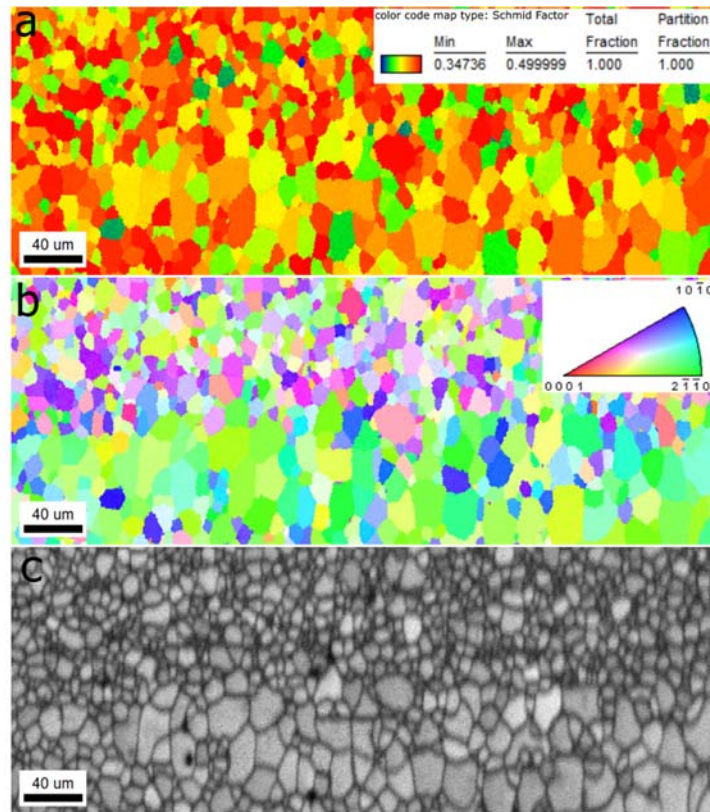
Figure 4.15   Schmid factor analysis of extruded Mg-0.4 wt. %Ce alloy.

a) Schmid factor (SF) map of Mg-0.4 wt. %Ce alloy extruded at 450 ℃ with 40 mm/min ram speed and 1:25 extrusion ratio. Purple and blue grains in the IPF ED map in **(b)** commensurate with higher SF values under compressive in-plane stress state, which suppresses their growth by virtue of higher dislocation activation, and hence, higher deformation stored energy. In fact, green grains with lower energy grow in the cost of high energy grains to reduce the total energy of system. **c)** The corresponding image quality (IQ) map indicating smaller grain size for grains with higher SF.

With that being said, one can rationalize the annihilation of $[0001] - \langle 10\bar{1}0 \rangle$

grains with higher GND population in favor of $[0001] - \langle 11\bar{2}0 \rangle$ grains. We conducted

SF analysis on an area with abnormal grain growth to examine the curvature of the high

angle boundaries between green and blue/purple grains.
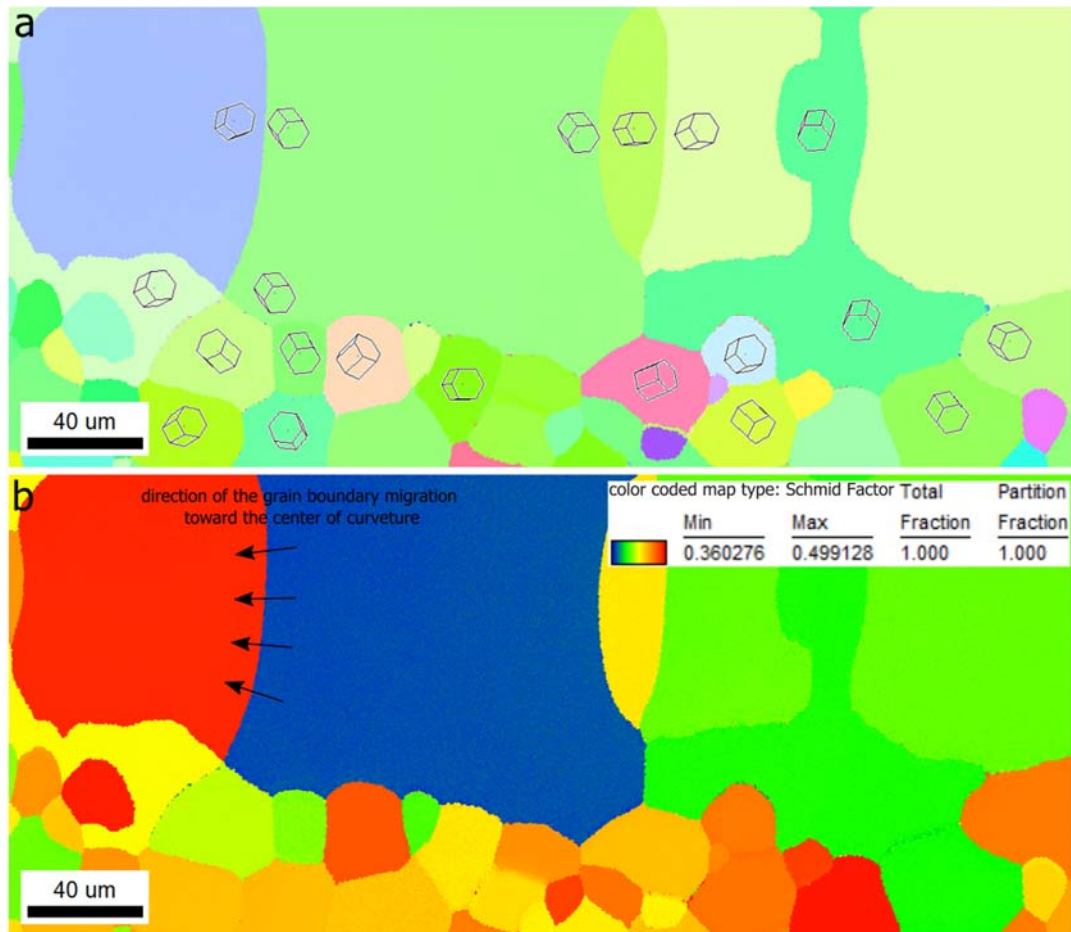
Figure 4.16   Schmid factor analysis of extruded Mg-0.96 wt. % Gd alloy.

a) Inverse pole figure (IPF) ED map taken from an area with abnormal grain growth in a Mg-0.96 wt. % Gd alloy extruded at 450 ºC with 10 mm/min ram speed and 1:25 extrusion ratio, and annealed for 3 hours at 450 ºC. **b)** The corresponding Schmid factor (SF) map under compressive in-plane stress state, depicting growth preference of low SF grains that belong to the $[0001] - \langle 10\bar{1}0 \rangle$ side of the stereographic triangle. The centers of curvature, which determines the boundary migration direction, is located within high SF grains. This effect is conspicuous in abnormally grown grains indicate by arrows.

The center of curvature lies within the blue grain in the top left corner of

Figure 4.16a (indicated by arrows), which has a considerably higher SF value in

Figure 4.16b. As in traditional grain growth mechanism, the interface moves toward the center of curvature, thereby wiping away the blue grain [54]. This observation was an additional evidence that, even in regions with abnormal grain growth, RE grains possess growth preference because of their orientation rendering them favorable for reducing the total energy of system.

4.4   Recapitulation

Thus, in summary, we propose that the well-known "RE texture" is a result of RE additions' modification on DRX grain nucleation and growth, stemming from their modifications of grain boundary and dislocation properties. This texture arises as a result, first, of higher dislocation densities present in deformed grains, particularly <c+a> dislocations. These higher densities arise from the reduced CRSS for <c+a> slip and the reduced mobility for all dislocations. These high dislocation densities induce a "backward rotation" of DRX grain nuclei during recovery resulting in a band of texture intensity roughly 35-65 degrees from $\langle 10\bar{1}0\rangle||ED$ fiber. The formation of a wide variety of grain boundary misorientations is more favorable than in traditional Mg alloys because grain boundary energy cusps which interrupt plastic spin are less prevalent due to segregated RE elements at grain boundaries. Moreover, the nucleation stage of DRX is retarded with RE additions present, allowing grains to rotate further than in traditional Mg alloys. Finally, grain growth favors grains near the $\langle 11\bar{2}1\rangle||ED$ component because these grains have lower Schmid factors and therefore lower dislocation densities, leading to them consuming grains with higher densities and thereby relaxing the system. Therefore, the role of RE elements is integrated with that of GNDs during DRX and neither can produce RE texture without a sufficient concentration of the other. This theory suggests that future

151

work seeking economically randomize DRX textures in Mg alloys should focus on methods of producing higher concentrations of GNDs without inducing cracking and on retarding the nucleation stage of recrystallization to alloy DRX nuclei to further mature before grain growth takes over.

4.5   Conclusions

We studied the effect of processing conditions and rare earth element concentration on formation and evolution of texture in two binary magnesium-rare-earth element (Mg-RE) alloys at various compositions. We selected Ce and Gd which exhibit low and high solubility limits, respectively. By designing proper materials and process variables, the details of microstructure and texture evolution were scrupulously analyzed and discussed explicated. We conclude the following:

1. The threshold concentration of rare earth elements for texture modification depends on the imposed strain energy. Defining an absolute value for rare earth element threshold concentration is thus unrealistic unless the deformation condition is consistent from one material to the other. This was clearly demonstrated for some Ce and Gd containing magnesium alloys which failed to develop any RE texture under reasonable extrusion conditions despite concentrations were well above the threshold limit. Extrusion condition may potentially favor or suppress rare earth texture evolution, in which the deformation stored energy and recrystallized grain size are the most important factors.

2. Continuous dynamic recrystallization was the predominant nucleation mechanism in binary Mg-RE alloys, as the size of continuous dynamic recrystallization grains overshadowed that of embryos nucleated through bulging. In this study, higher bulk diffusion rate due to high purity level of the cast alloys may account for the faster growth of sub-grains. Cell-structures continuously nucleated along the interface between recrystallized and parent grains through recovery of geometrically necessary dislocations including basal $\langle a \rangle$, prismatic $\langle a \rangle$, and $\langle c + a \rangle$ dislocations. A stochastic relaxation of dislocations into low angle grain boundaries is associated with the rotation of sub-grains, which produces necklaces of recrystallized grains with orientations forming a fairly wide arc in the stereographic triangle.

3. Survival and growth of new orientations is the most important influence of rare earth element additions on the recrystallization texture of Mg. Rare earth texture components manifest higher intensities where the average recrystallized grain size is larger. Our investigation suggests that static and dynamic grain growth grant a nearly equal drive for recrystallization to modify the deformation texture. Meanwhile, depending on the desired final texture and deformation condition, one can consider static grain growth as an effective tool for further texture modifications.

4. Schmid factor (SF) analysis showed a higher accumulative activity for basal $\langle a \rangle$, prismatic $\langle a \rangle$, and $\langle c + a \rangle$ dislocations in grains oriented close to the $[0001] - \langle 10\bar{1}0 \rangle || ED$ compared to the ones oriented close to $[0001] - \langle 11\bar{2}0 \rangle || ED$ (i.e. RE grains) texture components. In other words, blue and purple grains in ED mapped IPFs accommodate more plastic deformation than RE grains. Hence, the migration direction of grain boundaries toward the grains with higher dislocation density favors the growth of RE grains, which transforms an arc-shaped texture pattern to a hot spot on the calculated IPFs. Overall, growth preference of RE grains is a geometrical phenomenon explained by the orientation of grains with respect to the imposed in-plane stress during extrusion.

5. We propose a new integrated description of how rare earth element additions randomize and alter the texture of dynamically recrystallized Mg alloys, suggesting promising areas for further inquiry into how to cost-effectively enhance Mg alloy performance.

4.6   Acknowledgment

4.7 References

[1] B. Mordike, T. Ebert, Magnesium: properties—applications—potential, Mater. Sci. Eng. A 302 (2001) 37-45.

[2] I. Polmear, Magnesium alloys and applications, Mater. Sci. Technol. 10 (1994) 1-16.

[3] P. Changizian, A. Zarei-Hanzaki, M. Ghambari, A. Imandoust, Flow localization during severe plastic deformation of AZ81 magnesium alloy: Micro-shear banding phenomenon, Mater. Sci. Eng. A 582 (2013) 8-14.

[4] Y. Chino, M. Kado, M. Mabuchi, Compressive deformation behavior at room temperature – 773K in Mg–0.2mass%(0.035at.%)Ce alloy, Acta Mater. 56 (2008) 387-394.

[5] Y. Chino, M. Kado, M. Mabuchi, Enhancement of tensile ductility and stretch formability of magnesium by addition of 0.2wt%(0.035at%)Ce, Mater. Sci. Eng. A 494 (2008) 343-349.

[6] J. Del Valle, M.T. Pérez-Prado, O. Ruano, Texture evolution during large-strain hot rolling of the Mg AZ61 alloy, Mater. Sci. Eng. A 355 (2003) 68-78.

[7] H. El Kadiri, C.D. Barrett, J. Wang, C.N. Tomé, Why are twins profuse in magnesium?, Acta Mater. 85 (2015) 354-361.

[8] H. El Kadiri, J. Kapil, A. Oppedal, L. Hector, S.R. Agnew, M. Cherkaoui, S. Vogel, The effect of twin–twin interactions on the nucleation and propagation of twinning in magnesium, Acta Mater. 61 (2013) 3549-3563.

[9] A. Imandoust, C. Barrett, T. Al-Samman, K. Inal, H. El Kadiri, A review on the effect of rare-earth elements on texture evolution during processing of magnesium alloys, J. Mater. Sci. 52 (2017) 1-29.

[10] S. Agnew, M. Yoo, C. Tome, Application of texture simulation to understanding mechanical behavior of Mg and solid solution alloys containing Li or Y, Acta Mater. 49 (2001) 4277-4289.

[11] S.R. Agnew, L. Capolungo, C.A. Calhoun, Connections between the basal I1 "growth" fault and ⟨c+a⟩ dislocations, Acta Mater. 82 (2015) 255-265.

[12] S.R. Agnew, Ö. Duygulu, Plastic anisotropy and the role of non-basal slip in magnesium alloy AZ31B, Int. J. Plast. 21 (2005) 1161-1193.

[13] S.R. Agnew, J.A. Horton, T.M. Lillo, D.W. Brown, Enhanced ductility in strongly textured magnesium produced by equal channel angular processing, Scripta Mater. 50 (2004) 377-381.

[14] S.R. Agnew, C.N. Tomé, D.W. Brown, T.M. Holden, S.C. Vogel, Study of slip mechanisms in a magnesium alloy by neutron diffraction and modeling, Scripta Mater. 48 (2003) 1003-1008.

[15] M. Barnett, M. Nave, C. Bettles, Deformation microstructures and textures of some cold rolled Mg alloys, Mater. Sci. Eng. A 386 (2004) 205-211.

[16] M.R. Barnett, Twinning and the ductility of magnesium alloys, Mater. Sci. Eng. A 464 (2007) 8-16.

[17] T. Al-Samman, X. Li, Sheet texture modification in magnesium-based alloys by selective rare earth alloying, Mater. Sci. Eng. A 528 (2011) 3809-3822.

[18] I. Basu, T. Al-Samman, G. Gottstein, Shear band-related recrystallization and grain growth in two rolled magnesium-rare earth alloys, Mater. Sci. Eng. A 579 (2013) 50-56.

[19] J. Bohlen, M.R. Nürnberg, J.W. Senn, D. Letzig, S.R. Agnew, The texture and anisotropy of magnesium–zinc–rare earth alloy sheets, Acta Mater. 55 (2007) 2101-2112.

[20] X. Li, T. Al-Samman, G. Gottstein, Mechanical properties and anisotropy of ME20 magnesium sheet produced by unidirectional and cross rolling, Mater. Des. 32 (2011) 4385-4393.

[21] J. Bohlen, S. Yi, D. Letzig, K.U. Kainer, Effect of rare earth elements on the microstructure and texture development in magnesium–manganese alloys during extrusion, Mater. Sci. Eng. A 527 (2010) 7092-7098.

[22] L.L. Rokhlin. Magnesium alloys containing rare earth metals: structure and properties, Crc Press, 2003.

[23] N. Stanford, Micro-alloying Mg with Y, Ce, Gd and La for texture modification—A comparative study, Mater. Sci. Eng. A 527 (2010) 2669-2677.

[24] N. Stanford, M.R. Barnett, The origin of "rare earth" texture development in extruded Mg-based alloys and its effect on tensile ductility, Mater. Sci. Eng. A 496 (2008) 399-408.

[25] R.K. Mishra, A.K. Gupta, P.R. Rao, A.K. Sachdev, A.M. Kumar, A.A. Luo, Influence of cerium on the texture and ductility of magnesium extrusions, Scripta Mater. 59 (2008) 562-565.

[26] S. Sandlöbes, M. Friák, S. Zaefferer, A. Dick, S. Yi, D. Letzig, Z. Pei, L.F. Zhu, J. Neugebauer, D. Raabe, The relation between ductility and stacking fault energies in Mg and Mg–Y alloys, Acta Mater. 60 (2012) 3011-3021.

[27] S. Sandlöbes, S. Zaefferer, I. Schestakow, S. Yi, R. Gonzalez-Martinez, On the role of non-basal deformation mechanisms for the ductility of Mg and Mg–Y alloys, Acta Mater. 59 (2011) 429-439.

[28] J. Yasi, T. Nogaret, D. Trinkle, Y. Qi, L. Hector Jr, W. Curtin, Basal and prism dislocation cores in magnesium: comparison of first-principles and embedded-atom-potential methods predictions, Modell. Simul. Mater. Sci. Eng. 17 (2009) 055012.

[29] R. Cottam, J. Robson, G. Lorimer, B. Davis, Dynamic recrystallization of Mg and Mg–Y alloys: Crystallographic texture development, Mater. Sci. Eng. A 485 (2008) 375-382.

[30] J. Del Valle, O.A. Ruano, Influence of texture on dynamic recrystallization and deformation mechanisms in rolled or ECAPed AZ31 magnesium alloy, Mater. Sci. Eng. A 487 (2008) 473-480.

[31] N. Stanford, D. Atwell, M.R. Barnett, The effect of Gd on the recrystallisation, texture and deformation behaviour of magnesium-based alloys, Acta Mater. 58 (2010) 6773-6783.

[32] N. Stanford, D. Atwell, A. Beer, C. Davies, M.R. Barnett, Effect of microalloying with rare-earth elements on the texture of extruded magnesium-based alloys, Scripta Mater. 59 (2008) 772-775.

[33] J.P. Hadorn, K. Hantzsche, S. Yi, J. Bohlen, D. Letzig, S.R. Agnew, Effects of Solute and Second-Phase Particles on the Texture of Nd-Containing Mg Alloys, Metall. Mater. Trans. A 43 (2012) 1363-1375.

[34] J.P. Hadorn, K. Hantzsche, S. Yi, J. Bohlen, D. Letzig, J.A. Wollmershauser, S.R. Agnew, Role of Solute in the Texture Modification During Hot Deformation of Mg-Rare Earth Alloys, Metall. Mater. Trans. A 43 (2011) 1347-1362.

[35] K. Hantzsche, J. Bohlen, J. Wendt, K.U. Kainer, S.B. Yi, D. Letzig, Effect of rare earth additions on microstructure and texture development of magnesium alloy sheets, Scripta Mater. 63 (2010) 725-730.

[36] J.D. Robson, A.M. Twier, G.W. Lorimer, P. Rogers, Effect of extrusion conditions on microstructure, texture, and yield asymmetry in Mg–6Y–7Gd–0.5wt%Zr alloy, Mater. Sci. Eng. A 528 (2011) 7247-7256.

[37] A. Imandoust, H. El Kadiri, C.D. Barrett, T. Al-Samman, S.R. Agnew, M.A. Tschopp, E. Essadiqi, N. Hort, Unraveling recrystallization mechanisms governing texture development from rare earth element additions to magnesium Acta Mater. Under review.

[38] I. Basu, K. Pradeep, C. Mießen, L. Barrales-Mora, T. Al-Samman, The role of atomic scale segregation in designing highly ductile magnesium alloys, Acta Mater. 116 (2016) 77-94.

[39] J.P. Hadorn, R.P. Mulay, K. Hantzsche, S. Yi, J. Bohlen, D. Letzig, S.R. Agnew, Texture Weakening Effects in Ce-Containing Mg Alloys, Metall. Mater. Trans. A 44 (2012) 1566-1576.

[40] E. Ball, P. Prangnell, Tensile-compressive yield asymmetries in high strength wrought magnesium alloys, Scripta Metallurgica et Materialia 31 (1994) 111-116.

[41] M. Sanjari, A. Farzadfar, A.S.H. Kabir, H. Utsunomiya, I.-H. Jung, R. Petrov, L. Kestens, S. Yue, Promotion of texture weakening in magnesium by alloying and thermomechanical processing: (I) alloying, J. Mater. Sci. 49 (2013) 1408-1425.

[42] T. Al-Samman, G. Gottstein, Dynamic recrystallization during high temperature deformation of magnesium, Mater. Sci. Eng. A 490 (2008) 411-420.

[43] Z.R. Zeng, M.Z. Bian, S.W. Xu, C.H.J. Davies, N. Birbilis, J.F. Nie, Texture evolution during cold rolling of dilute Mg alloys, Scripta Mater. 108 (2015) 6-10.

[44] Z.R. Zeng, Y.M. Zhu, S.W. Xu, M.Z. Bian, C.H.J. Davies, N. Birbilis, J.F. Nie, Texture evolution during static recrystallization of cold-rolled magnesium alloys, Acta Mater. 105 (2016) 479-494.

[45] M. Steiner, J. Bhattacharyya, S. Agnew, The origin and enhancement of texture during heat treatment of rolled AZ31B magnesium alloys, Acta Mater. 95 (2015) 443-455.

[46] J. Bohlen, S.B. Yi, J. Swiostek, D. Letzig, H.G. Brokmeier, K.U. Kainer, Microstructure and texture development during hydrostatic extrusion of magnesium alloy AZ31, Scripta Mater. 53 (2005) 259-264.

[47] N. Stanford, M. Callaghan, B. De Jong, The effect of rare earth elements on the behaviour of magnesium-based alloys: Part 1—Hot deformation behaviour, Mater. Sci. Eng. A 565 (2013) 459-468.

[48] N. Stanford, R. Cottam, B. Davis, J. Robson, Evaluating the effect of yttrium as a solute strengthener in magnesium using in situ neutron diffraction, Acta Mater. 78 (2014) 1-13.

[49] N. Stanford, G. Sha, J. Xia, S. Ringer, M. Barnett, Solute segregation and texture modification in an extruded magnesium alloy containing gadolinium, Scripta Mater. 65 (2011) 919-921.

[50] C.D. Barrett, A. Imandoust, H. El Kadiri, Homogenization of grain boundary energy in magnesium by yttrium segregation, Scripta Mater. Under Review.

[51] C.D. Barrett, A. Imandoust, A.L. Oppedal, K. Inal, M.A. Tschopp, H. El Kadiri, Effect of grain boundaries on texture formation during dynamic recrystallization of magnesium alloys, Acta Mater. 128 (2017) 270-283.

[52] Y.B. Chun, M. Battaini, C.H.J. Davies, S.K. Hwang, Distribution Characteristics of In-Grain Misorientation Axes in Cold-Rolled Commercially Pure Titanium and Their Correlation with Active Slip Modes, Metall. Mater. Trans. A 41 (2010) 3473-3487.

[53] A. Rollett, F. Humphreys, G.S. Rohrer, M. Hatherly. Recrystallization and related annealing phenomena, Elsevier, 2004.

CHAPTER V

EFFECT OF RARE EARTH ON EXTENSION TWINNING INDUCED HARDENING

IN MAGNESIUM

5.1 Introduction

Traditional magnesium (Mg) alloys are known to exhibit poor formability at ambient temperature due to an effect associated with profuse twinning as all easy slip systems have their burgers vector lying only on the basal plane [1, 2]. $\{10\bar{1}2\}$ twinning is a universal twinning mode in most hexagonal close-packed structures and its critical resolved shear stress (CRSS) is particularly small for Mg, whereas $\langle c + a \rangle$ dislocations have threshold stresses which can be an order of magnitude higher for temperatures below 180 ºC [1, 2]. Hence, profuse $\{10\bar{1}2\}$ twinning takes place at low temperatures whenever deformation imposes plastic stretching along the $\langle c \rangle$-axis. However, because of the polarity of this twin mode pyramidal $\langle c + a \rangle$ slip triggers to accommodate plastic shortening along $\langle c \rangle$-axis[1]. $\{10\bar{1}1\}$ twins could also trigger to provide $\langle c \rangle$-axis compression or contraction but their threshold stress is much higher than that of pyramidal $\langle c + a \rangle$ slip.

The profuse activity of $\{10\bar{1}2\}$ twinning is known to cause a dramatic escalation of the hardening rate in HCP metals, but more particularly in Mg as the parent grain can be entirely consumed by this twin mode [3]. This results in a sigmoidal-shaped flow of the stress-strain behavior in sharply textured wrought alloys undergoing compression

normal to the main $\langle c \rangle$-axis fibers [4-6]. When the stress sign is inverted (asymmetry) for the same loading direction or vice-versa (anisotropy), $\{10\bar{1}2\}$ twinning is remarkably obviated in these sharp fibers. However, ductility remains unimproved. It has been suggested that $\{10\bar{1}2\}$ only ensues $\{10\bar{1}1\}$ twins (i.e. double twinning), which have been shown to be very detrimental to ductility as they can turn literally into cracks shortly after their nucleation [7, 8]. Additions of rare earth (RE) elements in Mg and its alloys have been shown to noticeably reduce anisotropy/asymmetry and ameliorate ductility. Several effects have been mentioned but there is a general consensus on texture weakening effects [9, 10]. In fact, RE enhances the formation of recrystallized grains which substantially deviate from the ideal fiber orientation after rolling or extrusion, making them less prone to twinning [2]. Nevertheless, $\{10\bar{1}2\}$ twinning is unequivocally active at room temperature (RT) [11], and its hardening effects play a significant role in RT formability of Mg-RE alloys. In this paper, in an effort to study the effect of RE additions on the role of $\{10\bar{1}2\}$ twinning in hardening, we designed experiments to favor the activity of this twinning mode. In this respect, we hampered recrystallization by exploiting process variables in order to produce samples of Mg-RE alloys with sharp $\langle 10\bar{1}0 \rangle$ fiber texture. Hence, $\{10\bar{1}2\}$ twinning was equally active during compression along extrusion direction in pure Mg and Mg-RE alloys. We monitored and investigated the effect of RE additions in high purity Mg on the $\{10\bar{1}2\}$ twinning behavior and its subsequent effects on strain hardening and plastic flow behavior.

160

5.2 Experimental procedure

To this end, Mg- 0.40 Ce and Mg-0.38 wt. % Gd binary alloys along with pure Mg were cast using 99.99999% pure magnesium and 99.999% pure rare earth elements in a vacuum induction melt furnace using a tantalum crucible at Ames Laboratory. The as-cast alloys were solution treated at 450 ºC for 10 h under flowing argon gas atmosphere followed by water quenching. The chemical compositions of annealed billets were analyzed using inductively coupled plasma atomic emission spectroscopy (ICP-AES) method. Solution treated alloys were machined to cylindrical specimens ~32 mm (1.25 in) in diameter and ~25 mm (1 in) long cylinders and were subject to indirect extrusion at ram speeds of 10 mm/min and 40 mm/min at 450 ºC with extrusion ratio of 1:6 followed by air cooling. Cylindrical compression samples with height to diameter ration of 1.5 were machined from extrudates. We conducted compression tests with constant strain rate of 0.001 s^{-1} at room temperature up to true strains of 0.04, 0.07, 0.11 and till failure. We conducted slow extrusions with small ratio in order to impose less strain energy, which is essential to drive dynamic recrystallization (DRX), and preserve the deformation texture (i.e $\langle 10\bar{1}0 \rangle$ fiber) in RE-containing alloys. Therefore, we were able to trigger the formation of $\{10\bar{1}2\}$ twinning profusely by compressing along extrusion direction (ED) (i.e. normal to $\langle c \rangle$ axis of $\langle 10\bar{1}0 \rangle || ED$ grains). This emboldened the effect of RE addition on $\{10\bar{1}2\}$ twinning induced hardening to an observable scale. Additionally, one fast extrusion was conducted to address the effect of DRX volume fraction on plastic flow behavior of the material.

Compressed samples were cut along compression axis and prepared by standard metallographic techniques and polished using 0.06 μm colloidal silica (Struers OPS) for

10 minutes. In preparation for electron back scattered diffraction (EBSD) analysis, electro-polishing was conducted using a Struers LectroPol-5 on polished samples in chilled Struers C1 electrolyte at 25 V for 120 s at -5 ℃. Samples were sonicated for 20 minutes afterwards in absolute ethanol to remove artifacts from the surface. Texture and microstructure analysis were conducted on transverse cross-sectional using EBSD. EBSD analyses were performed using a field emission scanning electron microscope (SEM) Zeiss Supra 40 at the operating voltage of 20 kV. Scanning step size was 1 µm for micro-texture measurements and 0.1 µm for ones used for intragranular misorientation axes (IGMA) analysis.

5.3   Results and discussion

Figure 5.1 shows the inverse pole figures (IPFs) of extruded materials along with their IPF maps. RE additions retard the rate of DRX in Mg-RE alloys [12], and hence, they retain their deformed microstructure after slow extrusions with a trivial volume fraction of DRX grains (Figure 5.1b and c). Therefore, we observed strong $\langle 10\bar{1}0 \rangle$ fiber texture as RE driven texture modification occurs during recrystallization [13, 14]. IPF map of Pure Mg in Figure 5.1a shows ~50 % DRX progress that spread $\langle 10\bar{1}0 \rangle$ fiber to $\langle 10\bar{1}0 \rangle - \langle 11\bar{2}0 \rangle$ fiber due to high mobility of $\{13\bar{4}0\}$ twin boundary upon recrystallization, which weakens the texture intensity [15]. However, all the grains within $\langle 10\bar{1}0 \rangle - \langle 11\bar{2}0 \rangle$ fiber are susceptible to $\{10\bar{1}2\}$ twinning during compression along ED, as they have their $\langle c \rangle$-axis perpendicular to ED and compression direction. Figure 5.1d indicates that higher ram speed (i.e. 40 mm/min) instigates DRX nucleation and growth, which consequently modifies the texture to lower intensities and reorients grains to orientations less susceptible to twinning.
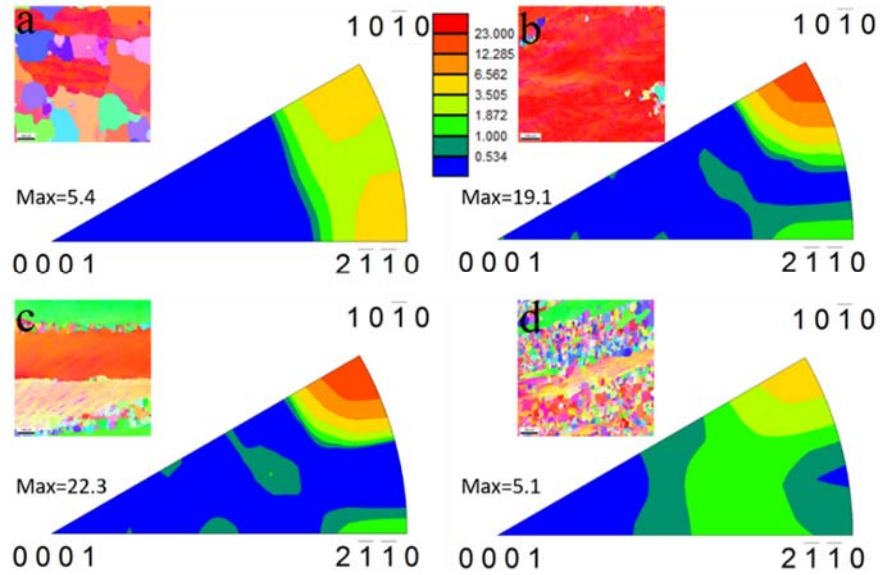
162

Figure 5.1   Inverse pole figures (IPFs) and IPF maps of extrude alloys.

a) pure Mg, **b)** Mg-0.38 Gd and **c, d)** Mg- 0.40 wt. %Ce. Extrusion was conducted at 450 ºC with 10 mm/min ram speed for **a-c** and 40 mm/min for **d** with 1:6 area reduction ratio.

Compression along ED direction, which triggered extensive formation of $\{10\bar{1}2\}$ twins in slowly extruded samples, illustrated a remarkable difference between pure Mg and binary Mg-RE alloys regarding their $\{10\bar{1}2\}$ twinning induced hardening in Region II in Figure 5.2b. Meanwhile, the fast extrusion sample expressed a higher compressive yield and a lower work hardening rate due to texture modification during DRX and less twin activation. The higher strain hardening rate for RE-containing alloys resulted in greater maximum flow stresses in Figure 5.2a. On the other hand, it reduced ductility. The IPF maps of interrupted pure Mg compression samples (inset micrographs in Figure 5.2a) explain the plastic flow behavior in regions I-III. Region I starts from $\varepsilon_t = 0.025$ associated with activation of $\{10\bar{1}2\}$ twinning that accommodates about 80% of the imposed deformation [4]. At $\varepsilon_t = 0.07$, relatively higher volume fraction of

163

{10$\bar{1}$2} twins (crystallographically harder orientations) and immense interaction of {10$\bar{1}$2} twin boundaries with basal and $\langle c + a \rangle$ dislocations increase the work hardening rate and starts Region II [4, 5]. It is worth noting that {10$\bar{1}$2} twinning reorients parent grains by ~86º around $\langle 11\bar{2}0 \rangle$ [16], and align their $\langle c \rangle$ axis nearly parallel to extrusion/compression direction. Hence, the imposed compressive strain in twinned grains (i.e. hard orientations) is mainly accommodated by $\langle c + a \rangle$ dislocations [4]. Variants of {10$\bar{1}$2} twins grow to saturation at $\varepsilon = 0.09$ [3, 4], at which the highest rate of change in work hardening curves was observed. At $\varepsilon = 0.11$, work hardening curves approach their peak values. Region III is associated with a sharp decrease in work hardening rate of Mg-RE alloys. On the other hand, pure Mg reaches its peak hardening rate at higher strains and expresses a smoother transition in hardening behavior (Figure 5.2b).

RE addition slightly increased the work hardening rate and flow stress in Region I (Figure 5.2). This trivial difference may be justified by RE solid solution strengthening and segregation of RE elements to grain boundaries, which suppresses dislocation motion [17].

However, the work hardening rate in region II is significantly higher for Mg-RE alloys. This remarkable difference may be associated with two microstructural observations: **1)** {10$\bar{1}$2} twins pass through the low angle grain boundaries (LAGBs) between the pancake shaped grains (Figure 5.3a and b), which resulted in the formation of large twins (Figure 5.3 and 5.4a). On the other hand, length of {10$\bar{1}$2} twins is pinned by grain boundaries in pure Mg, which limits their growth. Therefore, in Mg-RE alloys, there is a higher probability of interactions between grain boundary dislocations and twin

boundaries, which may lead to a higher dislocation forest hardening during early stages of plastic deformation Region II (i.e. $\varepsilon_t = 0.07 - 0.09$).

2) EBSD scans with 0.1 µm step size in Figure 5.3c revealed that the transmutation of basal dislocations take place during the growth of a $\{10\bar{1}2\}$ twin, which has crossed LAGBs $(< 5°)$ composed of geometrically necessary dislocations (GNDs). Figure 5.3c shows that arrays of basal dislocations (indicated by red arrows) transmute into prismatic dislocations (indicated by black arrows) as the $\{10\bar{1}2\}$ twin consumes the parent grain [18]. The observed dislocation transmutation enhances the forest hardening rate by producing prismatic dislocations, which have higher CRSS value compared to basal ones [2]. Transmuted prismatic dislocation could serve as hard obstacles for glide of $\langle c + a \rangle$ dislocations within hard orientations.

After $\{10\bar{1}2\}$ twin saturation at around $\varepsilon_t = 0.09$, plastic deformation continues by glide of $\langle c + a \rangle$ dislocations within hard orientations in Region II [4]. RE additions facilitates $\langle c + a \rangle$ slip by decreasing its CRSS value [19, 20], which results in easier dislocation glide and faster dislocation generation and multiplication [21, 22]. Nevertheless, Mg-RE alloys express higher flow stress compared to pure Mg, particularly after $\varepsilon = 0.09$ that commensurate with $\{10\bar{1}2\}$ twin saturation strain (Figure 5.2b) [3, 4]. The observed discrepancy could be rationalized by aforementioned higher work hardening rate in Mg-RE alloys, which compensates for the RE driven softened $\langle c + a \rangle$ slip. It is worth noting that the misorientation axis of LAGBs ranging $(5\text{-}10°)$ altered from $\langle 10\bar{1}0 \rangle$ to $[0001]$, which is associated with lattice rotations induced by a $\{10\bar{1}2\}$ twin crossing the LAGBs (Figure 5.3b).
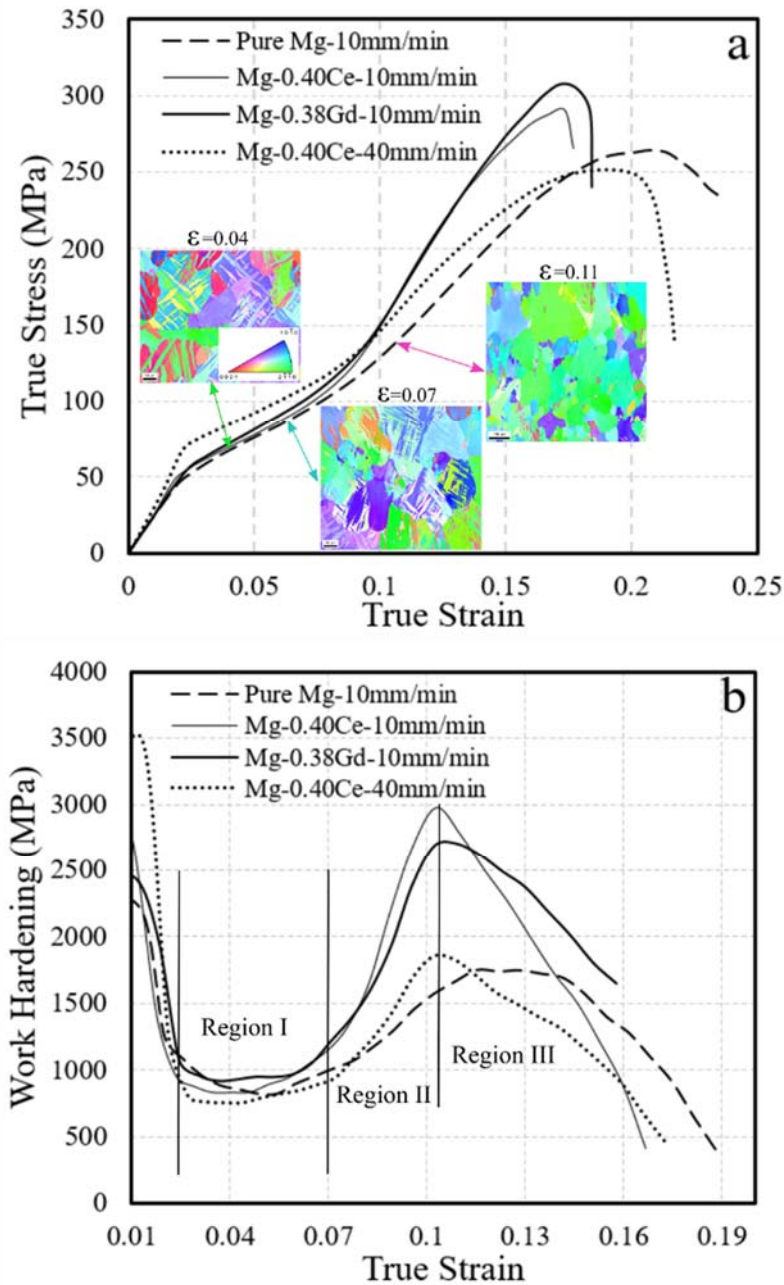
Figure 5.2   Compression testing results for extruded materials.

a) Typical true stress-true strain plot for compression tests along extrusion direction for extruded materials listed in Figure 1. The inset IPF maps correspond to pure magnesium strained to 0.04, 0.07 and 0.11 compressive true strain. **b)** The corresponding work hardening curves.
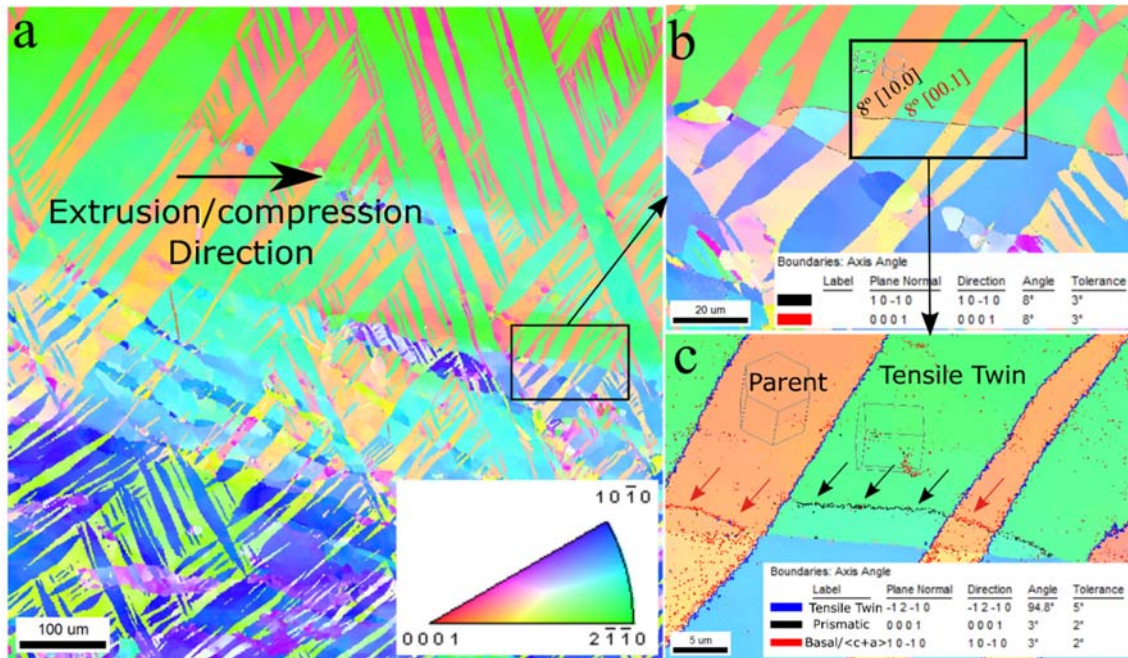
166

Figure 5.3　　EBSD analysis of Mg-0.38 wt. % Gd alloy after compression.

a) A typical EBSD scan of the extruded Mg-0.38 wt. % Gd alloy after compression to 0.04 true strain. **b)** An IPF map with scanning step size of 0.1 µm illustrating extension twins passing the grain boundaries. **c)** A higher magnification image from **b** highlighting extension twin boundaries along with basal/$\langle c + a \rangle$ and prismatic dislocations. Red and black arrows indicate the transmutation of basal/$\langle c + a \rangle$ to prismatic dislocations as the extension twins grow.

$\langle c + a \rangle$ dislocation glide rotates twinned lattice around its Taylor axis (i.e. $\langle \bar{1}100 \rangle$) [17], which deviates $\langle c \rangle$-axis of the crystals from compression direction. At $\varepsilon = 0.11$, 0.1 µm step size EBSD scan of Mg-0.40 Ce wt. % alloy indicated lattice rotations about 2-6º, which tallies a Schmid factor of 0.04-0.1 for basal slip. Hence, basal and prismatic modes activate and the work hardening rate starts to sharply decrease at the beginning of Region III, which is conceivably due to the gap between the critical resolved shear stress (CRSS) values of basal/prismatic and $\langle c + a \rangle$ modes.

On the other hand, the work hardening curve of pure Mg in Figure 5.2b shows a broad peak, which insinuates less $\langle c + a \rangle$ driven rotations. This leads to higher stored strain energy and deformation inhomogeneity at grain boundaries and triple junctions, which triggers low temperature dynamic recrystallization (LTDRX) at room temperature. Figure 5.4b is the image quality (IQ) map of a pure Mg sample compressed to $\varepsilon = 0.11$. As can be seen, dynamic recrystallization (DRX) nucleates extensively at triple junctions, which have the highest energy, to produce fresh DRX grains for continuation of plastic deformation. Occurrence of LTDRX can be rationalized by extensive activity of $\{10\bar{1}2\}$ twins prior to recrystallization and high purity of the experimental Mg billet, which weakens the barriers for bulk diffusion. However, small additions of RE halts recrystallization nucleation at room temperature due to recrystallization retardation and activation of non-basal slip modes [12, 19]. Therefore, Region III starts sharply for Mg-RE alloys, while pure Mg expresses a smooth transition of deformation mechanisms.

5.4   Summary and conclusions

In summary, we investigated the effect of rare earth element additions on hardening typically associated with $\{10\bar{1}2\}$ twinning. Our mechanical testing results indicated a remarkable increase in work hardening in rare earth element containing alloys, which boosted their plastic flow stress. Our micro-texture analyses clearly supported the test results. While in these alloys $\{10\bar{1}2\}$ twins nucleated shortly after the yield point and swiftly traversed low angle grain boundaries, in pure Mg, grain boundaries stopped twin propagation. This resulted in formation of large $\{10\bar{1}2\}$ twins in

Mg-RE alloys that enhanced the interaction of grain boundary dislocations and twin boundaries.
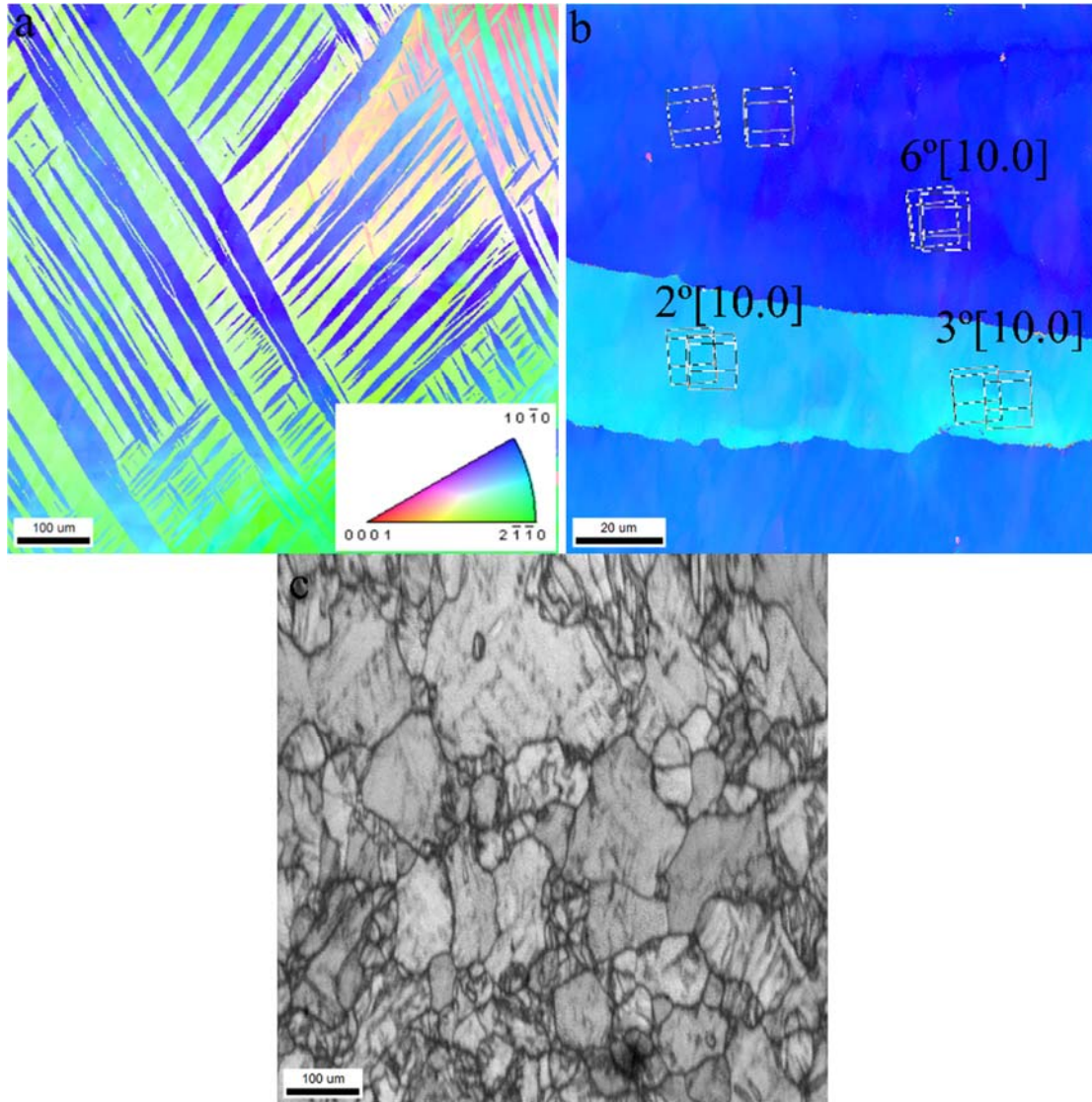

Figure 5.4   EBSD analysis of extruded Mg-0.40 wt. % Ce alloy and pure Mg after compression.

a) A typical EBSD scan of Mg-0.40 wt. % Ce alloy extruded with 10 mm/min ram speed, after compression to 0.04 true strain showing formation of large extension twins passing grain boundaries. b) 0.1 μm step size EBSD scan of Mg-0.40 wt. % Ce alloy at $\varepsilon = 0.11$ indicating rotations around $\langle 10\bar{1}0 \rangle$ axis within twinned grains. **c)** Image quality (IQ) map of extruded pure Mg strained to 0.11 true strain, reveling the occurrence of low temperature dynamic recrystallization upon twin saturation.

Moreover, transmutation of basal $\langle a \rangle$ to prismatic $\langle a \rangle$ dislocations occurred during growth of the twins that crossed several low angle grain boundaries. Upon twin saturation, rare earth element additions boosted $\langle c + a \rangle$ dislocations activity, which significantly escalated the work hardening rate due to their entanglement with transmuted prismatic dislocations. High work hardening rate more than compensated for the softer $\langle c + a \rangle$ slip in rare earth containing alloys and yielded higher flow stress. $\langle c + a \rangle$ activity within hard orientations induced rotations around the $\langle \bar{1}100 \rangle$ Taylor axis which triggered basal $\langle a \rangle$ slip. Activation of basal $\langle a \rangle$ slip resulted in a sharp drop in the work hardening rate of rare earth element containing alloys.

5.5   References

[1] S.R. Agnew, Ö. Duygulu, Plastic anisotropy and the role of non-basal slip in magnesium alloy AZ31B, Int. J. Plast. 21 (2005) 1161-1193.

[2] A. Imandoust, C. Barrett, T. Al-Samman, K. Inal, H. El Kadiri, A review on the effect of rare-earth elements on texture evolution during processing of magnesium alloys, J. Mater. Sci. 52 (2017) 1-29.

[3] H. El Kadiri, J. Kapil, A. Oppedal, L. Hector, S.R. Agnew, M. Cherkaoui, S. Vogel, The effect of twin–twin interactions on the nucleation and propagation of twinning in magnesium, Acta Mater. 61 (2013) 3549-3563.

[4] A. Jain, S. Agnew, Modeling the temperature dependent effect of twinning on the behavior of magnesium alloy AZ31B sheet, Mater. Sci. Eng. A 462 (2007) 29-36.

[5] H. El Kadiri, A. Oppedal, A crystal plasticity theory for latent hardening by glide twinning through dislocation transmutation and twin accommodation effects, J. Mech. Phys. Solids 58 (2010) 613-624.

[6] S.-G. Hong, S.H. Park, C.S. Lee, Role of {10–12} twinning characteristics in the deformation behavior of a polycrystalline magnesium alloy, Acta Mater. 58 (2010) 5873-5885.

[7] M. Barnett, Twinning and the ductility of magnesium alloys: Part II.“Contraction” twins, Mater. Sci. Eng. A 464 (2007) 8-16.

[8] I. Beyerlein, J. Wang, M. Barnett, C. Tomé. Double twinning mechanisms in magnesium alloys via dissociation of lattice dislocations. Proc. R. Soc. A, vol. 468: The Royal Society, 2012. p.1496-1520.

[9] J.P. Hadorn, K. Hantzsche, S. Yi, J. Bohlen, D. Letzig, S.R. Agnew, Effects of Solute and Second-Phase Particles on the Texture of Nd-Containing Mg Alloys, Metall. Mater. Trans. A 43 (2012) 1363-1375.

[10] K. Hantzsche, J. Bohlen, J. Wendt, K.U. Kainer, S.B. Yi, D. Letzig, Effect of rare earth additions on microstructure and texture development of magnesium alloy sheets, Scripta Mater. 63 (2010) 725-730.

[11] N. Stanford, M.R. Barnett, The origin of “rare earth” texture development in extruded Mg-based alloys and its effect on tensile ductility, Mater. Sci. Eng. A 496 (2008) 399-408.

[12] R. Cottam, J. Robson, G. Lorimer, B. Davis, Dynamic recrystallization of Mg and Mg–Y alloys: Crystallographic texture development, Mater. Sci. Eng. A 485 (2008) 375-382.

[13] J. Bohlen, S. Yi, D. Letzig, K.U. Kainer, Effect of rare earth elements on the microstructure and texture development in magnesium–manganese alloys during extrusion, Mater. Sci. Eng. A 527 (2010) 7092-7098.

[14] N. Stanford, Micro-alloying Mg with Y, Ce, Gd and La for texture modification—A comparative study, Mater. Sci. Eng. A 527 (2010) 2669-2677.

[15] C.D. Barrett, A. Imandoust, A.L. Oppedal, K. Inal, M.A. Tschopp, H. El Kadiri, Effect of grain boundaries on texture formation during dynamic recrystallization of magnesium alloys, Acta Mater. 128 (2017) 270-283.

[16] M.R. Barnett, Twinning and the ductility of magnesium alloys, Mater. Sci. Eng. A 464 (2007) 1-7.

[17] J.P. Hadorn, K. Hantzsche, S. Yi, J. Bohlen, D. Letzig, J.A. Wollmershauser, S.R. Agnew, Role of Solute in the Texture Modification During Hot Deformation of Mg-Rare Earth Alloys, Metall. Mater. Trans. A 43 (2011) 1347-1362.

[18] A. Serra, D. Bacon, Computer simulation of screw dislocation interactions with twin boundaries in HCP metals, Acta metallurgica et materialia 43 (1995) 4465-4481.

[19] J.P. Hadorn, R.P. Mulay, K. Hantzsche, S. Yi, J. Bohlen, D. Letzig, S.R. Agnew, Texture Weakening Effects in Ce-Containing Mg Alloys, Metall. Mater. Trans. A 44 (2012) 1566-1576.

[20] S. Sandlöbes, M. Friák, J. Neugebauer, D. Raabe, Basal and non-basal dislocation slip in Mg–Y, Mater. Sci. Eng. A 576 (2013) 61-68.

[21] S.R. Agnew, L. Capolungo, C.A. Calhoun, Connections between the basal I1 "growth" fault and ⟨c+a⟩ dislocations, Acta Mater. 82 (2015) 255-265.

[22] S. Sandlöbes, S. Zaefferer, I. Schestakow, S. Yi, R. Gonzalez-Martinez, On the role of non-basal deformation mechanisms for the ductility of Mg and Mg–Y alloys, Acta Mater. 59 (2011) 429-439.

CHAPTER VI

SUMMARY AND CONCLUSIONS

We investigated the contribution of dynamic recrystallization (DRX) mechanisms to texture development in rare earth (RE) containing magnesium (Mg) alloys. X-ray diffraction, electron back scattered diffraction (EBSD), and transmission electron microscopy (TEM) results explicated the correlation between microstructural evolution and the formation of new RE-driven texture components. Slow and fast ram speeds along with different extrusion ratios provided the experimental capability for tracking recrystallization steps from nucleation to growth. We categorized our chemical compositions into two families: 1) complex Mg-RE alloys, 2) binary Mg-RE alloys.

Nucleation of new orientations in all of the experimental alloys occurred on the boundaries between the bands of deformed grains. EBSD characterizations revealed that active nucleation sites are of tilt character, as they see their misorientation axis/angle laying close to that of $\langle 10\bar{1}0 \rangle$ symmetric tilt boundaries or near CSL boundaries. Upon nucleation, concomitant activity of $\langle 10\bar{1}0 \rangle$ and $[0001]$ Taylor axes resulted in rotation of DRX nuclei to random orientations. While the population of basal and non-basal dislocation at nuclei is stochastic, their arithmetic summation tallied the axis and degree of lattice rotation. Although all of the investigated alloys shared the same nucleation sites, nucleation and growth mechanisms were totally different for complex and binary Mg-RE alloys.

Discontinuous dynamic recrystallization (DDRX) was active at DRX nucleation sites of complex alloys, which lead to formation grains with new orientations. Whilst, in complex alloys, continuous dynamic recrystallization (CDRX) contributed to the rotation of cell structures within deformed grains only to cause texture sharpening. Co-segregation of zinc (Zn) and RE alloys into the grain boundaries lowered their energy, which rendered them energetically stable. Accumulation of varying dislocation density due to different Schmid factors at the two sides of boundaries triggered strain induced boundary migration (SIBM) mechanism. Additionally, presence of β and $Mg_{24}Y_5$ phases at grain boundaries corroborated the serration of grain boundaries. The ensuing grain growth and orientation selection appeared to be significantly affected by the combined concentration of Zn and RE elements. Alloys with lower Zn and moderate MM content expressed homogenous grain boundary mobility, which triggered homogenous growth of all the nucleated orientations.

Binary Mg-RE alloys expressed a different recrystallization behavior, where CDRX appeared to be accountable for nucleation of orientations. Necklace structures developed alongside the grain boundaries. EBSD characterizations showed that DRX nuclei continuously nucleated, and produced chains of randomly oriented grains. a textural transition as a function of grain growth was observed, where the inverse pole figure (IPF) maps expressed RE texture for larger grain sizes. On the other hand, samples with smaller grain size expressed an arc in the stereographic triangle, which resembled an immature textural transition. Schmid factor (SF) analysis unraveled that lower SF of RE-oriented grains granted their survival during grain growth. Due to lower SF of RE grains,

and hence lower dislocation activity, grain boundary migration direction was toward non-RE grains. Therefore, RE grains thrived at the expense of non-RE grains.

Effect of $\langle 10\bar{1}2 \rangle$ twinning induced hardening was explored so as to address this lack of information in the existing literature. RE additions appeared to have a significant influence on the plastic flow behavior of Mg alloys, where $\langle 10\bar{1}2 \rangle$ twinning was immense. Higher activation of $\langle c + a \rangle$ dislocations in twinned grains and extensive transmutation of basal/$\langle c + a \rangle$ dislocations to prismatic dislocations resulted in enhanced work hardening in Mg-RE alloys.

CHAPTER VII

FUTURE WORK

In order to reveal the minute detail behind the recrystallization events in Mg-RE

alloys, some further investigations are required.

1. High Resolution TEM studies should be carried out to pinpoint the co-segregation
   behavior of Zn and RE elements to grain boundaries. Moreover, molecular
   dynamics (MD) simulations will cast more light on the energy of grain boundaries
   in the presence of Zn and RE elements.

2. MD simulations are essential for the grain boundary energy homogenization of
   $\langle 10\bar{1}0 \rangle$ tilt boundaries in Mg-RE alloys, which are the nucleation sites for RE
   texture.9

3. High resolution TEM studies on the effect of RE elements on the interaction of
   $\langle c + a \rangle$ dislocations with twin boundaries would reveal the effect of RE elements
   on dislocation transmutations.

4. Electron channeling contrast imaging (ECCI) would cast light on the activity and
   population of basal and non-basal dislocations at the nucleation sites.